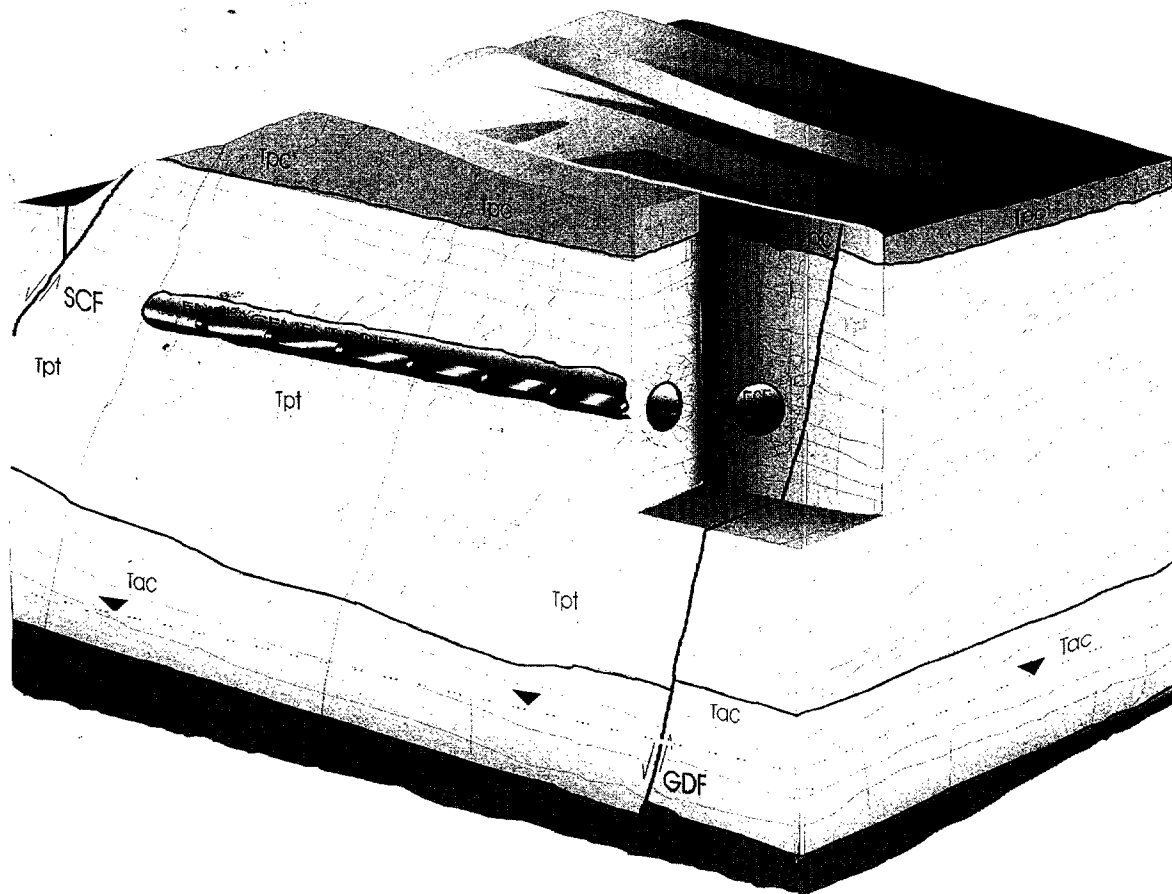


# Study of Unsaturated Zone Flow and Transport Models of Fractured Tuff





# Study of Unsaturated Zone Flow and Transport Models of Fractured Tuff

TR-108536

Final Report, October 1998

**WA**  
OPEN  
PACKAG  
YOUR ACCE  
LICENSE AG  
PRINT

EPRI Project Manager  
John H. Kessler

## **DISCLAIMER OF WARRANTIES AND LIMITATION OF LIABILITIES**

THIS REPORT WAS PREPARED BY THE ORGANIZATION(S) NAMED BELOW AS AN ACCOUNT OF WORK SPONSORED OR COSPONSORED BY THE ELECTRIC POWER RESEARCH INSTITUTE, INC. (EPRI). NEITHER EPRI, ANY MEMBER OF EPRI, ANY COSPONSOR, THE ORGANIZATION(S) BELOW, NOR ANY PERSON ACTING ON BEHALF OF ANY OF THEM:

(A) MAKES ANY WARRANTY OR REPRESENTATION WHATSOEVER, EXPRESS OR IMPLIED, (I) WITH RESPECT TO THE USE OF ANY INFORMATION, APPARATUS, METHOD, PROCESS, OR SIMILAR ITEM DISCLOSED IN THIS REPORT, INCLUDING MERCHANTABILITY AND FITNESS FOR A PARTICULAR PURPOSE, OR (II) THAT SUCH USE DOES NOT INFRINGE ON OR INTERFERE WITH PRIVATELY OWNED RIGHTS, INCLUDING ANY PARTY'S INTELLECTUAL PROPERTY, OR (III) THAT THIS REPORT IS SUITABLE TO ANY PARTICULAR USER'S CIRCUMSTANCE; OR

(B) ASSUMES RESPONSIBILITY FOR ANY DAMAGES OR OTHER LIABILITY WHATSOEVER (INCLUDING ANY CONSEQUENTIAL DAMAGES, EVEN IF EPRI OR ANY EPRI REPRESENTATIVE HAS BEEN ADVISED OF THE POSSIBILITY OF SUCH DAMAGES) RESULTING FROM YOUR SELECTION OR USE OF THIS REPORT OR ANY INFORMATION, APPARATUS, METHOD, PROCESS, OR SIMILAR ITEM DISCLOSED IN THIS REPORT.

ORGANIZATION(S) THAT PREPARED THIS REPORT

**Groundwater Simulations Group**

## **ORDERING INFORMATION**

Requests for copies of this report should be directed to the EPRI Distribution Center, 207 Coggins Drive, P.O. Box 23205, Pleasant Hill, CA 94523, (925) 934-4212.

Electric Power Research Institute and EPRI are registered service marks of the Electric Power Research Institute, Inc. EPRI. POWERING PROGRESS is a service mark of the Electric Power Research Institute, Inc.

Copyright © 1998 Electric Power Research Institute, Inc. All rights reserved.



# CITATIONS

---

This report was prepared by

Groundwater Simulations Group  
574 Sprucehill Ave.  
Waterloo Ontario N2L 4V9  
Canada

Principal Investigator  
P. Forsyth

This report describes research sponsored by EPRI.

The report is a corporate document that should be cited in the literature in the following manner:

*Study of Unsaturated Zone Flow and Transport Models of Fractured Tuff*; EPRI, Palo Alto, CA: 1998. Report TR-108536.

# REPORT SUMMARY

---

One of the most pressing challenges for the candidate Yucca Mountain high level waste (HLW) repository is to understand how groundwater flow is distributed beneath the mountain in order to minimize the amount of groundwater that can come into contact with the buried HLW containers. This report presents the findings of a study of flow and transport processes through fractured tuff at Yucca Mountain. The study compares alternative mathematical models based on dual-permeability / dual-porosity and equivalent porous medium concepts. It concludes that a dual-porosity, dual-permeability model must be used to simulate fast fracture flow.

## Background

Recent experimental and modeling studies have called into question the usual assumptions based on the equivalent continuum model (ECM) commonly used to simulate unsaturated flow at the Yucca Mountain site. The recent discovery of  $^{36}\text{Cl}$  at the depth of the proposed repository beneath Yucca Mountain would appear to indicate the presence of fast flow paths from the surface to the repository. In general, ECM models are not suited for modeling such fast flow path situations. A pseudo ECM, dual continuum model (DCM), or discrete fracture model (DFM) may be better able to simulate fast flow paths.

## Objective

To investigate models for simulating unsaturated zone flow and transport in fractured tuff.

## Approach

Investigators modeled representative cross sections of the Yucca Mountain site using both dual-permeability and ECM approaches. They focused their attention on models that were capable of qualitatively predicting fast fracture flow consistent with recent experimental observations. As part of this effort, they modified an existing variably saturated flow and tracer transport computer program called Hydrologic Transport Simulator to provide DCM capability. The simulator, which uses parameters characteristic of the Yucca Mountain site, can handle highly nonlinear unsaturated flow conditions.

## Results

While flow simulations at Yucca Mountain are extremely challenging, this study shows that a dual-porosity, dual-permeability model represents the most viable option for simulating fast fracture flow. Simulations showed that

- 
- The ECM model cannot be used to simulate fast fracture flow.
  - The capillary barrier (Paintbrush formation) diverts from 27-79% of the infiltrating water to the fault zone, depending on which recharge rates and material properties are used. This occurs so long as there are no discrete fractures or breaks in the barrier layer.
  - Fast fracture flow through the fault zone is highly dependent on the fault zone material properties and the nature and magnitude of episodic infiltration events.
  - In cases where fast fracture flow occurs, very little  $^{36}\text{Cl}$  penetrates laterally away from the fault zone unless the matrix-fracture coupling term is reduced dramatically.
  - Depending on properties in the fault zone, the matrix is near saturated even under low long-term infiltration.
  - It is necessary to obtain a true steady-state flow solution before attempting to determine a transport solution. While exceedingly difficult, the nonlinear equation must be solved to very small residuals.
  - Regions of the system that are not in close proximity to active fault zones may take an exceedingly long time to reach equilibrium with respect to changes in infiltration at the surface.

### **EPRI Perspective**

An extensive set of simulations of a typical Yucca Mountain cross section revealed that fast fracture flow can be induced by even moderately large episodic infiltration events. In addition, significant movement of the tracer through the Paintbrush fault zone only occurs with alternation of the fault formation properties, or reduction of the matrix-fracture coupling term by two orders of magnitude. While neither of these two effects alone results in movement of the tracer away from the fault zone, combining both effects causes significant movement of tracer away from the fault zone. It would therefore appear to be necessary to further delineate mechanisms by which large episodic infiltration events occur, perhaps due to complex surface water-groundwater interaction. It is also imperative to further characterize the properties of fault zones at Yucca Mountain and to obtain a more precise understanding of the mechanism of matrix-fracture coupling. Related EPRI work includes *Yucca Mountain Total System Performance Assessment, Phase 3* (TR-107191, December 1996).

### **TR-108536**

**Interest Categories:** Exploratory research and new science, Land and water quality, Soil and groundwater remediation, Environmental compliance planning, High level waste

**Keywords:** Yucca Mountain, High-level radioactive wastes, Radionuclide migration, Radioactive waste disposal, Groundwater flow, Computer codes

## ABSTRACT

---

This report summarizes an investigation of models for simulation of unsaturated zone flow and transport in fractured tuff. Representative cross-sections of the Yucca Mountain site were modeled using both dual permeability and Equivalent Continuum Model (ECM) approaches. Attention was focused on models which were capable of qualitatively predicting fast fracture flow consistent with recent experimental observations. It is concluded that a dual permeability model must be used to simulate fast fracture flow. As well, there is very little solute transport laterally away from the fault zone unless the matrix-fracture coupling term is reduced from the theoretical value.

# CONTENTS

---

<b>1 INTRODUCTION .....</b>	<b>1-1</b>
<b>2 PHYSICAL SYSTEM .....</b>	<b>2-1</b>
<b>3 GOVERNING EQUATIONS (DUAL CONTINUUM AND ECM MODELS) .....</b>	<b>3-1</b>
3.1 Unsaturated Flow .....	3-1
3.1.1 Discretized Flow Equations .....	3-2
3.2 Unsaturated Transport Equations .....	3-6
3.2.1 Discretized Transport Equations .....	3-6
3.3 Transient Flow and Transport .....	3-8
3.4 ECM model .....	3-8
<b>4 VALIDATION.....</b>	<b>4-1</b>
4.1 Multidimensional Unsaturated Flow .....	4-1
4.2 One-dimensional Dual-permeability Unsaturated Flow and Transport.....	4-1
<b>5 MODEL RESULTS USING AN AVERAGE RECHARGE RATE OF ONE MILLIMETER PER YEAR AS A BASE CASE.....</b>	<b>5-1</b>
5.1 Steady 1 mm/yr Recharge with Additional Recharge Pulses.....	5-6
5.1.1 Case 1: Uniform Recharge .....	5-6
5.1.2 Case 2: Variable Recharge: 10 mm/week Infiltration Pulses .....	5-8
5.1.3 Case 3: Variable Recharge: 10 cm/week Infiltration Pulses.....	5-8
5.1.4 Case 4: Variable Recharge: 10 cm/week Infiltration Pulses using Altered Paintbrush Formation Fault Zone Properties .....	5-13
5.2 Dual-permeability/ECM Comparison .....	5-16
5.2.1 Case 5: Uniform Recharge: DPM/ECM Comparison .....	5-16
5.2.2 Case 6: Variable Recharge: 10 mm/week Infiltration Pulses , DPM/ECM Comparison.....	5-16

---

5.2.3 Case 7: Variable Recharge: 10 cm/week Infiltration Pulses , DPM/ECM Comparison.....	5-20
5.3 Flux Diversion .....	5-22
5.4 Long-term Periodic Infiltration .....	5-24
5.5 Apparent Water Ages from <sup>36</sup> Cl Decay .....	5-30
5.6 Results for Altered Fault Zone Properties .....	5-33
5.6.1 Cases 8 & 9: Variable Recharge, 10 mm/week and 10 cm/week Infiltration Pulses with F2 Fault Zone Properties.....	5-38
5.7 Reduction of the Matrix/Fracture Coupling Term.....	5-40
<b>6 ADDITIONAL MODEL RESULTS USING AN AVERAGE RECHARGE RATE OF FIVE MILLIMETERS PER YEAR AS A BASE CASE .....</b>	<b>6-1</b>
6.1 Base Case .....	6-4
6.2 Altered Paintbrush Properties .....	6-4
6.3 Reduction of the Matrix/Fracture Coupling Term.....	6-7
6.4 Combined Case .....	6-10
6.5 Flux Diversion .....	6-10
<b>7 CONCLUSIONS .....</b>	<b>7-1</b>
<b>8 REFERENCES .....</b>	<b>8-1</b>
<b>A DERIVATION OF CONVERGENCE CONDITION FOR DISCRETE FLOW SOLUTION .....</b>	<b>A-1</b>

## LIST OF FIGURES

Figure 2-1 Physical system.....	2-1
Figure 5-1 Finite-element mesh .....	5-2
Figure 5-2 Hydraulic head at steady-state .....	5-3
Figure 5-3 Matrix/fracture head difference, $dH (H_m - H_f)$ .....	5-4
Figure 5-4 Saturation at steady-state.....	5-5
Figure 5-5 Concentration at 50 years, Case 1 .....	5-7
Figure 5-6 Concentration at 10 years, Case 2 .....	5-9
Figure 5-7 Concentration at 50 years, Case 2 .....	5-10
Figure 5-8 Concentration at 10 years, Case 3 .....	5-11
Figure 5-9 Saturation at 10 years, Case 3 .....	5-12
Figure 5-10 Darcy flux vectors in (a) matrix and (b) fractures .....	5-14
Figure 5-11 Concentration after first 10 cm/week pulse, Case 4.....	5-15
Figure 5-12 DPM/ECM hydraulic head at steady-state .....	5-17
Figure 5-13 DPM/ECM saturation at steady-state.....	5-18
Figure 5-14 Concentration at 50 years, Case 6 .....	5-19
Figure 5-15 Concentration at 50 years, Case 7 .....	5-21
Figure 5-16 Vertical component of Darcy flux near the base of the infiltration spreading layer.....	5-22
Figure 5-17 Vertical component of Darcy flux near the repository level .....	5-23
Figure 5-18 Location of points A,B,C and D.....	5-24
Figure 5-19 Saturation in fracture at point A .....	5-26
Figure 5-20 Detail of saturation in fracture at point A.....	5-26
Figure 5-21 Saturation in the matrix at point A.....	5-27
Figure 5-22 Saturation in fracture at points A, B and C.....	5-27
Figure 5-23 Concentration in matrix and fracture at point A.....	5-28
Figure 5-24 Saturation in fracture at point D .....	5-28
Figure 5-25 Saturation in matrix at point D.....	5-29
Figure 5-26 $^{36}\text{Cl}$ concentration at steady-state .....	5-31
Figure 5-27 Apparent age of groundwater based on $^{36}\text{Cl}$ concentration .....	5-32
Figure 5-28 Fault Zones (a) TC and (b) F2 capillary pressure curves.....	5-33

---

Figure 5-29 Heads at steady-state using F2 fault zone properties .....	5-35
Figure 5-30 Saturations at steady-state using F2 fault zone properties .....	5-36
Figure 5-31 Concentration in matrix at steady-state using F2 fault zone properties .....	5-37
Figure 5-32 Apparent age of matrix waters using F2 fault zone properties .....	5-37
Figure 5-33 Change in concentration after a 10 cm/week pulse, F2 Fault Zone Properties, Case 9. ....	5-39
Figure 5-34 Change in concentration after a 10 cm/week infiltration event, Case 10 .....	5-42
Figure 5-35 Change in concentration after 1 year, Case 10 .....	5-43
Figure 5-36 Change in concentration after 50 years, Case 10 .....	5-44
Figure 6-1 Steady State System .....	6-3
Figure 6-2 Base Case Concentration, t=50 years .....	6-5
Figure 6-3 Base Case Concentrations with 10 cm/week Pulse Events .....	6-6
Figure 6-4 Altered Paintbrush Properties Concentrations, t=50 years.....	6-8
Figure 6-5 Fracture/Matrix Reduction Concentrations, t=50 years .....	6-9
Figure 6-6 Fracture/Matrix Reduction Concentrations, t=50 years .....	6-11
Figure 6-7 Flux Diversion .....	6-12
Figure 6-8 Flux Diversion for a 10 cm/week Pulse Event .....	6-13



LIST OF TABLES

---

Table 2-1 Geometry of Layered System .....	2-2
Table 2-2 Summary of flow parameters assigned to various units .....	2-3
Table 5-1 Head and saturation changes in Unit TCw1 .....	5-30
Table 6-1 Summary of flux diversion calculation .....	6-14

## SUMMARY

---

This report presents the findings of a study of flow and transport processes through fractured tuff at Yucca Mountain, and compares alternative mathematical models based on dual-permeability/dual-porosity and equivalent porous medium concepts.

The complete discrete equations for multidimensional flow and transport for a dual continua (dual porosity and dual permeability) model are derived in a finite element framework. The detailed form of the matrix-fracture coupling terms are given. In addition, the precise form of the flow convergence criteria is given which ensures that the transport solution has no incorrect local maxima and minima. This very tight convergence criteria for the steady state flow is essential for subsequent transport simulations.

A conceptual model of a cross-section typical of the Yucca mountain site is described. This model has 15 stratigraphic units, and abuts a fault zone which is divided into three units. A recharge spreading layer is used to allocate infiltration into matrix or fracture nodes.

An extensive series of flow and transport simulations (using a conservative contaminant,  $^{36}\text{Cl}$ ) were carried out using a dual permeability formulation. Simulations were run using uniform recharge and variable recharge, with different pulse recharge rates. Fast fracture flow was observed only with a high pulse recharge and altered Paintbrush fault zone (F1 PT) properties. Comparisons with the ECM formulation indicated that the ECM method could not simulate fast fracture flow due to episodic events.

Detailed analysis of uniform recharge simulations showed that the Paintbrush formation (PTn), sometimes referred to as a 'capillary barrier' layer, caused from 27 to 79% diversion of incoming infiltration at the repository depth.

A series of simulations with long term periodic recharge were also carried out, and detailed analysis of saturation histories at various depths was described. As expected, due to the matrix buffering effect, deep zones remote from active fault zones are very slow to respond to changes in surface infiltration.

---

A simulation was carried out in order to determine the effect of advective-dispersive transport and radioactive decay on the steady-state distribution of  $^{36}\text{Cl}$ . A plot of apparent age shows, as expected, that the more active fault zone waters are much younger than those in the non-fault zones. Predicted ages are in good agreement with previously reported values.

A series of simulations which used the F2 fault zone properties was carried out and showed that fast fracture flow was not achieved in that case, even during high pulse recharge events. Matrix saturations in the fault zone were much lower than in previous runs, and it is concluded that this inhibited fast fracture flow.

Although the simulations with the altered Paintbrush (fault zone) properties exhibited fast fracture flow, the contaminant plume was rapidly attenuated due to flow from the fractures into the matrix. Little movement of contaminant away from the fault zone was observed. Additional simulations were carried with a reduction of 1/100 of the theoretical value of the matrix-fracture coupling term. In this case, significant movement of the contaminant away from the fault zone was observed.

# 1

## INTRODUCTION

---

EPRI is engaged in research related to innovative ideas to resolve high level radioactive waste (HLW) repository issues. Current R&D that EPRI is pursuing in this area includes development of a repository performance assessment (PA) code and the development of regulatory performance standards for the HLW repository. The PA code has been successfully used to identify the most important mechanisms governing radionuclide release, which has served as guidance to DOE in their site characterization and repository design efforts. The repository performance standards work has yielded specific recommendations that EPRI is making to the regulatory authorities on the character of performance regulations and the technical bases for them.

One of the most pressing challenges for the Yucca Mountain HLW repository design is to understand how groundwater flow is distributed beneath Yucca Mountain so that it is possible to minimize the amount of groundwater that can come into contact with the buried HLW containers. In addition, the current high level of uncertainty in knowing how much water can contact the HLW containers makes it difficult to be able to predict potential movement of HLW contaminants. This makes demonstration of adequate repository performance difficult as well.

Recent experimental and modeling studies (e.g. Bodvarsson and Banduragga, 1996) have called into question the usual assumptions based on the Equivalent Continuum Model (ECM) which is commonly used to simulate unsaturated flow at the Yucca Mountain site. In particular, the recent discovery of  $^{36}\text{Cl}$ , originating from the era of atmospheric nuclear bomb detonation testing, at the depth of the proposed repository beneath Yucca Mountain would appear to indicate the presence of fast flow paths from the surface to the repository, which is a cause for concern. In general, ECM models are not suited for modeling such fast flow path situations. Other models, such as Pseudo ECM, Dual Continuum (DCM) or Discrete Fracture (DFM) models may be better able to deal with fast flow paths.

The objective of the work reported here is to determine which of the above models can be used to simulate flow and transport in heterogeneous fractured tuff (the type of rock found at the proposed repository horizon beneath Yucca Mountain) consistent with the recent experimental observations at Yucca Mountain (i.e., apparent fast fracture flow). Because of the paucity of data on the characteristics of individual fractures at Yucca Mountain, the work will focus on comparing the performance and suitability of

ECM and DCM formulations to represent flow and transport through a representative multi-layer vertical cross section at Yucca Mountain.

To achieve the objective, an existing variably-saturated three-dimensional flow and tracer transport computer program called Hydrologic Transport Simulator (HTS) (Sudicky and VanDerKwaak, 1996) was modified to provide Dual Continuum (DCM) capability. The simulator is capable of using parameters characteristic of the Yucca Mountain site, and has been designed to reliably handle the highly nonlinear unsaturated flow conditions that are characteristic of the site. As well, the basic data structure allows generalization to handle discrete fractures, and flow and transport in 1 or 2 as well as 3 dimensions. Because of the paucity of data on the characteristics of individual fractures at Yucca Mountain, this study focuses on flow and transport through a representative multi-layer vertical cross section.

In light of the results from the simulations conducted earlier in this project, and after consultation with various researchers involved in the Yucca Mountain project, it was determined that a final set of simulations should be carried out to reinforce those conclusions for higher average infiltration rate. This work is presented in Section 6.

The objectives of the additional work are threefold; 1) to present the mathematical formulation of the DCM model, 2) to show what processes are important for triggering the rapid movement of water (and tracer) along fast flow paths and 3) to investigate the fate of recharge water with respect to the proposed location of a HLW repository.

# 2

## PHYSICAL SYSTEM

Modeling flow and transport requires a simulation domain, a set of flow and transport parameters, and boundary conditions on the domain. The design of the two-dimensional domain (Figure 2-1) was based on work at Los Alamos by Robinson et al. (1995). Our simulation domain is a portion of a large cross-section (A-A', Robinson et al., 1995) oriented East-West across Antler Ridge. The section is 350 m long and extends downward from the ground surface approximately 625 m to the water table. The region is assumed to include a 50 m-wide fault zone along the right side. The vertical side boundaries provide a no-flow boundary for water and zero-dispersive flux for mass transport. The ground surface is represented as a fixed or time-varying flux boundary for flow and as a Cauchy flux boundary to accommodate solute inputs. The bottom boundary is a specified pressure boundary for flow which represents the water table and is a boundary for advective loss of solute mass to the saturated zone.

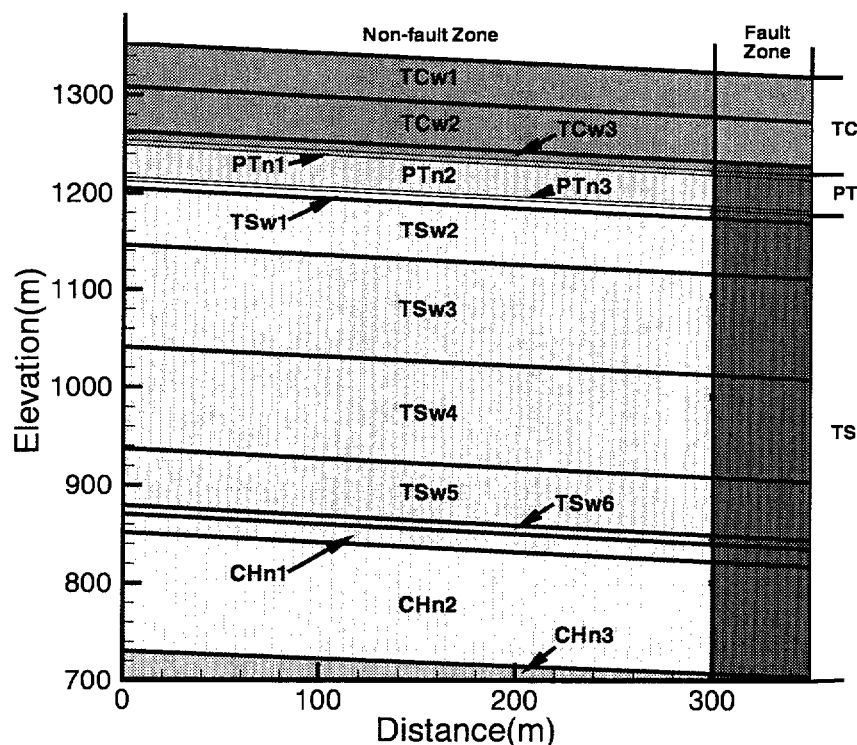


**Figure 2-1**  
**Physical system**

Selecting the length for the section is important given the tendency for lateral diversion of flow within the Paintbrush Tuff. In effect, the length of the section controls the volume of water ultimately diverted to the fault zone. Our conceptualization provides modest opportunities for lateral diversion and opportunities for downward flow across the Paintbrush Tuff. This conceptualization is in keeping with observations of Fabryka-Martin et al. (1996) of  $^{36}\text{Cl}$  detections along the ESF rather than only at major fault zones. Consequently, lateral diversion at the capillary barrier may be an imperfect process.

The simulation domain is subdivided into a number of zones having different hydrologic properties. Overall, 15 dipping stratigraphic layers are included, as described in Table 2-1. Our list of stratigraphic units to be included is the same as Robinson et al. (1995) and Wittwer et al. (1995). The fault zone is conceptualized in two ways and represented by either three zones (Fault 1) or one zone (Fault 2). A thin layer is included across the top to spread the recharge.

**Table 2-1**  
**Geometry of Layered System**

Unit	Thickness (m)	Elevation	
		Left Side (masl)	Right Side (masl)
TCw1	45	1353	1318
TCw2	45	1308	1273
TCw3	9	1263	1228
PTn1	5	1254	1219
PTn2	32	1249	1214
PTn3	3	1217	1182
TSw1	9	1214	1179
TSw2	59	1205	1170
TSw3	104	1146	1111
TSw4	104	1042	1007
TSw5	59	938	903
TSw6	9	879	844
CHn1	18	870	835
CHn2	113	852	817
CHn3	39	739	704
Bottom		700	700

Since the focus of this work is to develop an understanding of the mechanisms by which fast fracture flow may occur, we consider the simulated cross-section at described in Table 2-1 to be representative of a typical cross-section at Yucca Mountain. We do not claim that the data in Table 2-1 is an exact reproduction of any particular

cross-section. Ongoing work on the Yucca Mountain Project continues to develop a more detailed and refined stratigraphy. Our work here used the most recently available stratigraphic information at the time our study began. The 1996 study report from Lawrence Berkeley National Laboratory (Bodvarsson and Bandurraga, 1996) was not available until our work was well underway.

Flow and mass transport parameters need to be assigned to the fracture network and matrix in each zone. In general, these parameters are the same as those presented by Robinson et al. (1995). They are summarized in Table 2-2, along with information for the fault zones. As was the case with stratigraphic data, our work was based on the data available when the study began. Recent work has again led to changes in the basic system parameters. However, the system parameters are still highly uncertain. Consequently, our simulations should be viewed as providing a qualitative understanding of the general flow processes at Yucca Mountain.

**Table 2-2**  
**Summary of flow parameters assigned to various units**

Unit	Matrix Properties					Fracture properties				
	q %	Sr	k m <sup>2</sup>	a m <sup>-1</sup>	n	Sr	k m <sup>2</sup>	Spacing (m)	a m <sup>-1</sup>	n
TCw1	17	0.02	1E-18	0.0066	1.33	0.005	4E-12	0.618	0.8	3.0
TCw2	17	0.02	2E-18	0.0066	1.33	0.005	4E-12	0.618	0.8	3.0
TCw3	6	0.12	1E-18	0.0066	1.33	0.005	4E-12	0.618	0.8	3.0
PTn1	33	0.154	1E-13	0.16	1.2	0.005	2E-13	2.22	10.0	3.0
PTn2	37	0.154	5E-14	0.587	1.19	0.005	2E-13	2.22	10.0	3.0
PTn3	32	0.154	1E-13	0.424	1.17	0.005	2E-13	2.22	10.0	3.0
TSw1	6	0.12	1E-18	0.0066	1.41	0.005	4E-12	0.74	1.0	3.0
TSw2	15	0.045	4E-16	0.012	1.22	0.005	4E-12	0.74	1.0	3.0
TSw3	13	0.045	4E-18	0.02	1.28	0.005	4E-12	0.74	1.0	3.0
TSw4	14	0.045	5E-18	0.013	1.33	0.005	4E-12	0.74	1.0	3.0
TSw5	12	0.045	5E-18	0.0066	1.33	0.005	4E-12	0.74	1.0	3.0
TSw6	5	0.12	1E-18	0.0066	1.41	0.005	4E-12	0.74	1.0	3.0
CHn1	35	0.097	2E-13	0.2	1.15	0.005	1E-12	1.62	0.5	3.0
CHn2	28	0.097	3E-13	0.2	1.14	0.005	1E-12	1.62	0.5	3.0
CHn3	39	0.097	3E-13	0.2	1.14	0.005	1E-12	1.62	0.5	3.0
F1-TC	15	0.005	2E-18	0.0066	1.33	0.005	1.5E-11	0.5	1.0	3.0
F1-P	15	0.005	1E-13	0.0066	1.33	0.005	4E-13	0.5	1.0	3.0
F1-TS	15	0.005	5E-18	0.0066	1.33	0.005	1.5E-11	0.5	1.0	3.0
F2-all	30	0.1	1E-13	0.61	2.0	0.005	1E-11* 1E-10**	0.5	0.6	2.0

For Fractures, all permeabilities are bulk values.

F1 refers to fault zone.

For alternative fault zone F2 - \* designates horizontal permeability; \*\* designates vertical permeability



# 3

## GOVERNING EQUATIONS (DUAL CONTINUUM AND ECM MODELS)

---

### 3.1 Unsaturated Flow

The flow in the unsaturated zone is modeled using the usual assumption in which the water is mobile, but the air pressure is assumed to be constant. Fully saturated conditions can also be simulated. The following formulation is valid for both single permeability and dual permeability (rock matrix and fractures) simulations.

The usual form for the unsaturated-saturated flow equation is:

$$\frac{\partial}{\partial t}(\theta S_w) = -\nabla \cdot (\mathbf{V}_w) + q_w \quad (3-1)$$

where the Darcy flux of water is given by:

$$\mathbf{V}_w = -\mathbf{K} \cdot \lambda_w (\nabla P_w - \rho_w g \nabla D) \quad (3-2)$$

and where

- $S_w$  = saturation of water
- $P_w$  = pressure of water
- $\theta$  = volume averaged porosity
- $\rho_w$  = density of water
- $\mathbf{K}$  = absolute permeability tensor
- $\lambda_w = k_{rw} / \mu_w$
- $\mu_w$  = viscosity of water  $w$
- $k_{rw}$  = relative permeability of water
- $D$  = depth
- $g$  = gravitational acceleration

$$q_w = \text{source/sink term representing fluid exchange} \quad (3-3)$$

between rock matrix and fractures

The water pressure is related to the (constant) air pressure by the capillary pressure  $P_{caw}$  according to:

$$P_a = P_w + P_{caw}(S_w) \quad (3-4)$$

The basic form of equation (3-2) holds for both fractures and rock matrix. The various properties (i.e. porosity, permeability) and constitutive relations (i.e. relative permeability, capillary pressure) are different in fractures and matrix.

### 3.1.1 Discretized Flow Equations

Equation (3-2) is discretized using a control volume-finite element method (see Forsyth, 1991; Letniowski, 1991). This approach allows for the use of unstructured meshes, which are convenient for modelling complex geological structures.

Let  $N_i$  be the usual finite element basis functions such that

$$\begin{aligned} N_i &= 1 \text{ at node } i \\ &= 0 \text{ at all other nodes} \\ \sum_j N_j &= 1 \text{ everywhere in the solution domain} \end{aligned} \quad (3-5)$$

In the following we will restrict attention to linear basis functions defined on triangles in two dimensions and tetrahedra in three dimensions.

Defining  $\psi = P_w - \rho_{wj}gD$ , then  $P_w$ ,  $\psi$ , and  $S_w$  are approximated by

$$\begin{aligned} P_w &= \sum_j P_{wj} N_j \\ \psi &= \sum_j \psi_j N_j \\ &= \sum_j (P_{wj} - \rho_{wj}gD_j) N_j \\ S_w &= \sum_j S_{wj} N_j \end{aligned} \quad (3-6)$$

If superscript  $N$  denotes the time level, then the discrete form of equation (3-2) is:

$$\left\{ [\theta S_w]_i^{N+1} - [\theta S_w]_i^N \right\} \frac{V_i}{\Delta t} = \sum_{j \in \eta_i} (\lambda_w)_{(ij+1/2)}^{N+1} \gamma_{ij} (\psi_j^{N+1} - \psi_i^{N+1}) + (q_w)_i^{N+1} \quad (3-7)$$

where:

$$\begin{aligned} V_i &= \int_v N_i dv \\ \psi_i^{N+1} &= P_i^{N+1} - \rho_{w,ij+1/2}^{N+1} g D_i \\ \rho_{w,ij+1/2} &= (\rho_{w,j}) / 2 \end{aligned} \quad (3-8)$$

Here  $\eta_i$  is the set of neighbor nodes of node  $i$  such that  $\gamma_{ij}$  are non-zero. Discrete equations (3-7) are valid for both matrix and fracture nodes. Generally, a matrix or fracture node  $i$  will be coupled to both fracture and matrix nodes  $j$ . Note that the volume  $V_i$  is the same for both matrix and fracture nodes located at the same physical point. Porosities are defined as volume averaged, so that the porosity of a fracture node will generally be very small.

If nodes  $i, j$  in equation (3-7) are both matrix nodes or both fracture nodes, then

$$\gamma_{ij} = - \int_v \nabla N_i \cdot \mathbf{K} \cdot \nabla N_j dv \quad (3-9)$$

For matrix nodes, the  $\mathbf{K}$  appearing in equation (3-9) is the actual matrix absolute permeability. For fracture nodes, the permeability is the effective permeability, i.e.

$$\begin{aligned} K_x &= K_{frac} w_f (1/L_z + 1/L_y) \\ K_y &= K_{frac} w_f (1/L_z + 1/L_x) \\ K_z &= K_{frac} w_f (1/L_y + 1/L_x) \end{aligned} \quad (3-10)$$

where  $K_x$ ,  $K_y$  and  $K_z$  are the fracture permeabilities in the  $x, y, z$  directions,  $w_f$  is the fracture width, and  $L_x$ ,  $L_y$  and  $L_z$  are the fracture spacing in the  $x, y, z$  directions. The fracture absolute permeabilities are given by

$$K_{frac} = \frac{w_f^2}{12} \quad (3-11)$$

If nodes  $i, j$  are such that node  $i$  is a matrix node, and node  $j$  is a fracture node, or *viceversa* then

$$\gamma_{ij} = 4V_i \left( \frac{K_x^{matrix}}{L_x^2} + \frac{K_y^{matrix}}{L_y^2} + \frac{K_z^{matrix}}{L_z^2} \right) \quad (3-12)$$

where  $K^{matrix}$  are the matrix permeabilities (i.e. either at node  $i$  or node  $j$  depending on which of  $i$  or  $j$  is the matrix node). Equation (3-12) is based on a geometric argument (Dean and Lo, 1983) which assumes a harmonic average for the permeabilities, and that the fracture width  $w_f$  is infinitesimal compared to the fracture spacing.

Upstream weighting is used for the term  $(\lambda_w)_{(ij+1/2)}$  in equation (3-7)

$$\begin{aligned} (\lambda_w)_{(ij+1/2)} &= (\lambda_w)_i \text{ if } \gamma_{ij}(\psi_j^{N+1} - \psi_i^{N+1}) < 0 \\ &= (\lambda_w)_j \text{ if } \gamma_{ij}(\psi_j^{N+1} - \psi_i^{N+1}) > 0 \end{aligned}$$

Boundary conditions are simulated by using the source/sink term  $(q_w)_i$  in equation (3-7) to inject or remove the appropriate amount of water (Forsyth et al, 1995).

The discrete equations are solved using full Newton iteration with variable substitution (Forsyth et al, 1995). Steady state flow was determined by initializing the system in gravity equilibrium, and then running the model to a large time. The steady state was deemed to have been reached when changes for the saturations at each node were  $<10^{-6}$  over a large timestep (i.e.  $10^5$  years).

However, problems were observed during preliminary tests on two dimensional simulations using matrix and fracture properties similar to those thought to be representative of Yucca Mountain. For example, if the steady state flow was used as the initial state for the transport simulations, even if small (i.e.  $< 1$  year) timesteps were used for the transport simulations, we observed local maxima and minima in the transport simulation which were physically incorrect.

The problem was traced to the fact that, even though the saturation changes were very small (for the flow solution), the effective residual for a fracture node might be large.

If we define the residual at a node  $r_i$  to be

$$r_i = \left\{ [\theta S_w]_i^{N+1} - [\theta S_w]_i^N \right\} \frac{V_i}{\Delta t} - \sum_{j \in \Gamma_i} (\lambda_w)_{(ij+1/2)}^{N+1} \gamma_{ij} (\psi_j^{N+1} - \psi_i^{N+1}) - (q_w)_i^{N+1} \quad (3-13)$$

and then let

$$flow_i^{pos} = \max\left((q_w)_i^{n+1}, 0\right) + \sum_{j \in \eta_i} \max\left((\lambda_w)_{(ij+1/2)}^{N+1} \gamma_{ij} (\psi_j^{N+1} - \psi_i^{N+1}), 0\right) \quad (3-14)$$

we can define an appropriate error measure based on requiring that the transport solution be monotone. If

$$\alpha_i = \frac{\theta V_i S_{wi}^N / (\Delta t) + flow_i^{pos}}{\theta V_i S_{wi}^N / (\Delta t) + flow_i^{pos} + r_i} \quad (3-15)$$

then it can be shown that the correct measure of error which is required to ensure that the transport simulation (which uses the flow solution for convective transport) will not result in solutions which cause incorrect local maxima and minima is:

$$flow_i^{error} = \left| (1 - |\alpha_i|) \right| \quad (3-16)$$

Steady state flow solutions were then obtained using the following strategy:

- The system was initialized in gravity equilibrium.
- Beginning with small timesteps, the system was simulated to a large time, using the usual convergence criteria based on saturation updates (i.e. convergence was deemed to have occurred when changes in the saturations were  $< 10^{-6}$ ). If necessary, this solution was obtained in two steps:
  1. Use pseudo fracture porosities of  $10^3$  times actual fracture porosities.
  2. Use the solution in step [1] above as the starting guess for a simulation with the actual fracture porosities.
- Further large timesteps were then taken using the additional convergence criteria (3-16)

$$\max_i(flow_i^{error}) < 10^{-3} \quad (3-17)$$

We note that it is quite difficult to obtain a steady state flow solution which is sufficiently accurate to use as the initial state for the transport solution. This problem has also been observed previously (Wu, private communication). This difficulty is due to the very nonlinear nature of the fracture and matrix capillary pressure relations, the very small porosity of the fracture nodes, and the large flow which occurs in the fractures at very small fracture saturations. We anticipate that sufficiently accurate

three dimensional dual permeability flow solutions will also be difficult to obtain (Y.W. Wu, private communication).

### 3.2 Unsaturated Transport Equations

The transient unsaturated advective dispersive transport equations are solved using the same control volume-finite element method which is used to solve the unsaturated zone flow equations. It is important to use a consistent approach for both flow and transport, so that any material balance errors in the flow solution do not become magnified in the transport solution.

The mass transport of a contaminant is given by

$$\frac{\partial}{\partial t}[(\theta S_w + \rho_b K_d)C] = -\nabla \cdot (C \mathbf{V}_w - \theta S_w \mathbf{D} \nabla C) + q'_w C - \lambda_d C [\theta S_w + \rho_b K_d] \quad (3-18)$$

Where

$$\begin{aligned} C &= \text{concentration} \\ \mathbf{D} &= \text{dispersion/diffusion tensor} \\ \rho_b &= \text{bulk density of matrix or surface density of fractures} \\ K_d &= \text{linear sorption coefficient} \\ \lambda_d &= \text{decay constant} \end{aligned} \quad (3-19)$$

The dispersion/diffusion tensor is given by

$$\phi S_w \mathbf{D} = \alpha_T |\mathbf{V}_w| \mathbf{I} + (\alpha_L - \alpha_T) \frac{\mathbf{V}_w \mathbf{V}_w}{|\mathbf{V}_w|} + \phi S_i D_m \mathbf{I} \quad (3-20)$$

where  $\alpha_T$  is the transverse dispersivity,  $\alpha_L$  is the longitudinal dispersivity and  $D_m$  is the effective molecular diffusion coefficient.

#### 3.2.1 Discretized Transport Equations

The discretized transport equations (for either matrix or fracture nodes) are then (using the same control volume finite element method used for the flow equations):

$$\begin{aligned}
 & \left\{ [\theta S_w CR]_i^{N+1} - [\theta S_w CR]_i^N \right\} \frac{V_i}{\Delta t} \\
 &= \sum_{j \in \eta_i} C_{(ij+1/2)}^{N+1} (\lambda_w)_{(ij+1/2)}^{N+1} \gamma_{ij} (\psi_j^{N+1} - \psi_i^{N+1}) \\
 &+ \sum_{j \in \eta_i} \gamma'_{ij} (C_j^{N+1} - C_i^{N+1}) + (q_w C_{ups})_i^{N+1} \\
 &- \lambda_d C_i^{N+1} [\theta S_i^{N+1} + \rho_b K_d]
 \end{aligned} \tag{3-21}$$

Where

$$\begin{aligned}
 R &= 1 + \frac{\rho_b K_d}{\theta S_w} \\
 C_{ups} &= C_i \text{ if } q_w < 0 \\
 &= C_{inflow} \text{ if } q_w > 0
 \end{aligned} \tag{3-22}$$

where  $C_{inflow}$  is the specified source inflow concentration (recall that  $q_w$  is the source/sink term used to represent boundary conditions). In order to preserve monotone solutions for the transport, and yet avoid the excessive numerical dispersion generated by upstream weighting, a nonlinear flux limiter (Unger et al, 1996) is used for the term  $C_{(ij+1/2)}$  in equation (3-21). Other terms in equation (3-21) are defined as for the discrete flow equation (3-7).

If nodes  $i, j$  are both matrix nodes, or both fracture nodes, then

$$\gamma'_{ij} = - \int_v \nabla N_i \cdot \phi S_w^{N+1} \mathbf{D} \cdot \nabla N_j dv \tag{3-23}$$

where the velocity is computed in the usual finite element manner.

If node  $i$  is a fracture node and node  $j$  is a matrix node, or vice versa, then

$$\gamma'_{ij} = \left( \alpha_L |(V_w)_{(ij+1/2)}| + D_m (S_w)_{(ij+1/2)}^{N+1} \theta_{(ij+1/2)} \right) 4V_i (1/L_x^2 + 1/L_y^2 + 1/L_z^2) \tag{3-24}$$

The velocity used in the matrix-fracture dispersion term (3-24) is given by

$$|(V_w)_{(ij+1/2)}| = \gamma_{ij} (\lambda_w)_{(ij+1/2)}^{N+1} |\psi_j - \psi_i| / A_{ij} \tag{3-25}$$

with the matrix-fracture interfacial area  $A_{ij}$  given by

$$A_{ij} = 2V_i (1/L_x + 1/L_y + 1/L_z) \quad (3-26)$$

Using a harmonic type weighting, and assuming that the fracture width is small compared to the fracture spacing, then we obtain the following for the interfacial saturations and porosities in equation (3-24)

$$\begin{aligned} (S_w)_{(ij+1/2)} &= (S_w)_{mat(i,j)} \\ \theta_{(ij+1/2)} &= \theta_{mat(i,j)} \end{aligned} \quad (3-27)$$

where

$$\begin{aligned} mat(i, j) &= i \text{ if } i \text{ is the matrix node} \\ &= j \text{ otherwise} \end{aligned} \quad (3-28)$$

This usually results in a large dispersion/diffusion coupling, since the matrix saturations and porosities are large. Alternative models of matrix-fracture dispersion/diffusion transport may give smaller coupling.

### 3.3 Transient Flow and Transport

The simulation of transient flow and transport is carried out in the following manner:

- An initial steady state flow solution is obtained as described in Section 3.1.1.
- The transient flow and transport is simulated by stepping through time, using the steady state flow as an initial state. Transient flow is generated by time dependent boundary conditions. Each timestep of the transient flow and transport is carried out in two steps:
  1. The flow solution is obtained for the values of saturations and pressures at the end of the timestep.
  2. Since the flow timestep can become very large, a flow timestep is broken into smaller transport sub-timesteps. Each transport sub-timestep solves the discrete equations (3-21). In each transport sub-timestep, the fluid saturations in the storage terms are linearly interpolated based on the values at the beginning and end of the large flow timestep (this ensures correct material balance).

### 3.4 ECM model

The Equivalent Continuum Model (ECM) uses only a single discrete node at each physical location. Effective relative permeability and capillary pressure curves are



determined by assuming that instantaneous thermodynamic equilibrium exists between matrix and fractures. A detailed description of the method used to compute these effective curves is described in Wu, Finsterle and Pruess (1996).

# 4

## VALIDATION

---

### 4.1 Multidimensional Unsaturated Flow

The multidimensional unsaturated flow module was validated by simulating the problems described in Forsyth et. al., 1995. Results for these problems have been previously reported in the literature. Good agreement was obtained between the current model and previous simulations.

### 4.2 One-dimensional Dual-permeability Unsaturated Flow and Transport

The current model was validated by simulating a problem which is described in Kessler et al. (1996) in which flow and transport in a one-dimensional dual-permeability (matrix and fractures) system was simulated. Good agreement was obtained between the current model and previous simulations.

# 5

## MODEL RESULTS USING AN AVERAGE RECHARGE RATE OF ONE MILLIMETER PER YEAR AS A BASE CASE

---

The first step in the modelling exercise was to discretize the domain described in Section 2. The finite-element mesh is shown in Figure 5-1. The mesh consists of 3683 nodes and 7149 elements. A dual-permeability approach was used in which each node in the initial finite-element mesh is duplicated, with one node representing the matrix and a second node representing the fractures, so the model domain actually has twice as many nodes as the initial 2D finite-element mesh. The HTS model was used to perform all simulations.

At the time when the initial modeling work was conducted (late 1996 and to 1997) the area-average infiltrating rate thought appropriate for Yucca Mountain was about 1 mm/yr. Thus, a constant, long-term infiltration rate of 1 mm/year was applied on the top boundary of the domain in this early work. In order to distribute the infiltration evenly between the matrix and fractured continua, a thin infiltration spreading layer was added to the top of the system. The pressure head was fixed at 0 (equivalent to 700 m total or hydraulic head) along the bottom. Both sides of the domain were assumed to be no flow boundaries, which represent flow divides or symmetry boundaries. The steady-state hydraulic head solution is shown in Figure 5-2. The legend labels  $H_m$  and  $H_f$  refer to hydraulic head in the matrix and fractures respectively.

The difference between the hydraulic head in the matrix and fractured continua (labeled as  $dH$ ) is shown in Figure 5-3. There are two zones where the head difference is approximately -80. The head difference is calculated here as matrix head minus fracture head, so negative  $dH$  values indicate higher fracture head and flow from fractures to matrix. We feel that the large difference in the zone near the top of the system is because of focused recharge (due to the infiltration spreading layer).

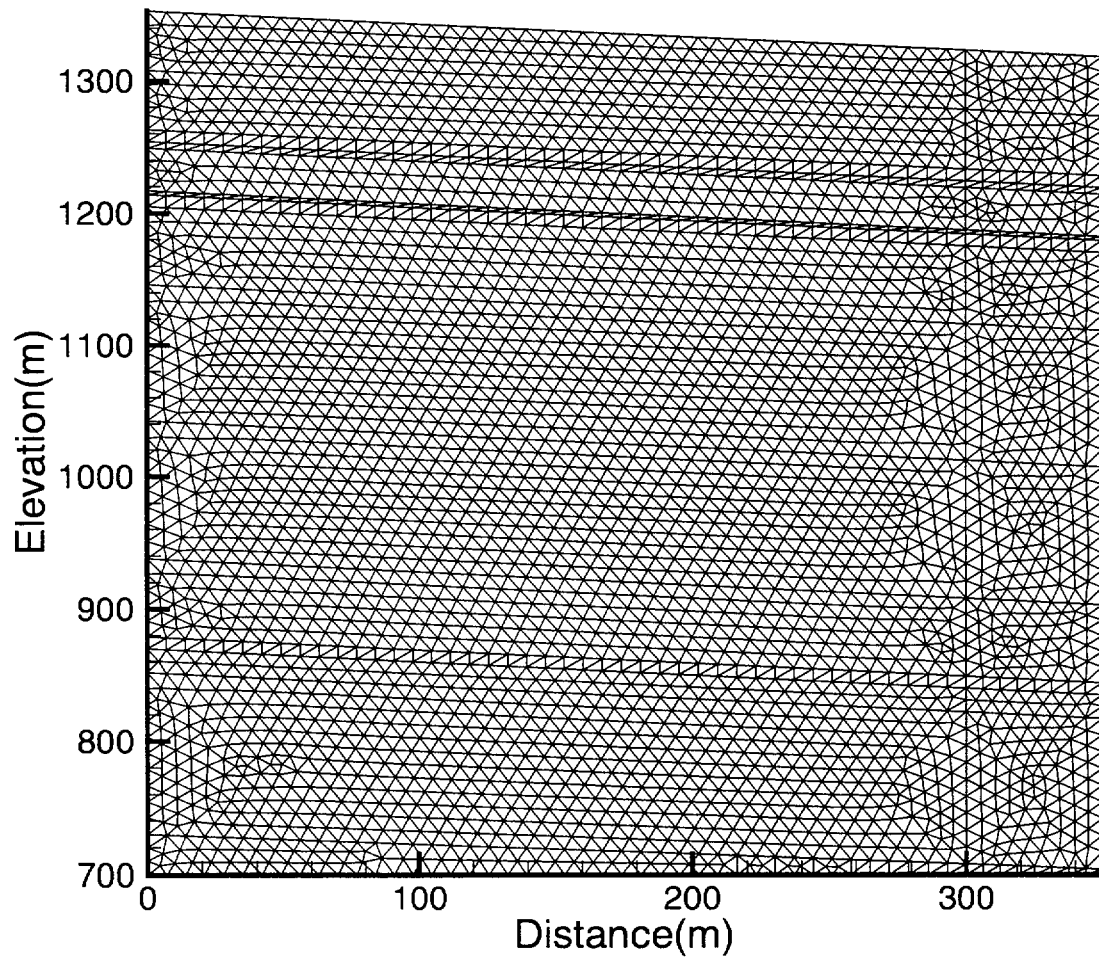


**Figure 5-1**  
**Finite-element mesh**

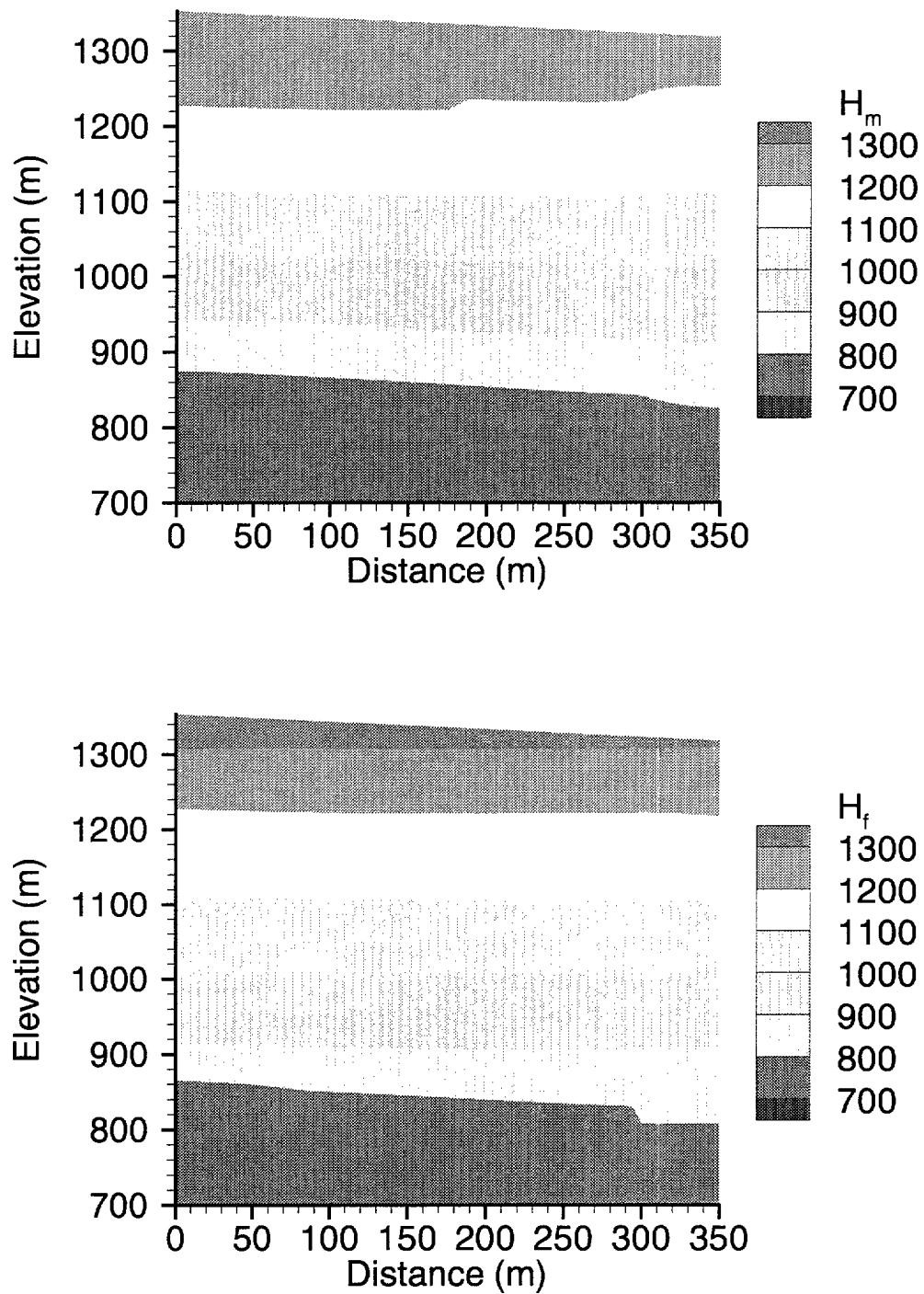


**Figure 5-2**  
Hydraulic head at steady-state

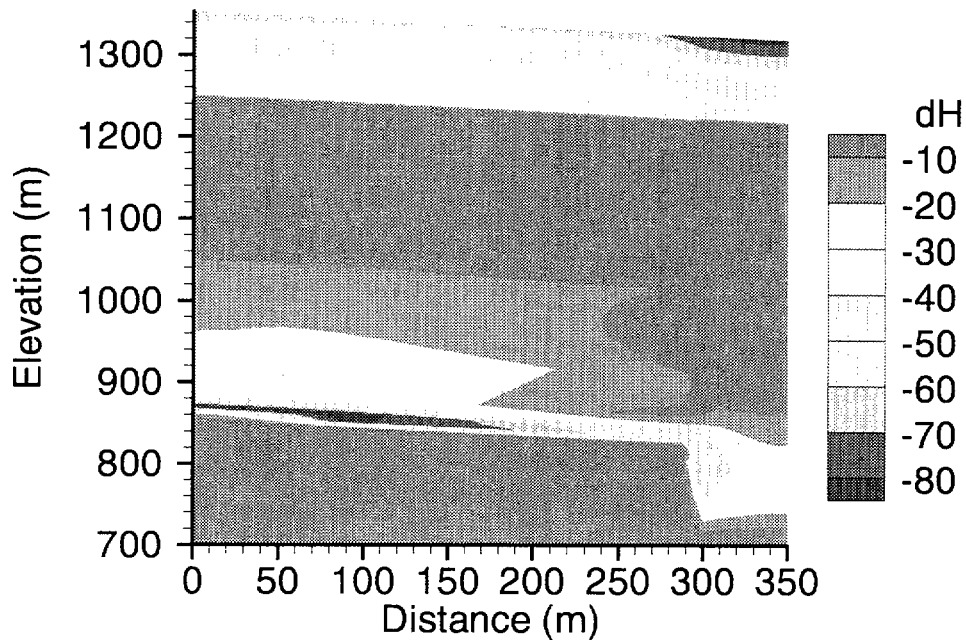


**Figure 5-3**  
**Matrix/fracture head difference,  $dH$  ( $H_m - H_f$ )**

However, near the base of the Topopah Spring formation (TSw) and to a lesser extent near the base of the Tiva Canyon formation (TCn) in the non-fault zone, there are other regions where the pressure differential is also large. We feel this could be caused by a buildup of water in the fractures prior to penetrating the lower layers. The steady-state saturations are shown in Figure 5-4. The matrix saturations are very high (0.9 or greater) throughout most of the cross-section, with the exception of the Paintbrush and Calico Hills Formations (CHn), which are both non-welded tuffs. On the other hand, fracture saturations are near residual throughout most of the cross-section.

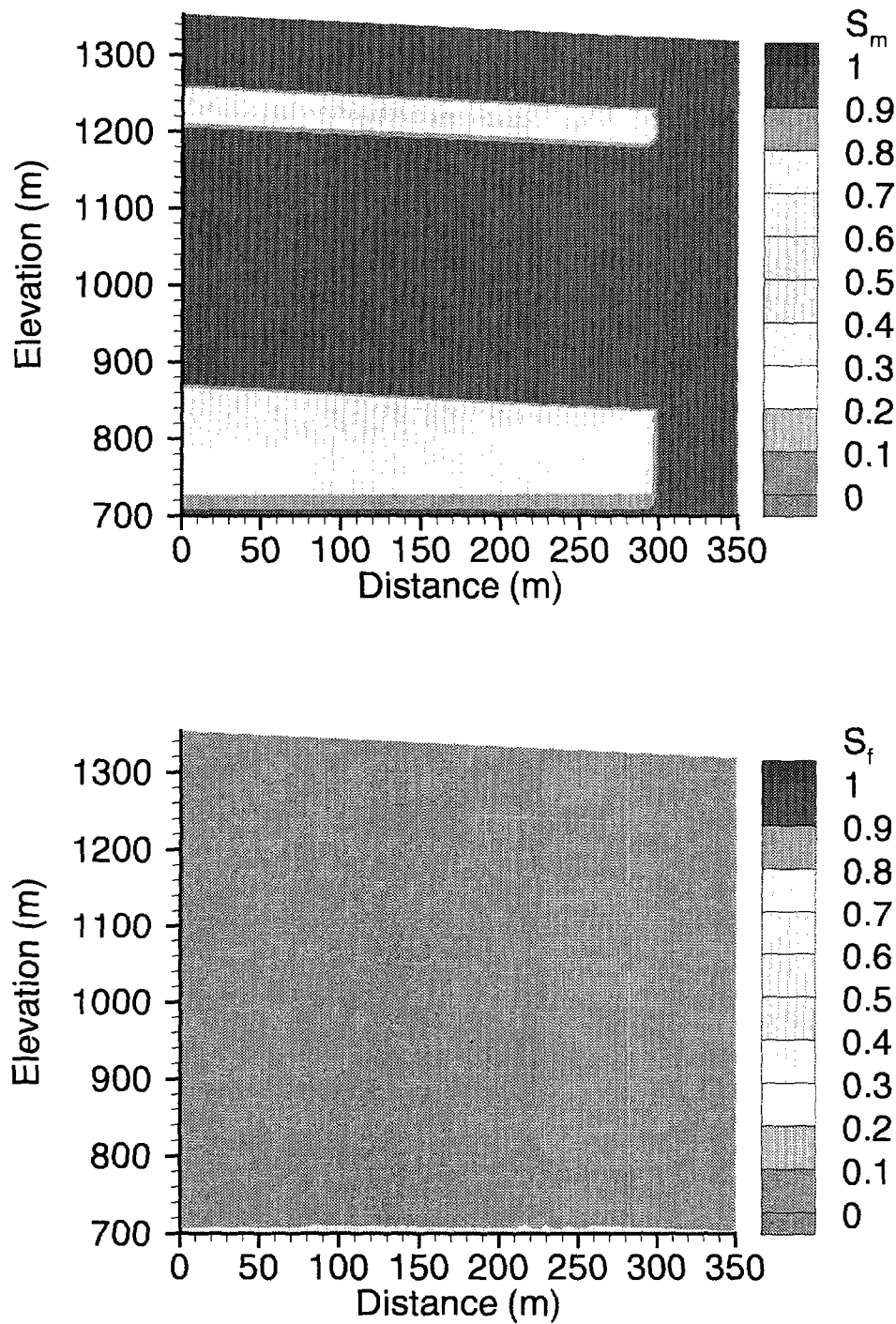


**Figure 5-4**  
**Saturation at steady-state**

## **5.1 Steady 1 mm/yr Recharge with Additional Recharge Pulses**

### **5.1.1 Case 1: Uniform Recharge**

The model was set up to simulate transport under steady-state flow conditions using the heads and saturations, shown in Figure 5-2 and Figure 5-4 respectively, as input. An initial background concentration of 500 (expressed as the ratio of  $^{36}\text{Cl}/^{35}\text{Cl}$ ) was assigned and a third-type boundary condition was applied along the top of the domain with an input concentration of 20,000. Decay of  $^{36}\text{Cl}$  was not considered in these simulations because the duration of the simulation time is relatively short (50 years) and the half-life of  $^{36}\text{Cl}$  is large (301,000 years). The resultant plume is shown at a time of 50 years in Figure 5-5, and has not penetrated very far into the system. The concentrations in the matrix and fractures are essentially the same, indicating that the system is in equilibrium.



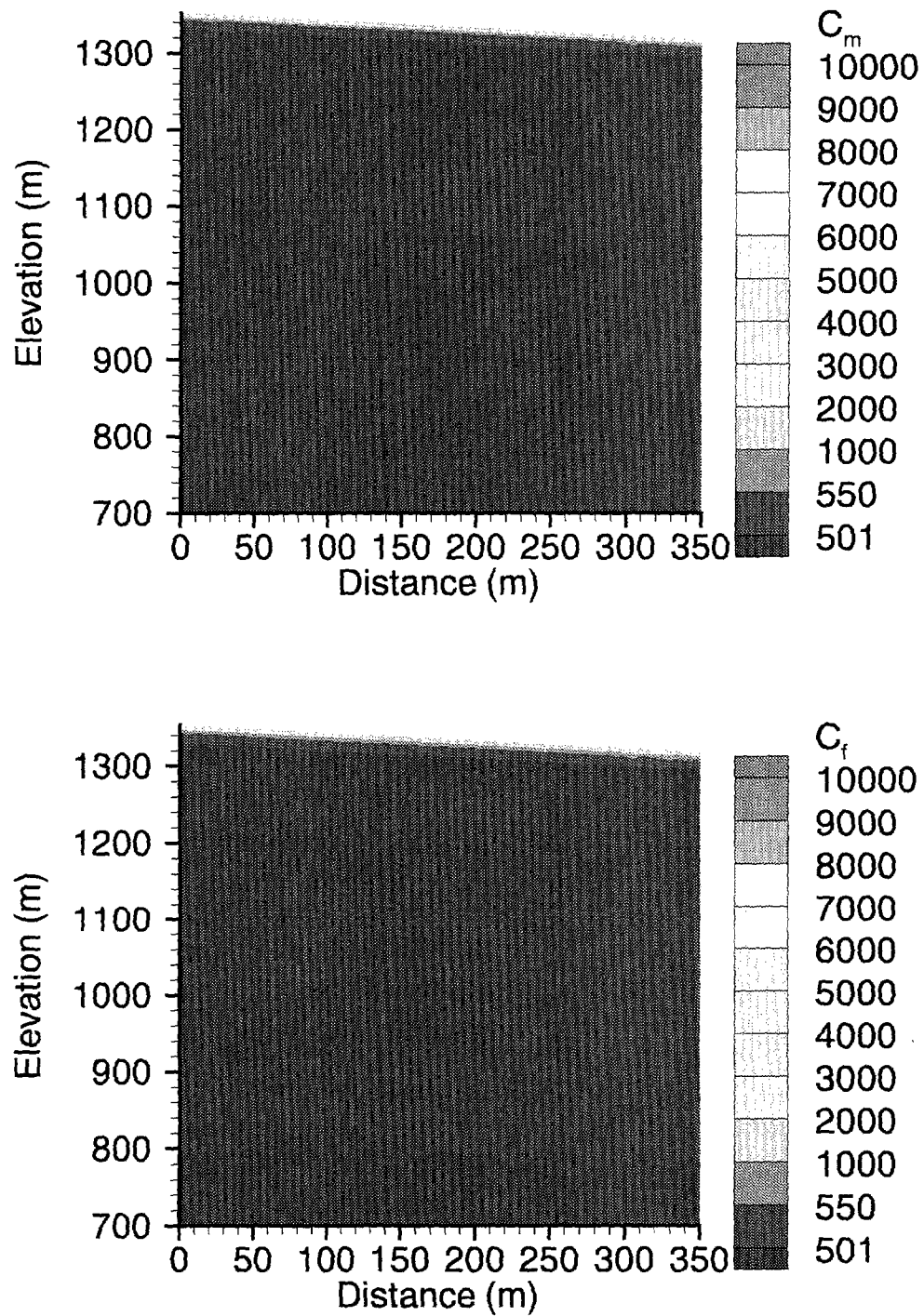


Figure 5-5  
Concentration at 50 years, Case 1

### **5.1.2 Case 2: Variable Recharge: 10 mm/week Infiltration Pulses**

This case is identical to Case 1 (Section 5.1.1), with the exception that after 10 years of infiltration at a rate of 1 mm/year, one week of infiltration at a rate of 10 mm/week was applied to the top of the fault zone only. This was repeated every 10 years. The duration of the simulation was again 50 years. The average annual infiltration rates over this period equals 1.0024 mm/year, expressed as a uniform value over the full length of the cross section.

Figure 5-6 shows the resultant plume at the end of the first 10 mm/week pulse (about 10 years since the start of the simulation). The plume has penetrated down most of the way through the Tiva Canyon formation at relatively high concentrations in the fractures. Concentrations in the matrix at that time are much lower, indicating that the system is not in equilibrium. It appears that the 10 mm/week pulse was sufficient to initiate rapid flow down the fractures.

Figure 5-7 shows the plume at a time of 50 years, after 4 recharge pulses (the last pulse occurs at 40 years). The contaminant plumes in the matrix and fractures are essentially the same. This is because the high concentrations observed at the end of a pulse have now flowed/diffused into the matrix blocks. Because the matrix porosity is high relative to the fracture porosity, it buffers the concentration so the peaks are much lower than we observed in the fractures at the end of the first pulse.

### **5.1.3 Case 3: Variable Recharge: 10 cm/week Infiltration Pulses**

This case is identical to Case 2 (Section 5.1.2), except that larger pulses of 10 cm/week were applied every 10 years at the top of the fault zone. As before, the background infiltration over the remainder of the surface was held constant at 1 mm/year. Over the 50 year period of the simulation, the average annual infiltration rate, expressed as a uniform value over the entire surface, is 1.027 mm/year.

Figure 5-8 shows the resultant plume at the end of the first 10 cm/week pulse (about 10 years since the start of the simulation). The plume has penetrated down to the top of the Paintbrush formation at relatively high concentrations in the fractures. Concentrations in the matrix at that time are much lower, similar to what was observed in Case 2.

There is a buildup of solute in the matrix near the toe of the plume in the lowest layer of the Tiva Canyon formation. This correlates well with a rise in fracture saturation in this region, which is shown in Figure 5-9. It appears that water is pooling in the fractures and is then flowing into the matrix. The larger quantities of water flowing into the matrix carry more solute and therefore, the buffering effect of the matrix is less noticeable, hence the concentrations are higher.

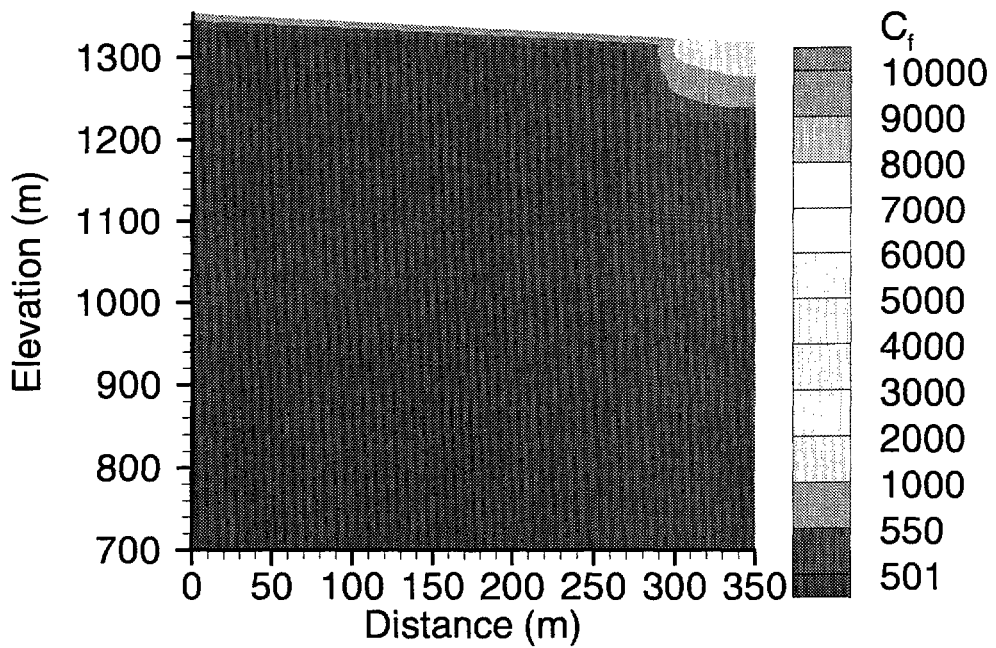
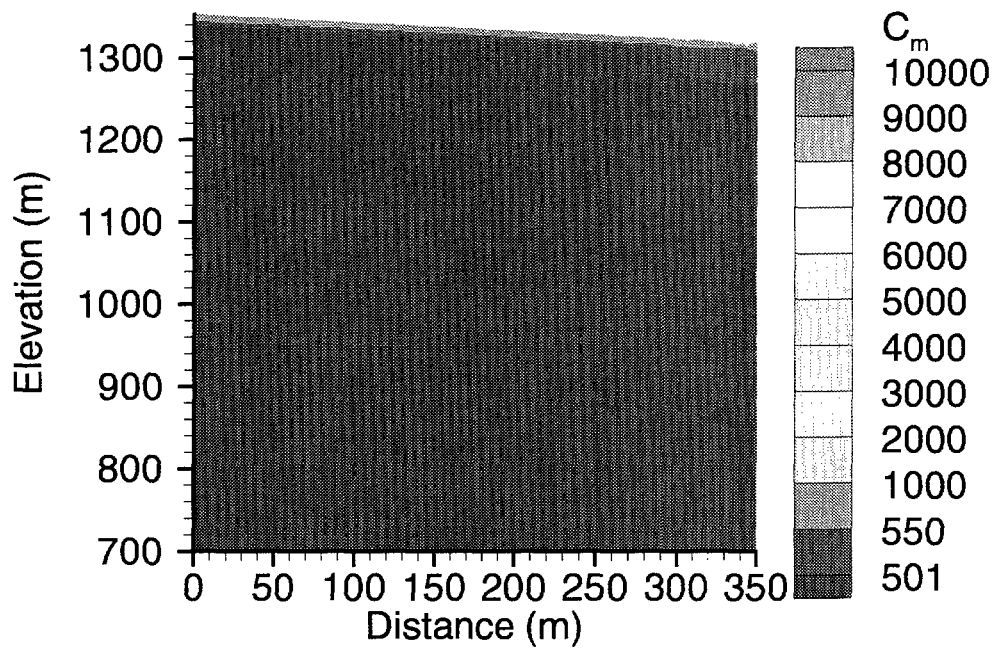


Figure 5-6  
Concentration at 10 years, Case 2

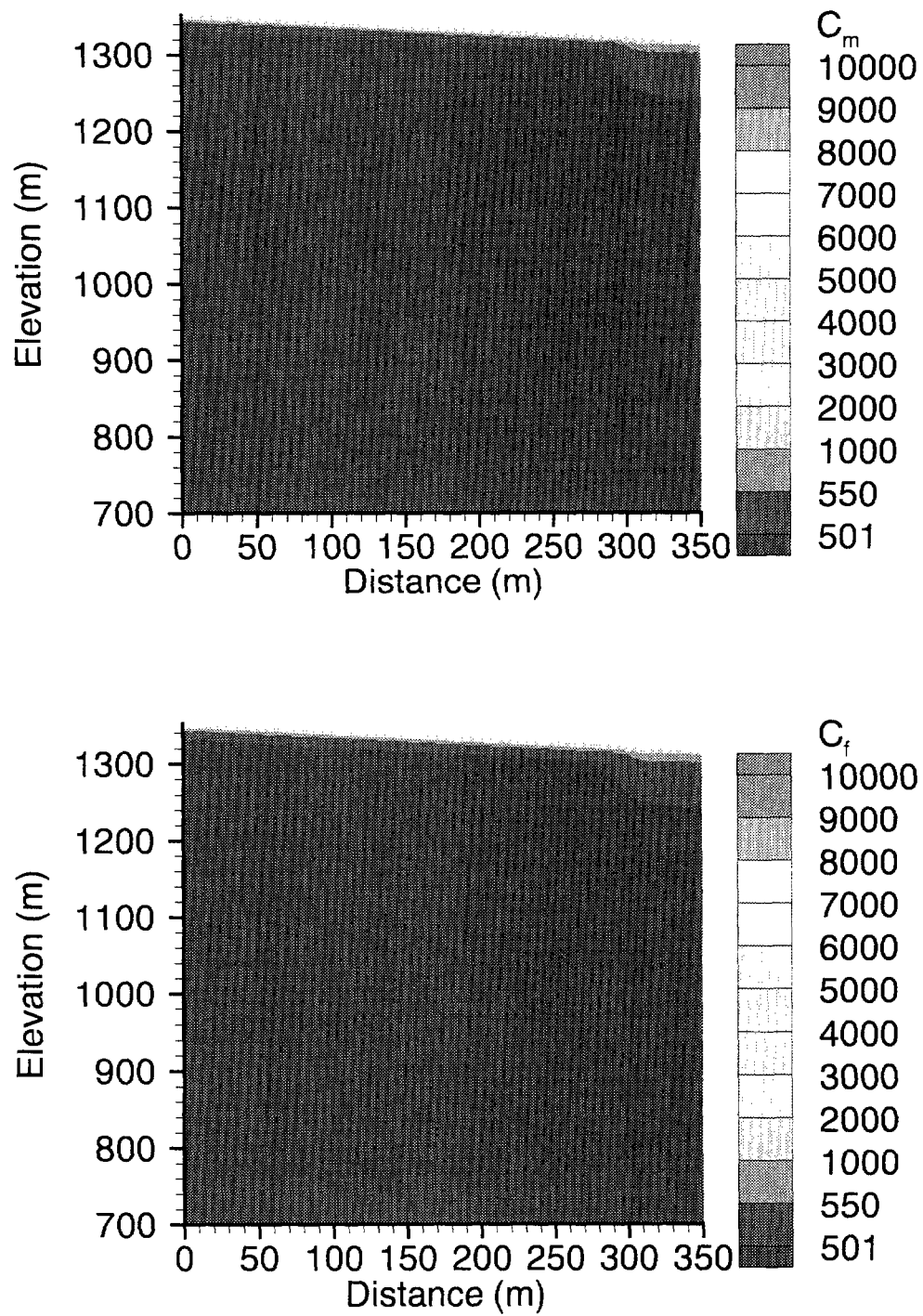


Figure 5-7  
Concentration at 50 years, Case 2

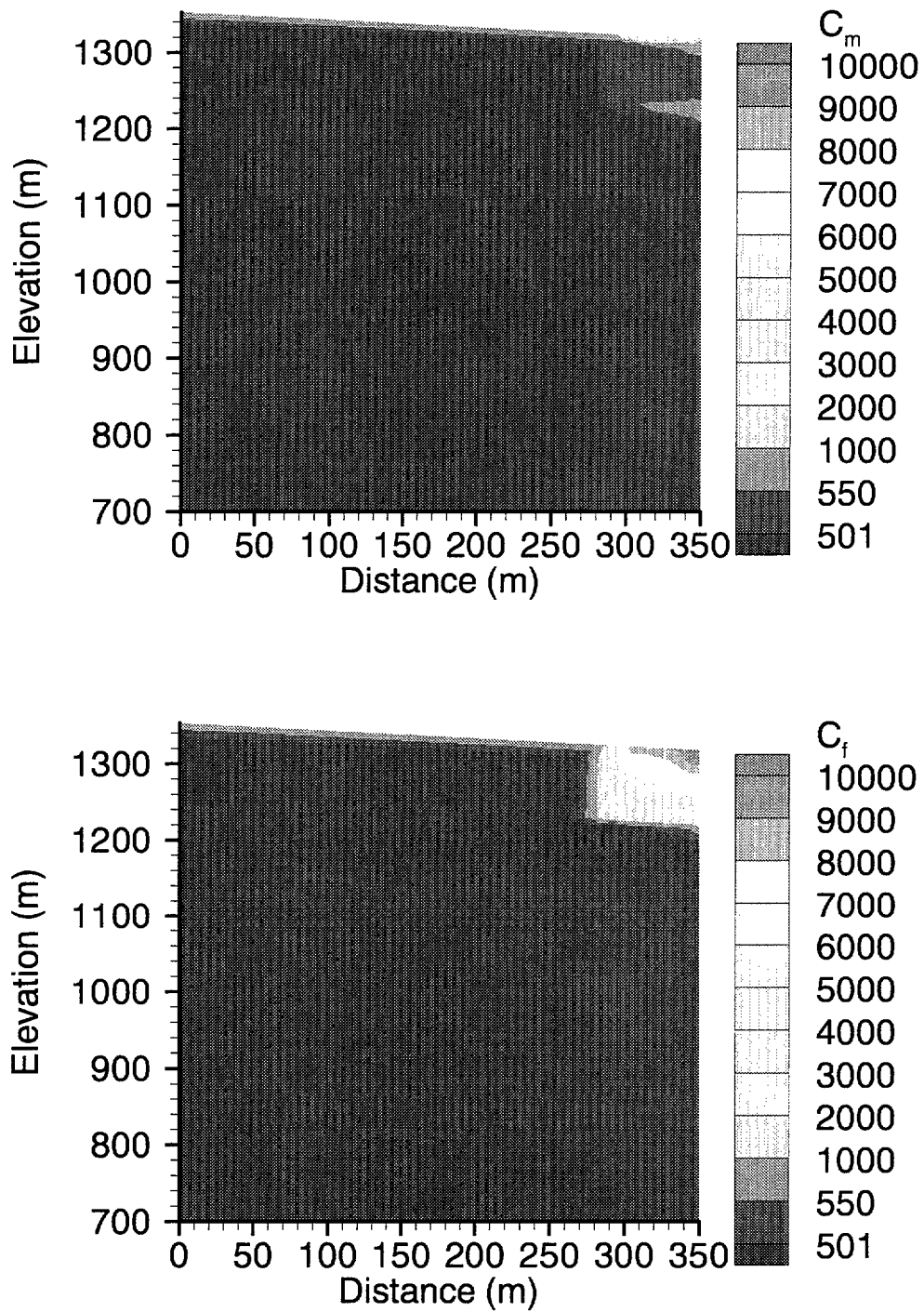
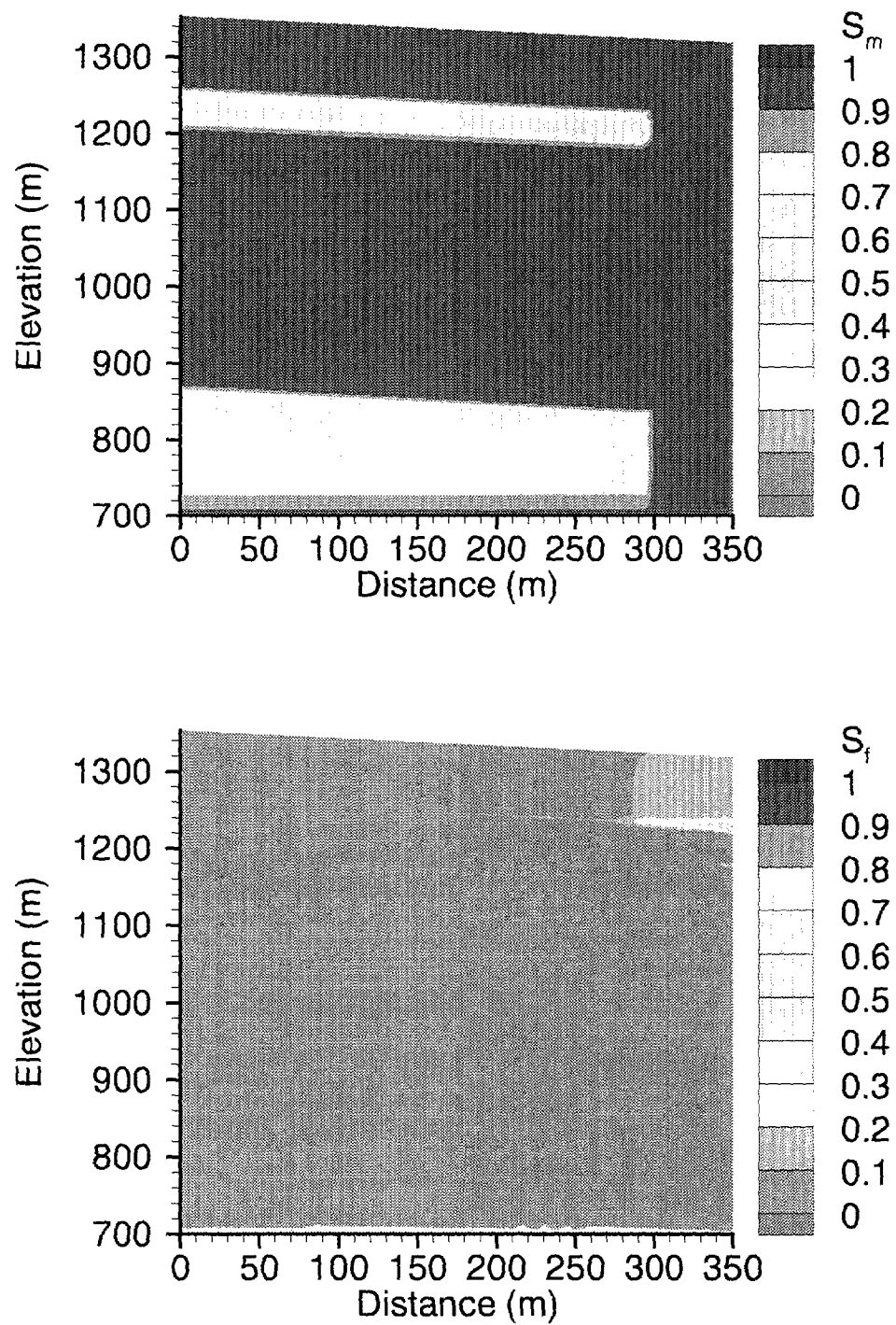


Figure 5-8  
Concentration at 10 years, Case 3



**Figure 5-9**  
**Saturation at 10 years, Case 3**

At a time of 50 years, after 4 recharge pulses the contaminant plumes in the matrix and fractures are again essentially the same, as they were in Case 2.

It appears that the properties of the Paintbrush Formation in the fault zone are holding up the advance of the solute plume. Figure 5-10 shows the Darcy flux vectors in the matrix and fractures around the region of the Fault zone TC/PT contact. These vectors have been scaled by magnitude, so that larger vectors show regions of active flow. It is clear that water is flowing preferentially through the matrix in this region, while in the fractures this is a zone of little or no flow. This would explain why vertical plume migration appears to cease at this contact, since the high matrix porosity would tend to buffer the concentration significantly.

#### ***5.1.4 Case 4: Variable Recharge: 10 cm/week Infiltration Pulses using Altered Paintbrush Formation Fault Zone Properties***

This case is identical to Case 3 (Section 5.1.3), with the exception that the Topopah Springs fault zone properties were substituted for those of the Paintbrush formation to see if the front would advance more rapidly.

Figure 5-11 shows the resultant plume at the end of the first 10 cm/week pulse (about 10 years since the start of the simulation). It can be seen that the front now penetrates the altered Paintbrush formation, indicating that the original properties of that formation were slowing down the vertical advance of the solute plume.

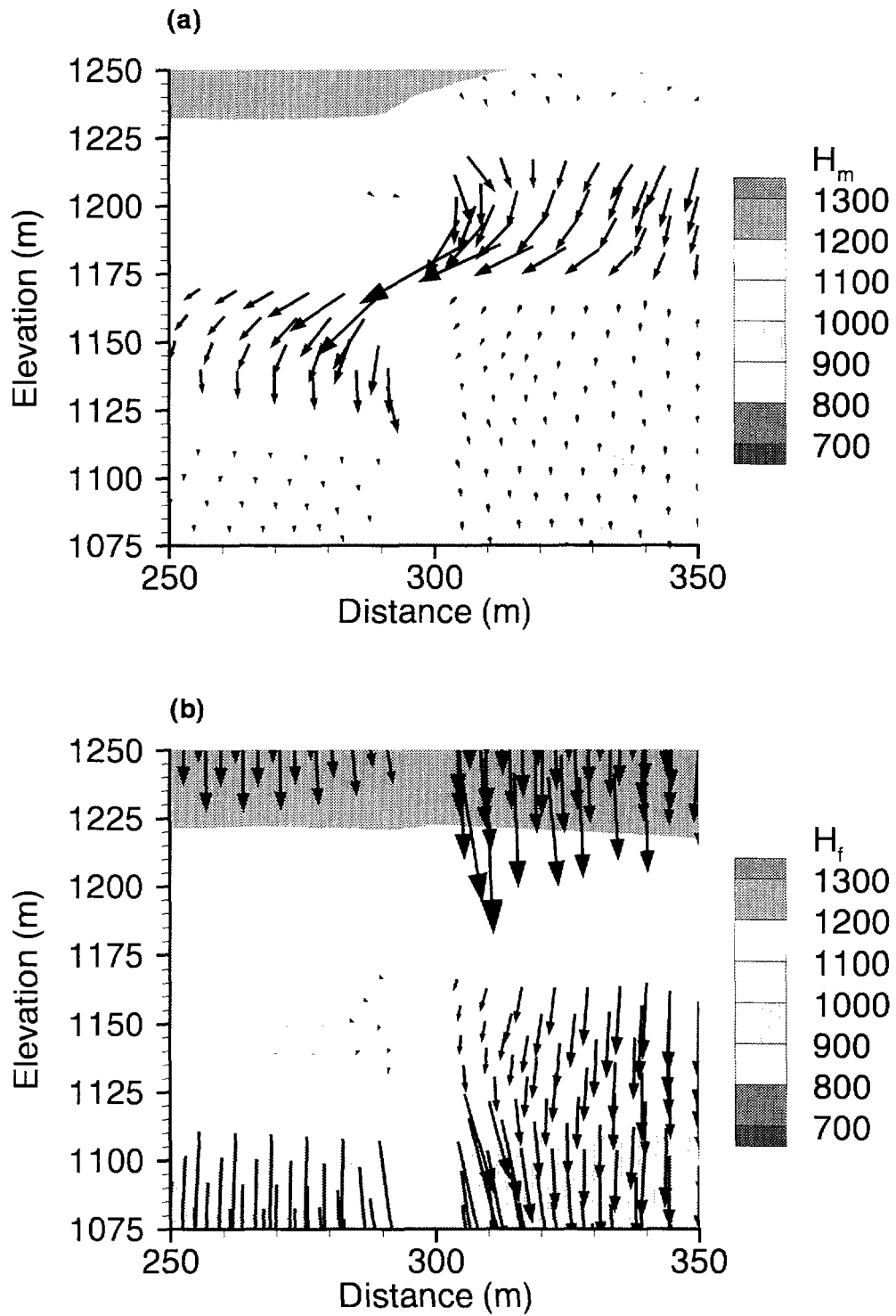


Figure 5-10  
Darcy flux vectors in (a) matrix and (b) fractures



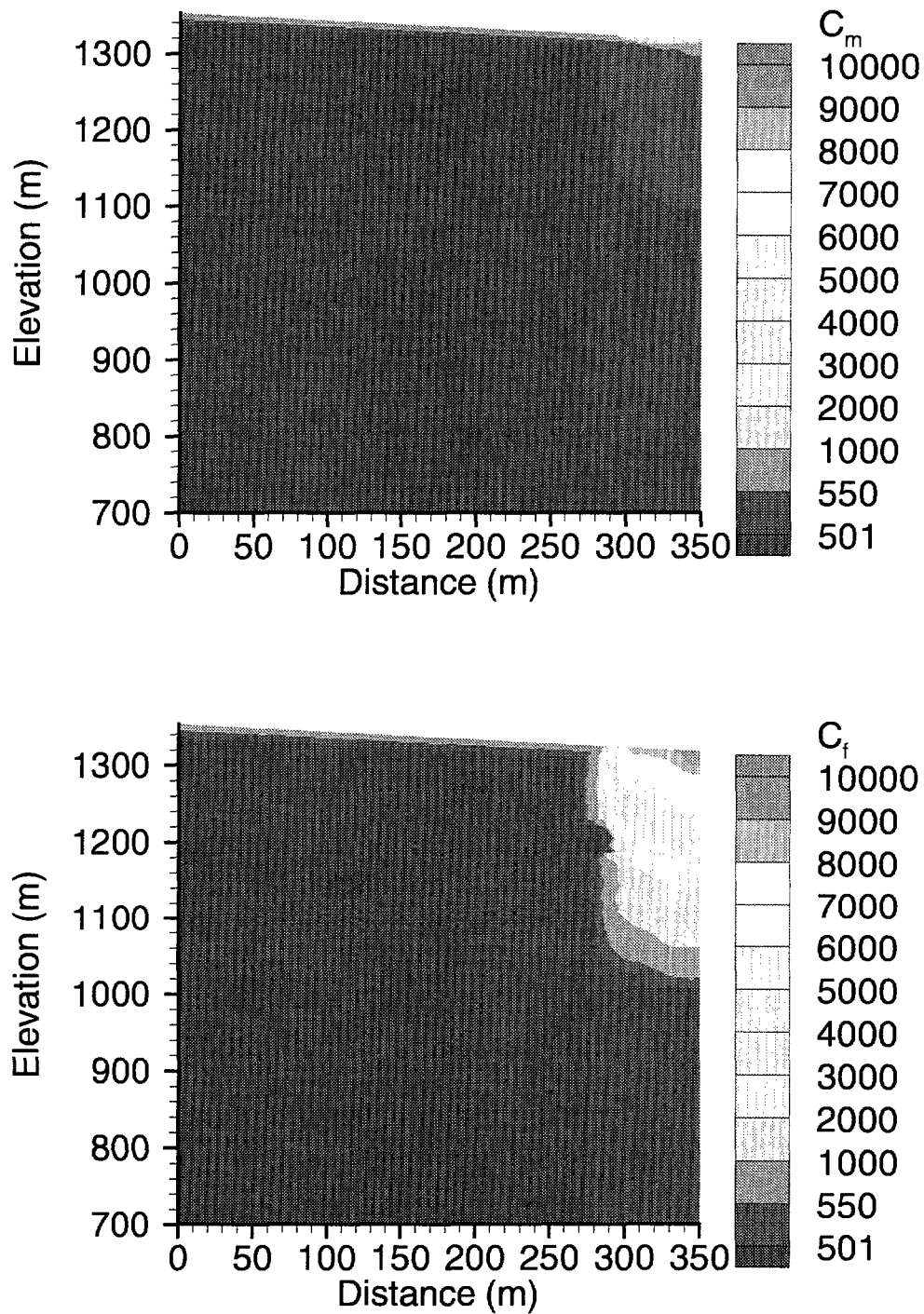


Figure 5-11  
Concentration after first 10 cm/week pulse, Case 4

## **5.2 Dual-permeability/ECM Comparison**

We used the generalized ECM (Equivalent Continuum Model) approach as outlined in Wu, Finsterle and Pruess(1996) to generate effective relative permeability and capillary pressure curves. One of the key assumptions of the ECM approach is equality of pressures between the matrix and fracture continua. This is clearly not the case as shown by the plot of pressure differential in the dual-permeability system for Case 1 (see Figure 5-2). For this reason, we would expect that the ECM approach would be unable to reproduce the results we saw above for the dual-permeability system.

Flow and transport boundary conditions were identical to those used for Case 1. Figure 5-12 is a plot of the dual-permeability matrix heads together with those of the ECM approach. The ECM head plot shows that the total hydraulic head at the top of the system at steady-state is somewhat higher than for the dual-permeability simulation. This would imply that the dual-permeability system is allowing water to percolate downward more freely, so that the head required to drive the water through the system is lower than in the ECM approach.

Figure 5-13 shows that saturations are much more uniform throughout the system in the ECM model than in the dual-permeability model.

### **5.2.1 Case 5: Uniform Recharge: DPM/ECM Comparison**

This case was identical to Case 1 (Section 5.1.1), except that the ECM steady-state flow field was used instead of the dual-permeability flow field. In this case, the results of the ECM approach were essentially the same as for the dual-permeability approach and will not be shown here. It appears that for low infiltration rates and relatively sluggish flow and transport situations the ECM approach works well.

### **5.2.2 Case 6: Variable Recharge: 10 mm/week Infiltration Pulses , DPM/ECM Comparison**

This case was identical to Case 2 (Section 5.1.2), except that the ECM steady-state flow field was used instead of the dual-permeability flow field.

Figure 5-14 shows that after 50 years, the plume has penetrated further into the domain in the dual-permeability system than in the ECM system. It appears that the mechanism of fast movement through the fractures during high-recharge events has been lost in the ECM approach.

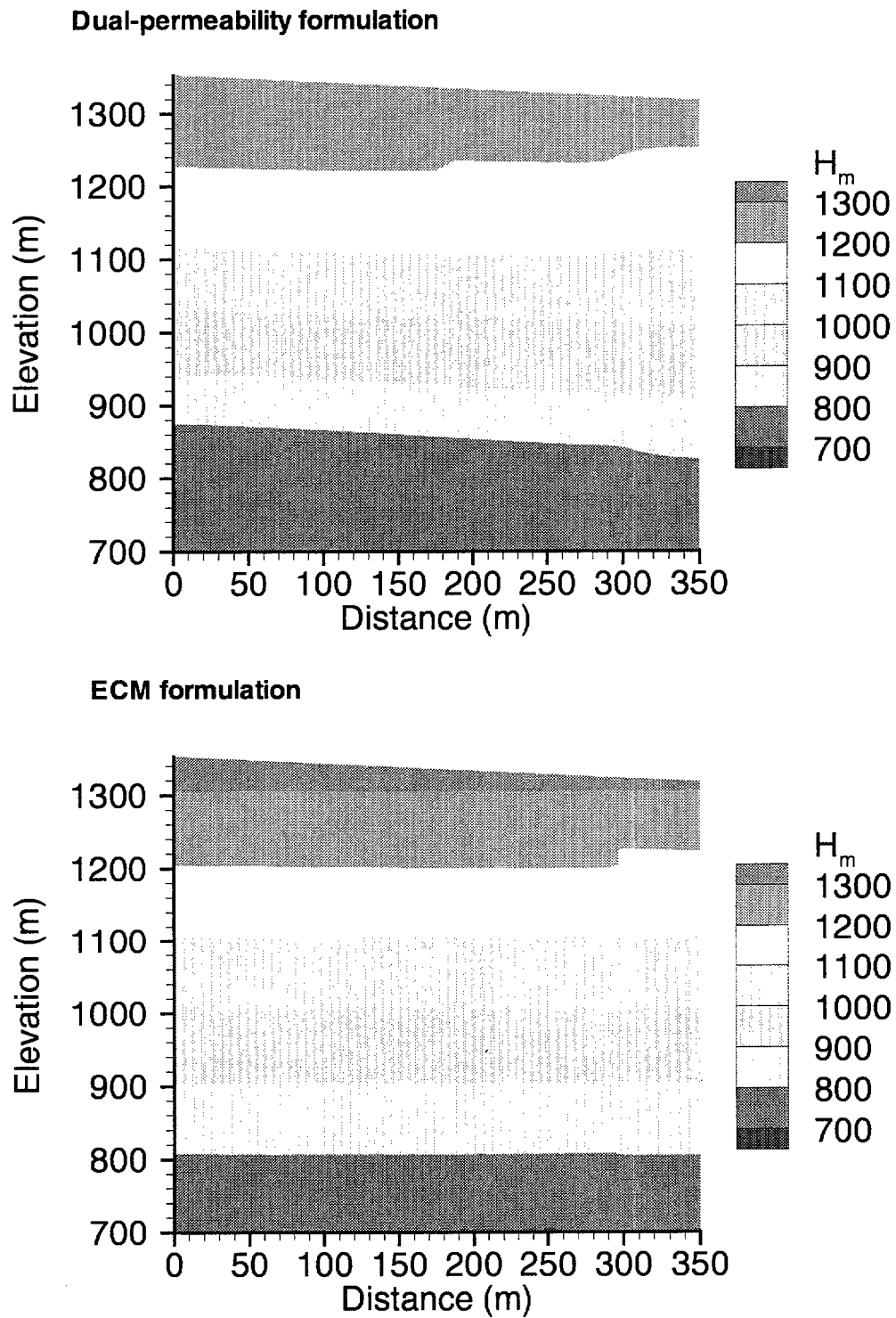
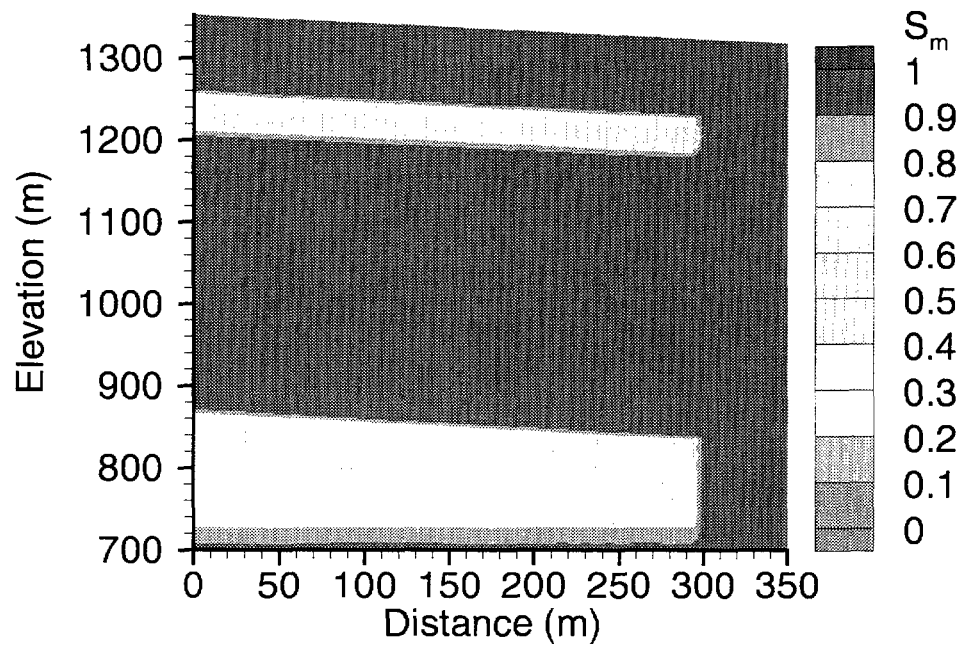
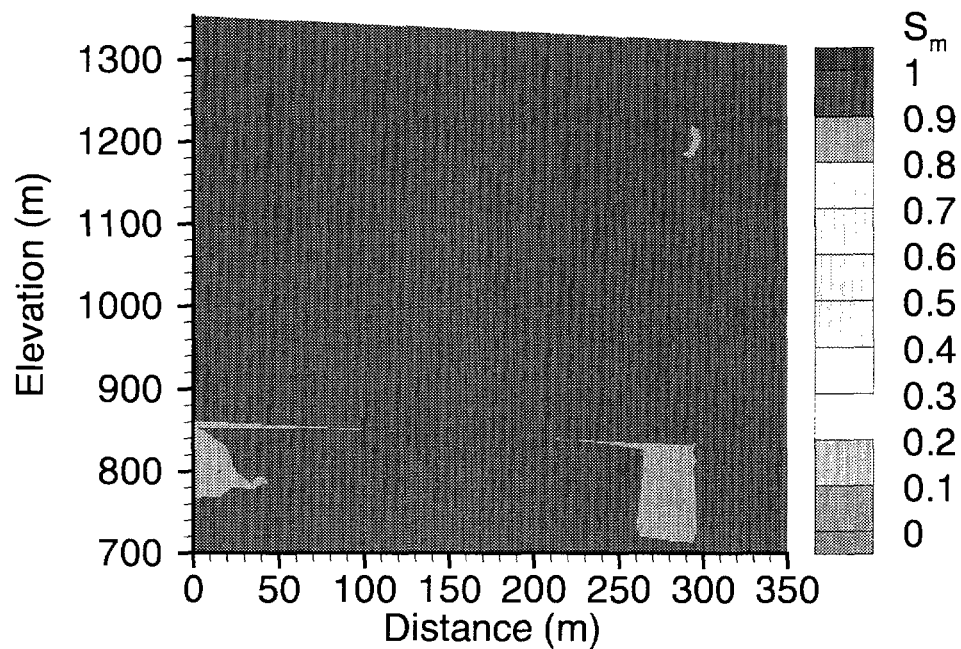


Figure 5-12  
DPM/ECM hydraulic head at steady-state

**Dual-permeability formulation**



**ECM Formulation**



**Figure 5-13**  
**DPM/ECM saturation at steady-state**

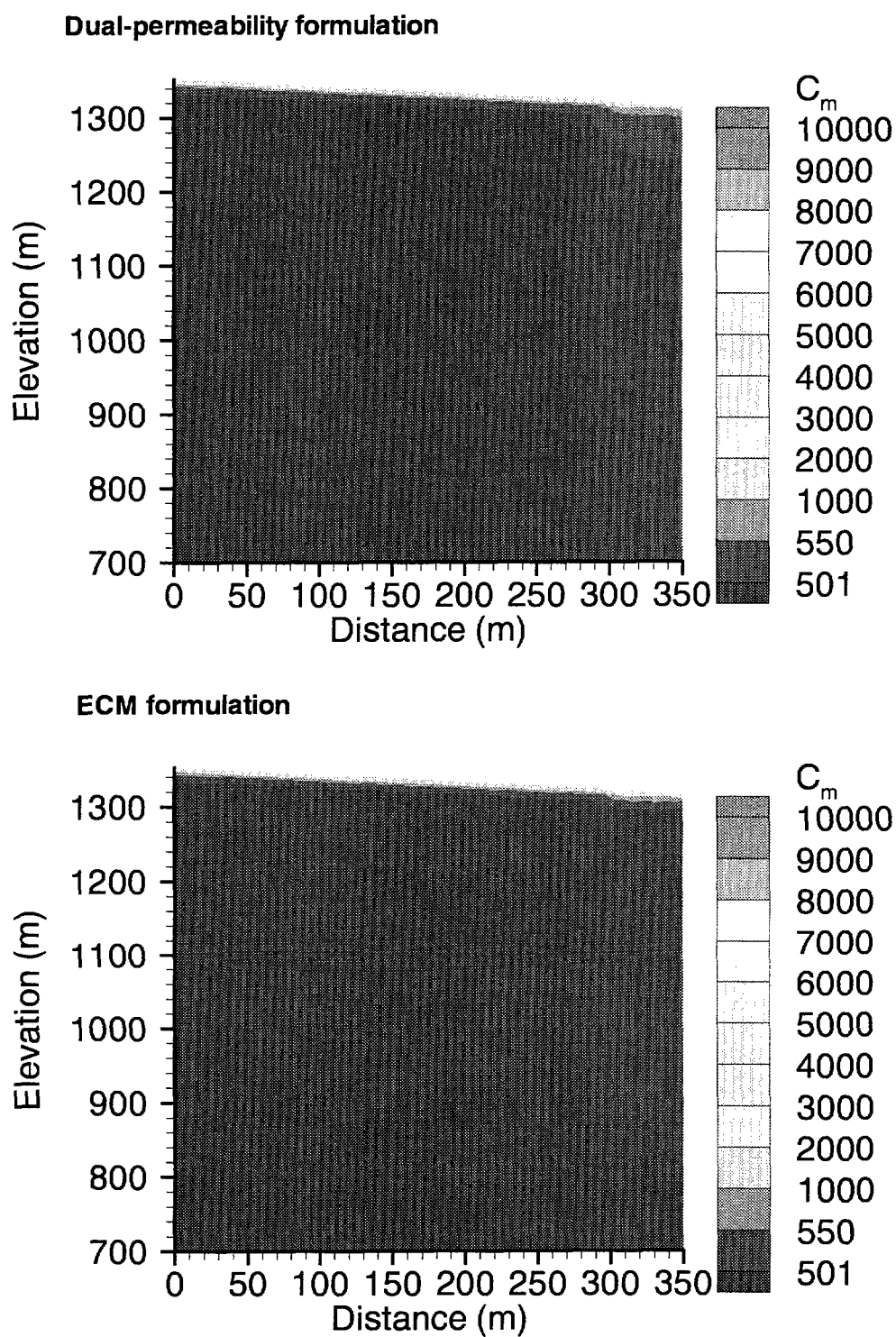


Figure 5-14  
Concentration at 50 years, Case 6

### **5.2.3 Case 7: Variable Recharge: 10 cm/week Infiltration Pulses , DPM/ECM Comparison**

This case was identical to Case 3 (Section 5.1.3), except that the ECM steady-state flow field was used instead of the dual-permeability flow field.

Figure 5-15 shows more dramatically that the ECM approach is unable to simulate the mechanism of fast fracture flow as seen in the dual-permeability results.

We conclude that the ECM formulation is unable to simulate the observed fast fracture flow at Yucca Mountain, and for this reason we did not explore any other variants of the ECM approach.

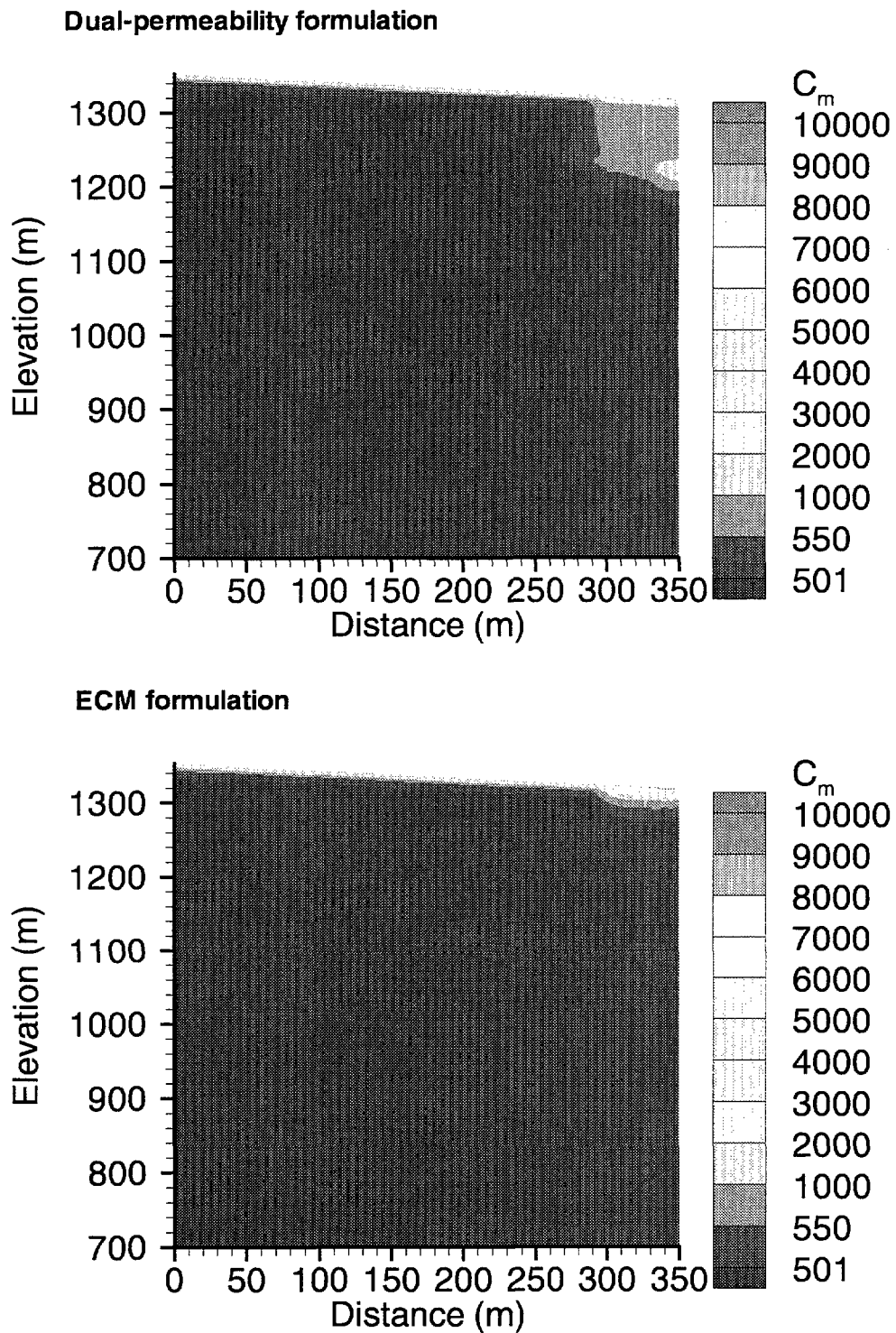


**Figure 5-15**  
**Concentration at 50 years, Case 7**

### 5.3 Flux Diversion

One of the objectives of the modelling exercise was to determine how much infiltrating water was diverted laterally into the 50 meter wide fault zone.

Figure 5-16 shows the lateral distribution of the vertical component of the Darcy flux in the matrix and fractures just below the base of the infiltration spreading layer. Note that this data is taken from Case 1, which used the original unaltered Paintbrush fault zone properties. It is clear that the fracture flow is dominant, and the flux is spread fairly evenly over the width of the cross-section. The value for the fractures is approximately equal to the infiltration rate of 1 mm/year (expressed on the plot as  $2.74 \times 10^{-6}$  m/day). This indicates that for the low, long term infiltration rate, the infiltration spreading layer is not diverting water laterally to the fault zone.

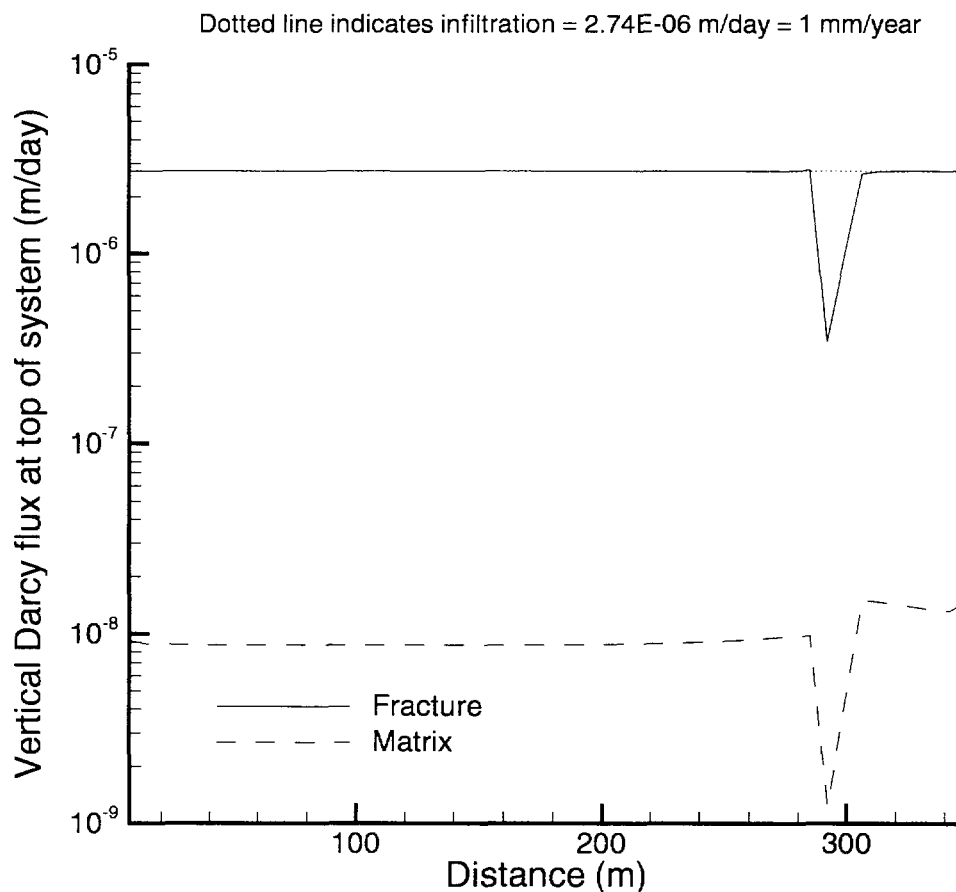


**Figure 5-16**  
Vertical component of Darcy flux near the base of the infiltration spreading layer



Figure 5-17 shows the lateral distribution of the vertical component of the Darcy flux in the matrix and fractures at the repository level (assumed to be at an elevation of 1085 m for the purpose of this exercise). In this case, we see that the fracture Darcy flux has dropped to a level of about  $1 \times 10^{-8}$  m/day at the left side of the domain and rises to a value of about  $6 \times 10^{-6}$  m/day approaching the contact of the fault zone. The matrix Darcy flux is fairly uniform in the non-fault zone at a value of  $6 \times 10^{-6}$  m/day. The repository level is in the region where flow is being diverted into the non-fault zone (see Figure 5-10).

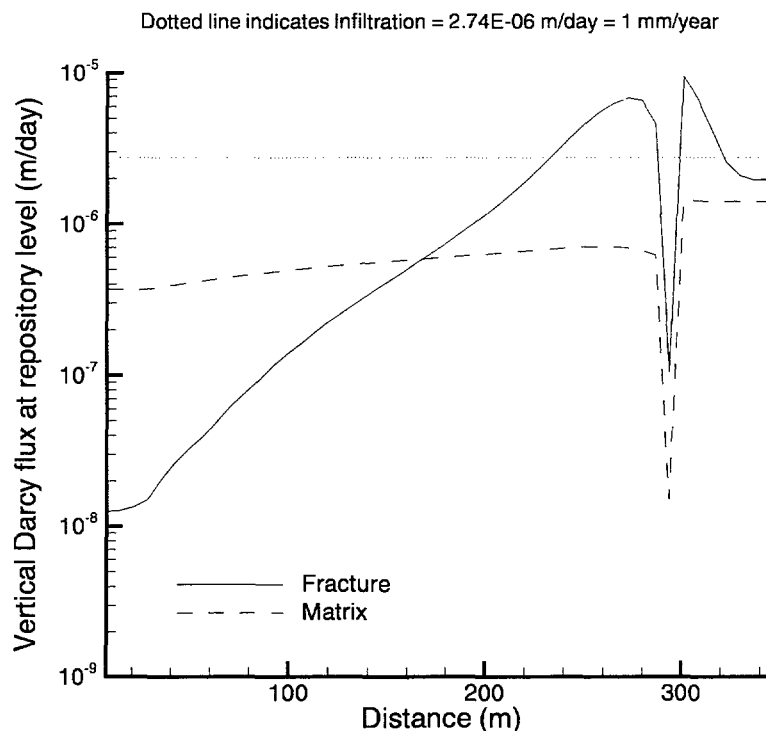


**Figure 5-17**  
Vertical component of Darcy flux near the repository level

In order to determine how much infiltrating water was being diverted laterally into the fault zone, the area under the vertical Darcy flux curves for both the matrix and fractures from  $X$  equals 0 to  $X$  equals 300 m (i.e. to the edge of the fault zone) was calculated. This yields the total water flux moving downward in this region. We carried out this calculation at the top of the system and at the repository level and the results were compared to determine the amount of lateral diversion. For a long term infiltration rate of 1 mm/year, the calculated lateral flux diversion was 28%. For 2 mm/year, the lateral flux diversion increased to 51%. Finally, for 2 mm/year and with the altered Paintbrush fault zone properties, the lateral flux diversion increased to 79%.

## 5.4 Long-term Periodic Infiltration

The purpose of this simulation was to assess the long term effect of periodic infiltration events of 10 mm/week every 10 years on the steady-state flow system which was established using a constant rate of infiltration of 1 mm/year. The 10 mm/week pulses were applied only to the top of the fault zone, with a uniform value of 1 mm/year being used elsewhere. We would expect some impact since a background rate of 1 mm/year with a 10 mm/week rainfall event every 10 years averages out to 2 mm/year over the long term.

In order to assess this, we extended the end time of Case 2 to approximately 500,000 days (1370 years). Again, note that we are using the original unaltered Paintbrush fault zone properties. In our discussion, we will refer to 4 points in the system which we have labeled A, B, C and D, the locations of which are shown in Figure 5-18. The first 3 points are near the top, middle and base of the fault zone respectively, and the fourth point is located in the non-fault zone at about the center of the domain.

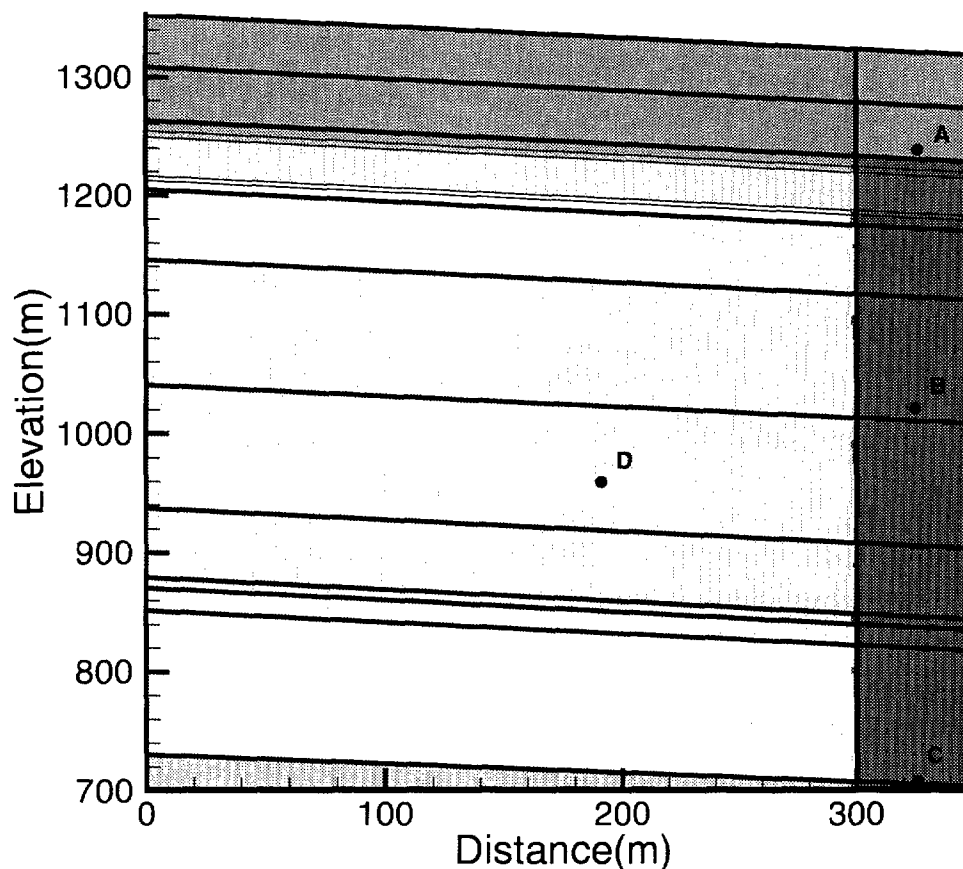


Figure 5-18  
Location of points A,B,C and D

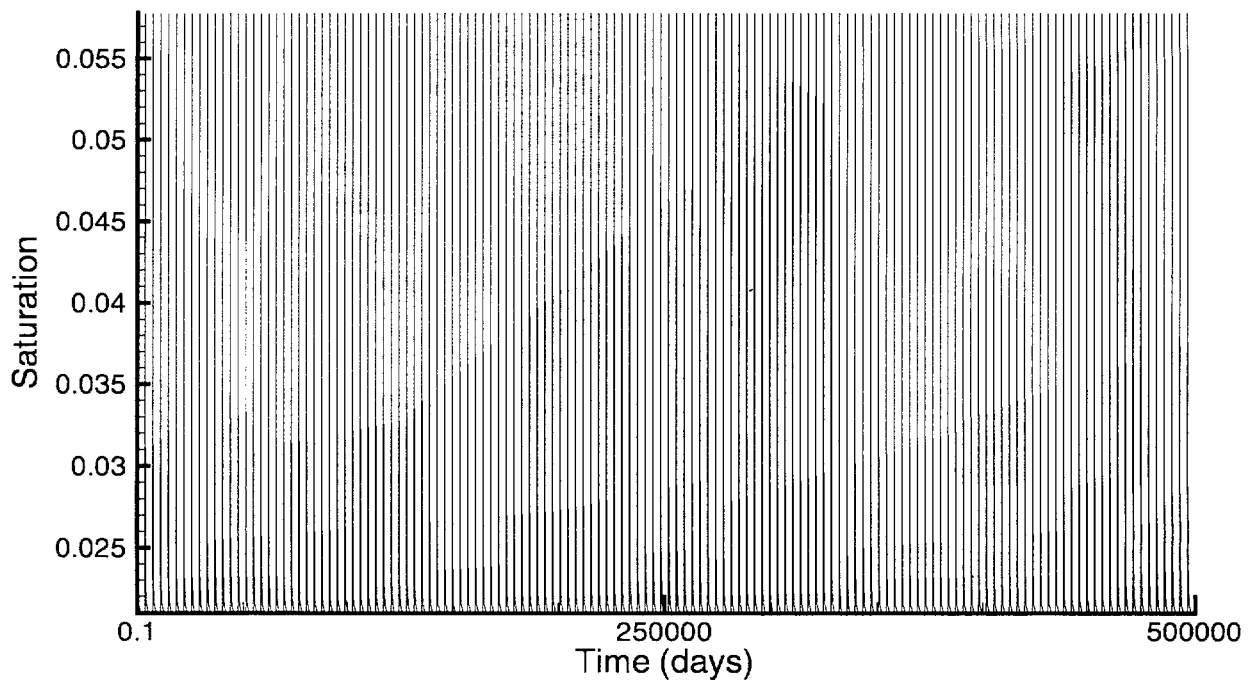
Figure 5-19 shows the saturation in the fracture at Point A. Because of the time scale of the plot, it is difficult to discern that the saturation at point A shows a repeated pattern in which it rises rapidly to a value of about 0.0578 and then falls more gradually back to a value close to its initial saturation of 0.0209. Figure 5-20 is a detailed plot of the initial pulses at point A in the fracture. The first recharge pulse reaches point A after about 3 days and rises to its peak value after about 10 days. It then takes about 1000 days to decay back to its initial level. This behavior is repeated throughout the simulation, and after 500,000 days, there has been an increase in the peak saturation of only  $1.47 \times 10^{-5}$  and in the background saturation by  $5.4 \times 10^{-6}$ .

Figure 5-21 shows the saturation in the matrix at point A. It displays a gradual long term increase over the course of the simulation, for a total increase of  $2.6 \times 10^{-3}$ . It is evident that some of the recharge water is being absorbed by the matrix over the long term, as would be expected. Small jumps in the curve, which correspond to the recharge events, are just visible at this scale.

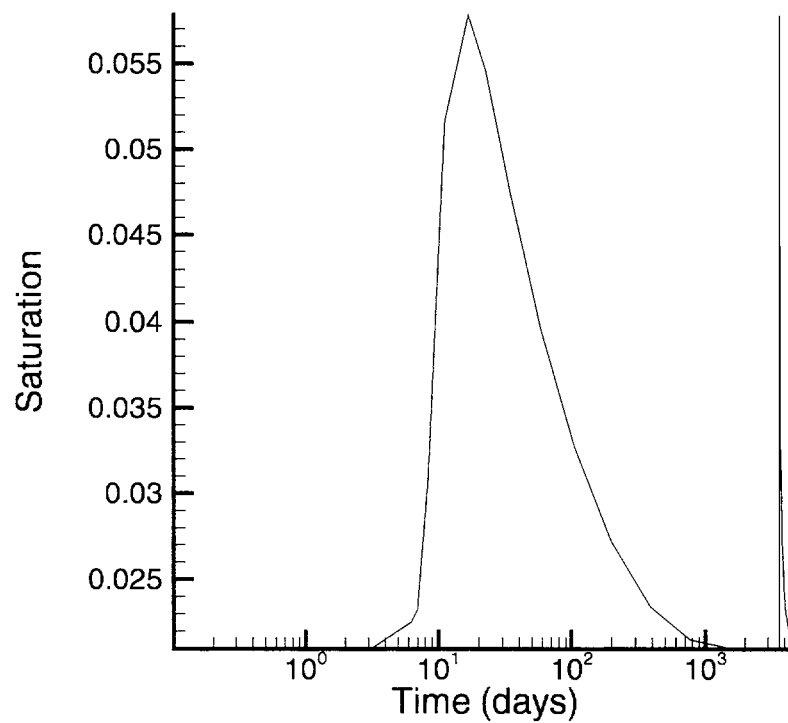
Figure 5-22 is a plot of the saturation in the fracture at points A, B, and C for the first 5 pulses. It shows that as we go deeper in the fault zone, the dramatic peaks in the fracture saturation at point A are dampened out, probably by absorption of the recharge water by the porous matrix, and that by the time we reach point C at the base of the fault zone, the rise in fracture saturation is relatively smooth.

Figure 5-23 is a plot of the concentration in the fracture and matrix at point A. The fracture concentration history appears similar to the saturation history at this point, with dramatic peaks matching the fracture saturation response. The matrix, has a series of step-like rises which correspond to the peaks in the fracture, as the solute rapidly enters the porous matrix. No rise in solute concentration above background was seen at points B or C in either fracture or matrix, indicating that most of the solute had been absorbed by the matrix above these points.

Figure 5-24 is a plot of the long term response of fracture saturation at point D, near the center of the fault zone. This response is smooth, due to the matrix buffering effect noted above, and appears to be approaching steady-state asymptotically. Figure 5-25 is a plot of the long term response of matrix saturation at point D and shows that the rate of change of saturation is still increasing at the end of the simulation, and does not appear to be as close to steady-state as the fractures at this point. This indicates that regions of the system which are not in close proximity to active fault zones may take an exceedingly long time to reach equilibrium with respect to changes in infiltration at the surface.



**Figure 5-19**  
Saturation in fracture at point A



**Figure 5-20**  
Detail of saturation in fracture at point A

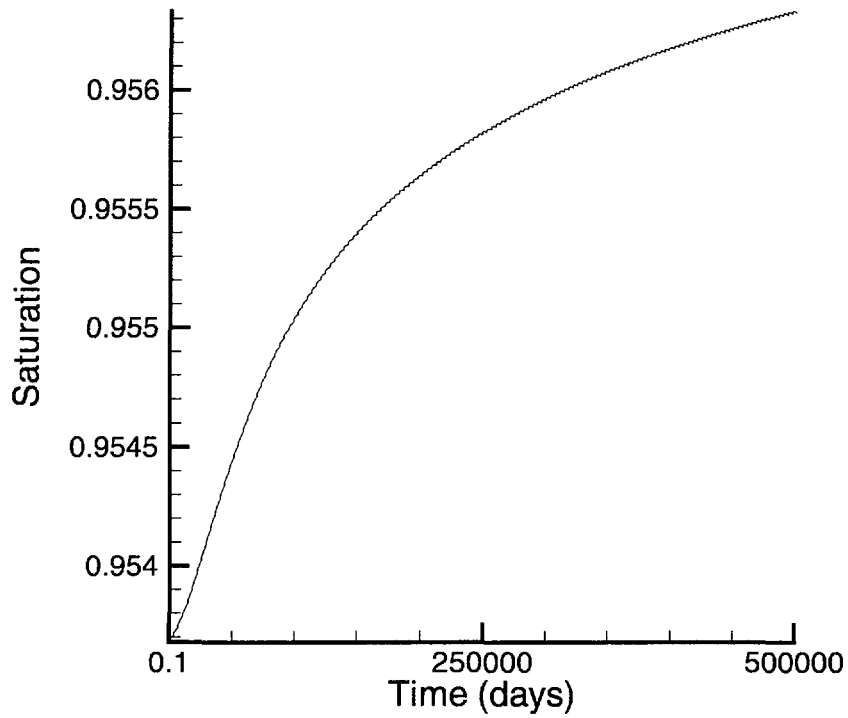


**Figure 5-21**  
Saturation in the matrix at point A

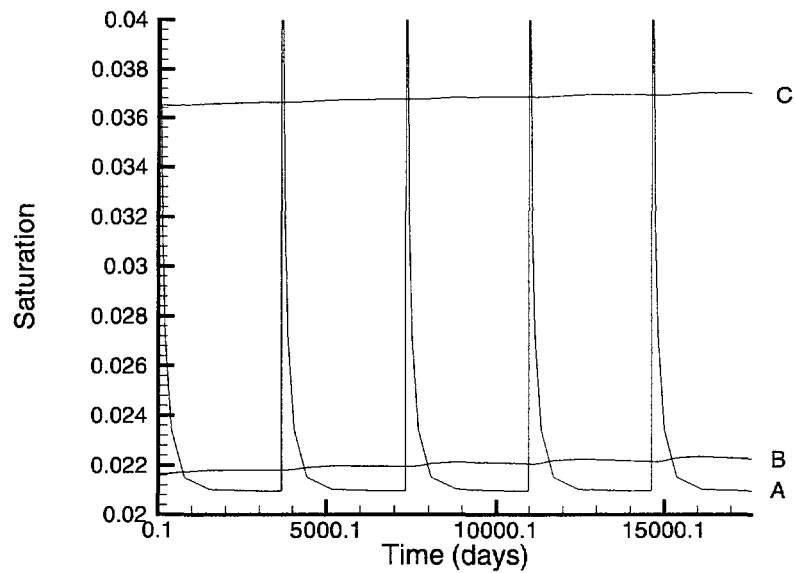


**Figure 5-22**  
Saturation in fracture at points A, B and C

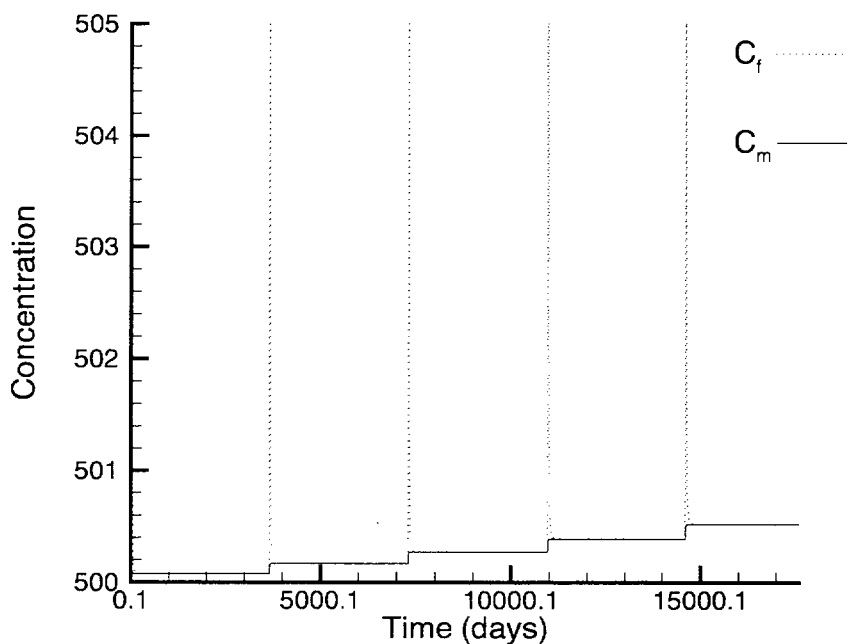


**Figure 5-23**  
Concentration in matrix and fracture at point A

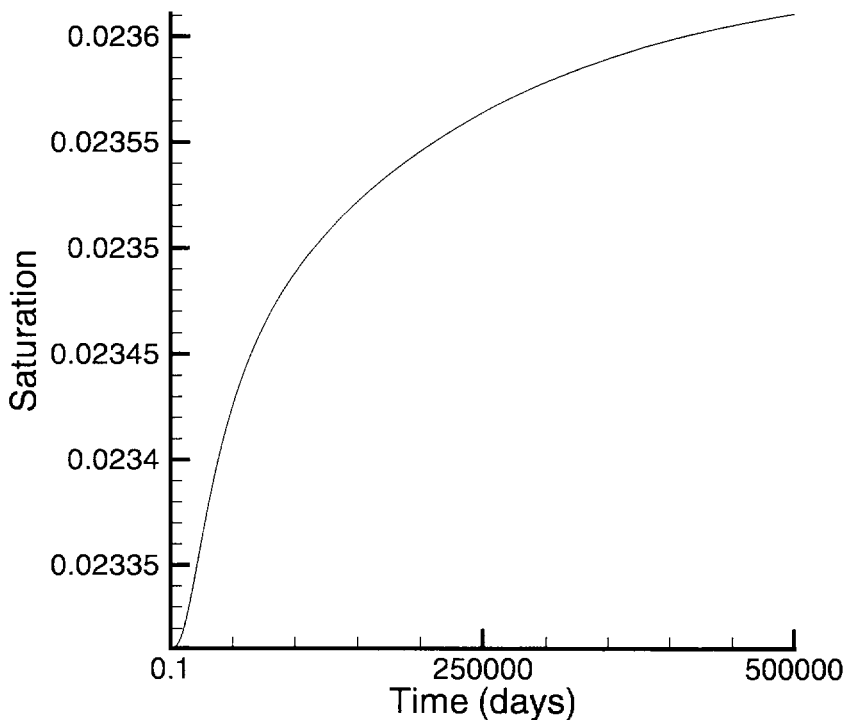


**Figure 5-24**  
Saturation in fracture at point D

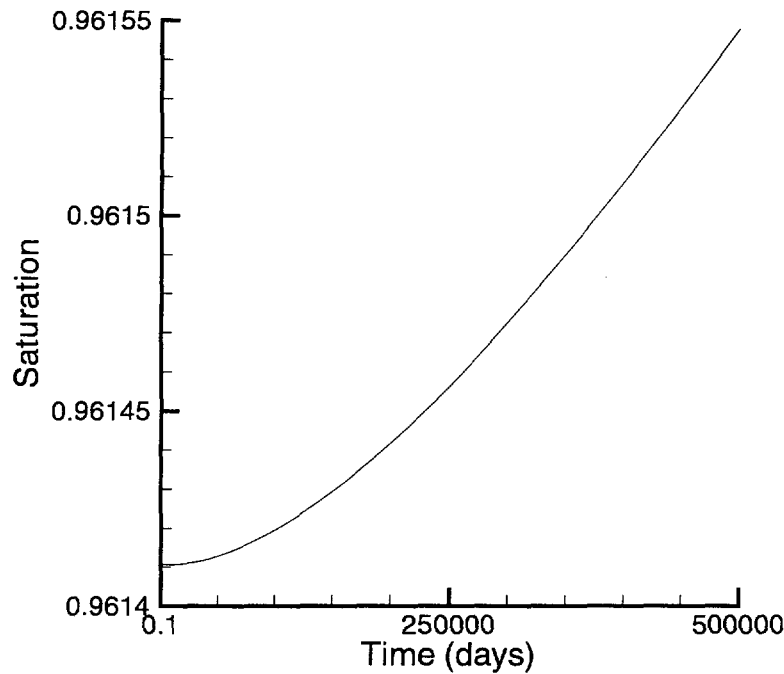


**Figure 5-25**  
**Saturation in matrix at point D**

It is evident that the end time of the simulation would have to be extended significantly in order to reach a steady-state flow regime. Unfortunately, due to the periodic nature of the recharge, the computer model cannot take large timesteps, making it impractical to achieve a steady state solution in a reasonable time for this situation.

The total change in matrix saturation for point A (which showed the most dramatic absolute increase) over the course of the simulation was only about 0.25% of the initial saturation, indicating that even at steady-state, the absolute change in saturation would be quite small when compared to the earlier steady-state flow system under a constant infiltration of 1 mm/year. This is perhaps not surprising when it is noted that the matrix under those conditions was already approaching saturation. As a test, we performed a steady-state simulation using a long-term infiltration rate of 2 mm/year. Plots of head and saturation were almost identical to the results of the original steady-state flow system achieved with 1 mm/year long term infiltration rate. Table 5-1 shows the head and saturation values for matrix and fractures at the top left hand corner of the domain for each case. It is interesting to note that for this small change in fracture saturation in unit TCw1, we have an approximate doubling of the relative permeability. Since we know from the plot of vertical Darcy flux in the fracture and matrix (see Figure 5-16), that almost all of the flow occurs in the fractures in this region, this small change would be all that is required to move twice the amount of water through the unit (i.e. 2 mm/year).

**Table 5-1**  
**Head and saturation changes in Unit TCw1**

	Infiltration rate	
	1 mm/year	2 mm/year
Matrix head	1276.44	1291.56
Fracture head	1345.02	1345.77
Matrix saturation	0.9210	0.9381
Fracture saturation	0.0300	0.0355

## 5.5 Apparent Water Ages from $^{36}\text{Cl}$ Decay

None of the previous simulations have included the decay of  $^{36}\text{Cl}$ . The half-life of  $^{36}\text{Cl}$  was set at  $3.01 \times 10^5$  years and a long term simulation was carried out so that the steady-state plume could be examined. A constant, uniform infiltration rate of 2 mm/year was used to generate the steady-state flow field. A fixed  $^{36}\text{Cl}$  input concentration of 500 units was applied at the surface of the domain as a 3rd-type boundary condition.

Figure 5-26 is a plot of the steady-state  $^{36}\text{Cl}$  plume. The concentration in the matrix and fractures are essentially the same at steady-state.

The apparent age of the water in the domain is based on the relative concentration and decay constant of  $^{36}\text{Cl}$  using the equation:

$$AGE = \frac{-1}{\lambda} \ln(C / C_0) \quad (5-1)$$

where  $\lambda$  is the decay constant for  $^{36}\text{Cl}$ ,  $C$  is the calculated steady-state concentration in either the fractures or the matrix and  $C_0$  is the input concentration at the surface, in this case 500 units.

Figure 5-27 shows the apparent groundwater age based on steady-state  $^{36}\text{Cl}$  concentrations. These ages show that water in the fault zone would generally be much younger and that age would increase with lateral distance from the fault zone. Ages on the order of 3,000 to 7,000 years for the Calico Hills formation are reported in Wu, Chen and Bodvarsson, 1996 (e.g. page 238-239) and would appear to be younger than those we see here, which are between 10,000 and 40,000 years in the fault zone region adjacent to the Calico Hills formations. However, we would expect these ages to decrease if large transients were carrying contaminant rapidly down the fractures in the fault zone, a mechanism which is not operating in this long term steady-state flow system.



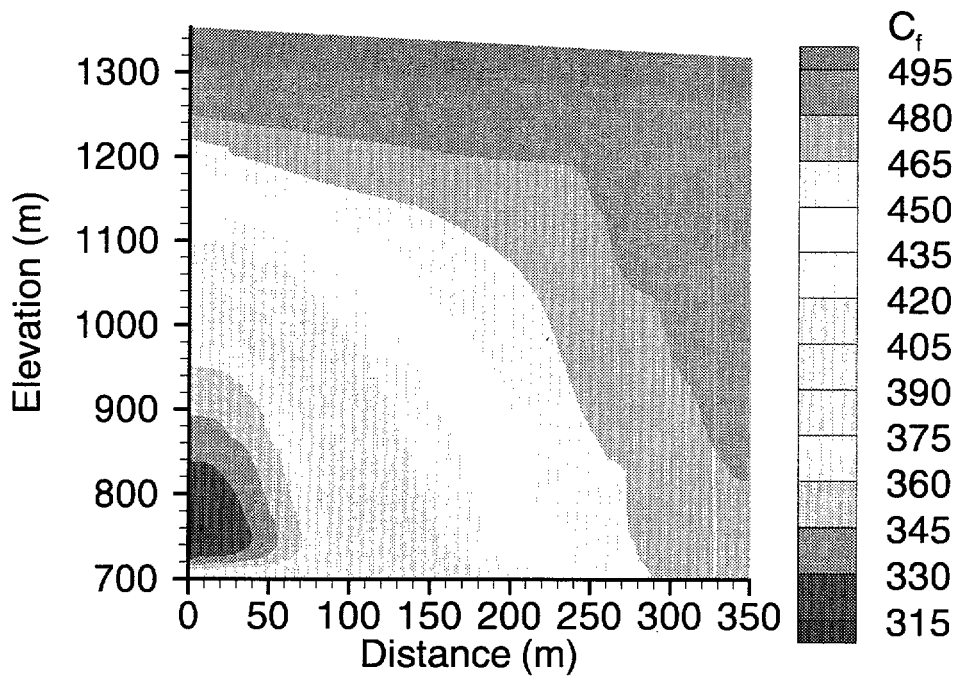
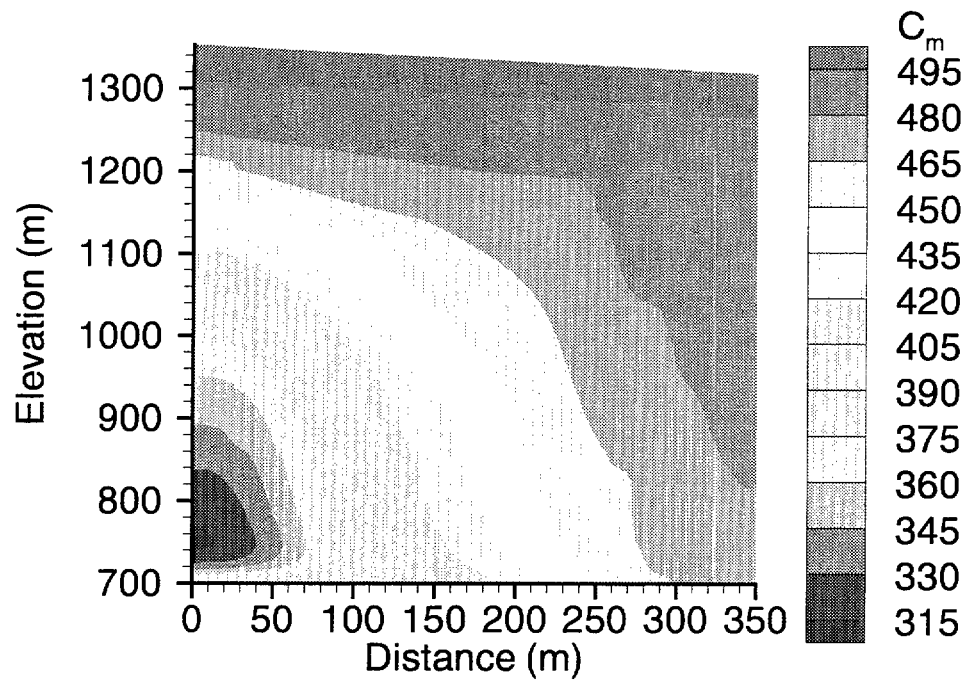
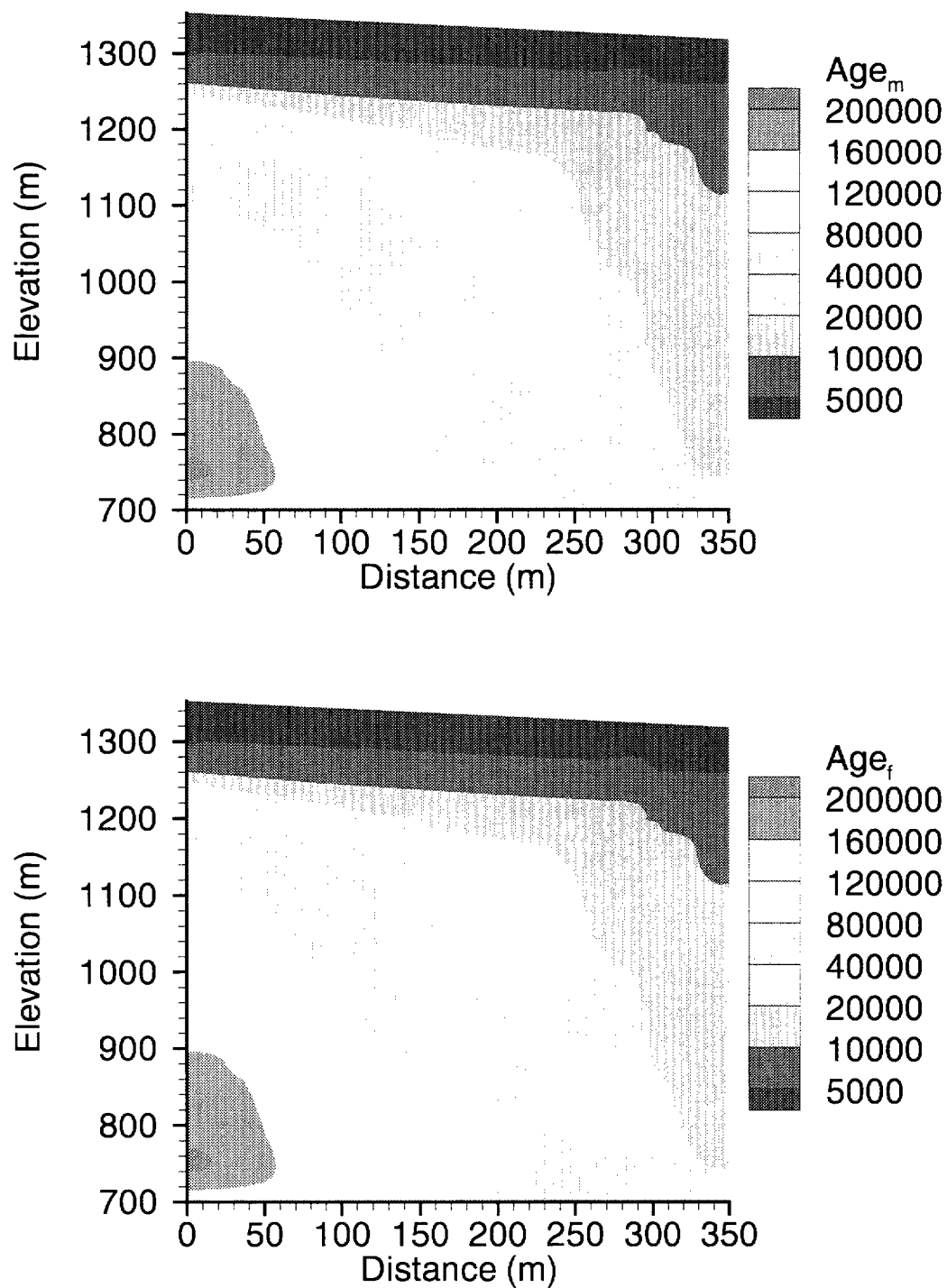


Figure 5-26  
 $^{36}\text{Cl}$  concentration at steady-state



**Figure 5-27**  
**Apparent age of groundwater based on <sup>36</sup>Cl concentration**

## 5.6 Results for Altered Fault Zone Properties

The objective of this simulation was to assess the effect that modifying the fault zone properties would have on the flow system and transport of  $^{36}\text{Cl}$ . The fault zone is no longer divided into three layers but has uniform properties from top to bottom. These properties are given in Table 2-2 as unit F2-all. The new fault zone has very different capillary pressure curves. Figure 5-28 shows the capillary pressure curves for fault zones TC and F2.

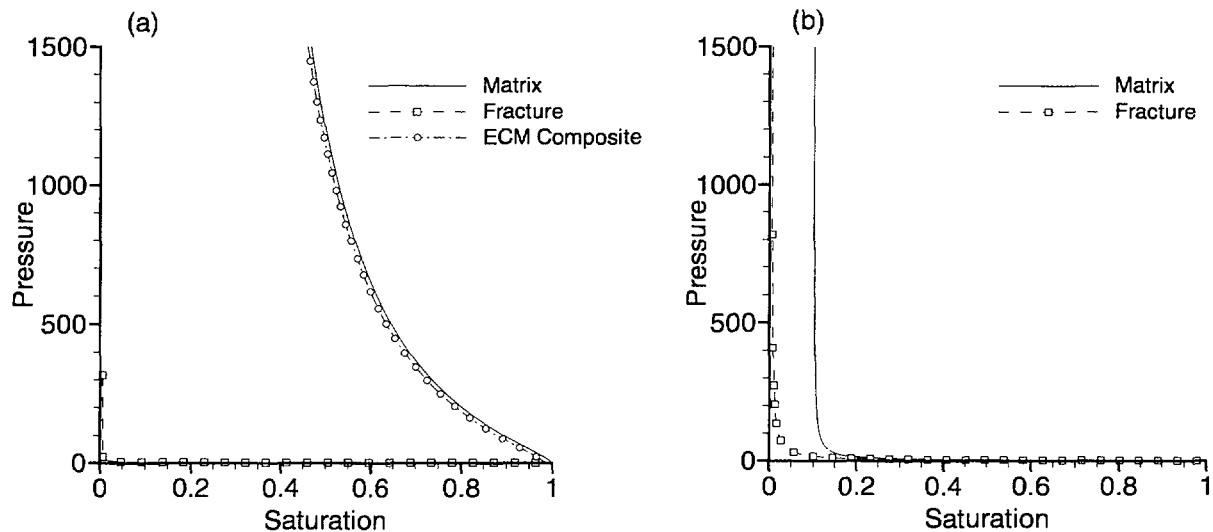


**Figure 5-28**  
Fault Zones (a) TC and (b) F2 capillary pressure curves

It can be seen that for unit F2, the matrix saturations drop off very rapidly as capillary pressures increase. The matrix permeability is also much higher than it was in the top and bottom fault zones, but similar to the value that was used previously for the middle layer (Paintbrush formation) in the fault zone. One other difference is that the permeability is now anisotropic.

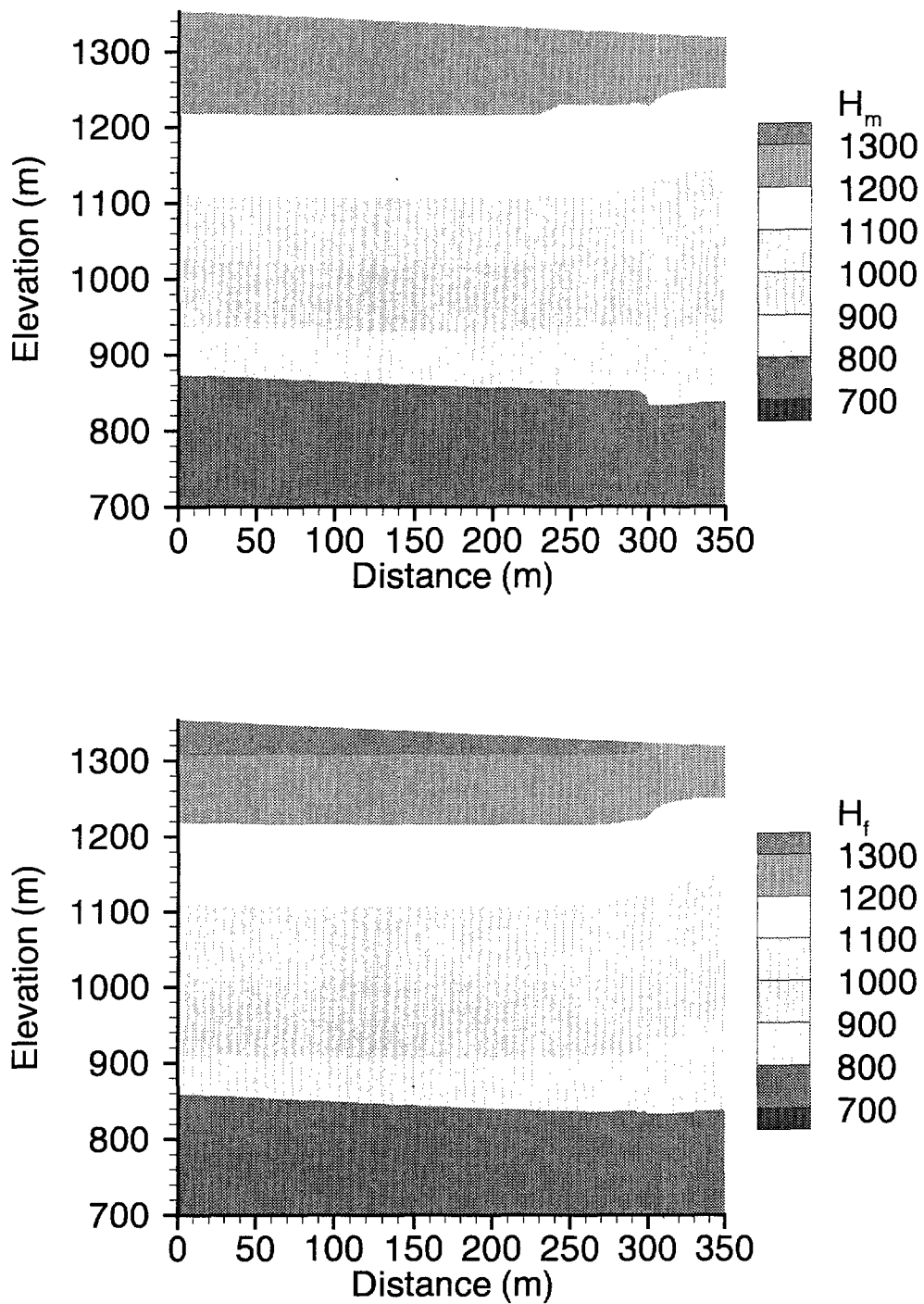
A constant, spatially-uniform infiltration rate of 2 mm/year yielded the steady-state heads shown in Figure 5-29, which are similar to previous results (e.g. see Figure 5-2).

Figure 5-30 shows the steady-state saturations. It is evident that the matrix saturations in the fault zone are now much lower than they were with the previous fault zone properties (see Figure 5-4).

Figure 5-31 is a plot of the steady-state  $^{36}\text{Cl}$  plume in the matrix. As for the previous set of fault zone properties, the concentrations (and apparent age) in the matrix and fractures are essentially the same at steady-state and so we have not shown both here. Compared to the results using the previous set of fault zone properties (see Figure 5-

26), here we see higher concentrations penetrating more deeply into the fault zone and less lateral penetration of the plume into the non-fault zone.

Figure 5-32 is a plot of apparent age of the matrix water, which shows that the tongue of younger water penetrates more deeply in the fault zone, while the maximum age of the waters in the non-fault zone are somewhat older than was previously observed (see Figure 5-27).



**Figure 5-29**  
**Heads at steady-state using F2 fault zone properties**

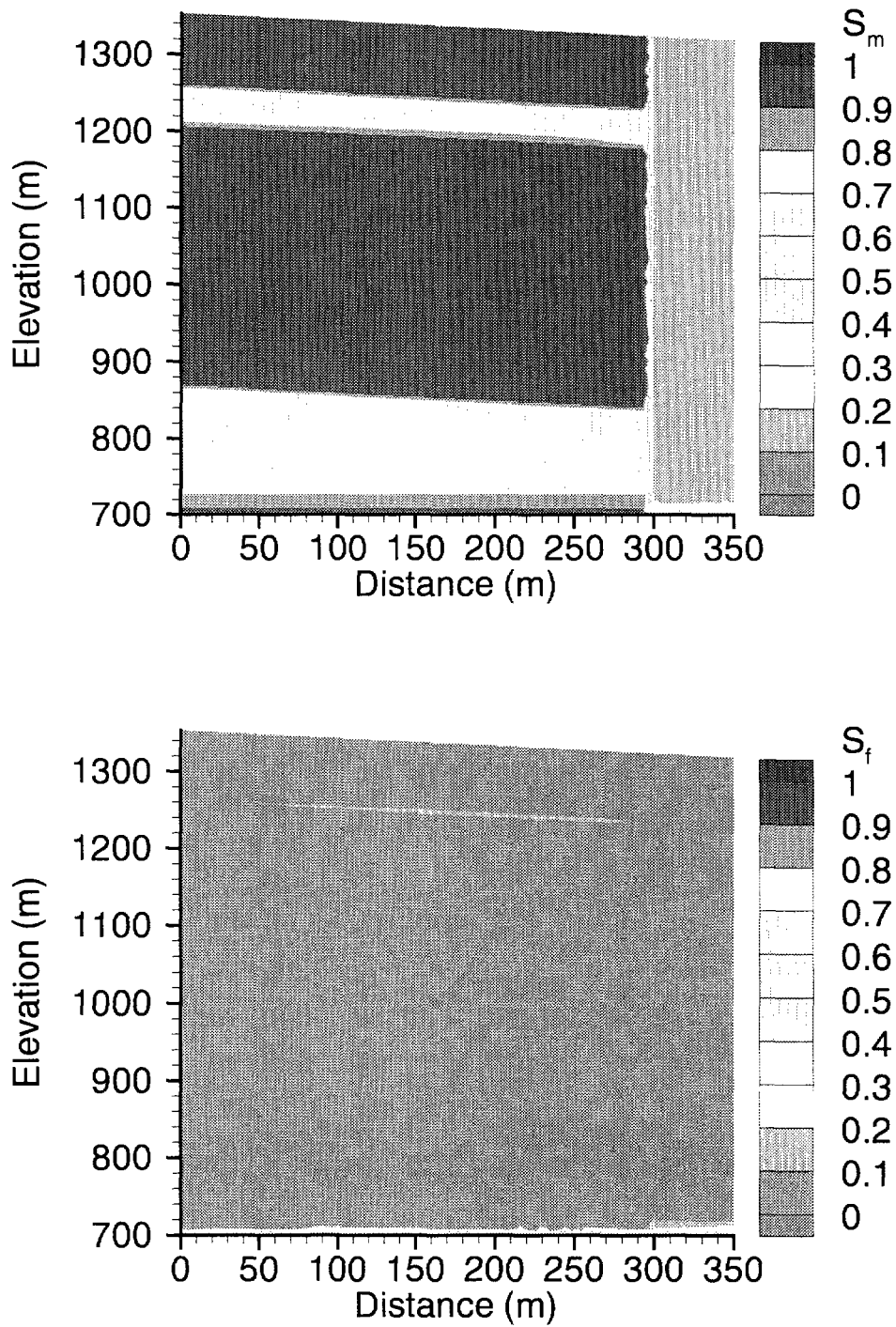


**Figure 5-30**  
**Saturations at steady-state using F2 fault zone properties**

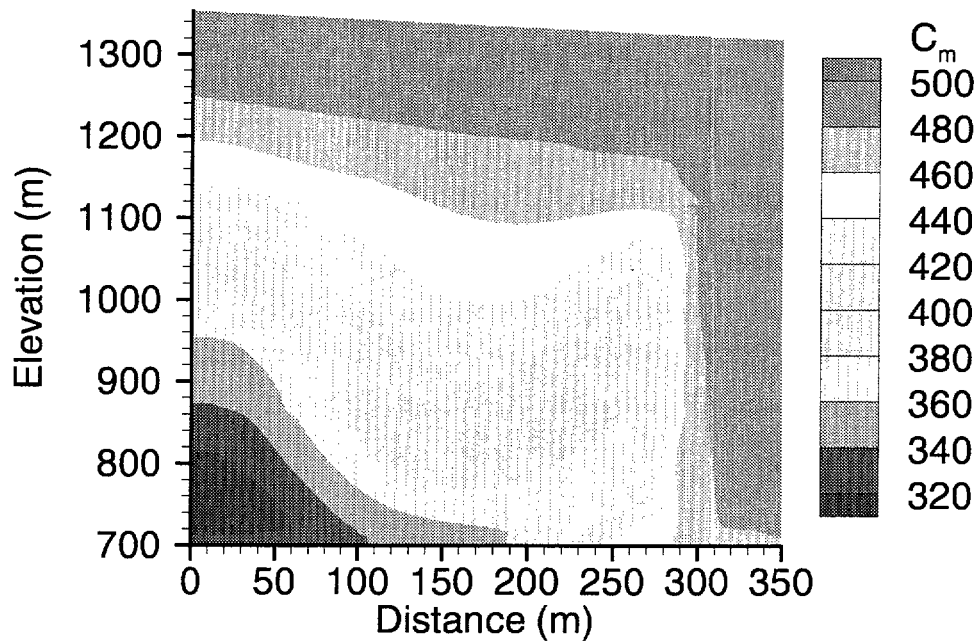


**Figure 5-31**  
Concentration in matrix at steady-state using F2 fault zone properties

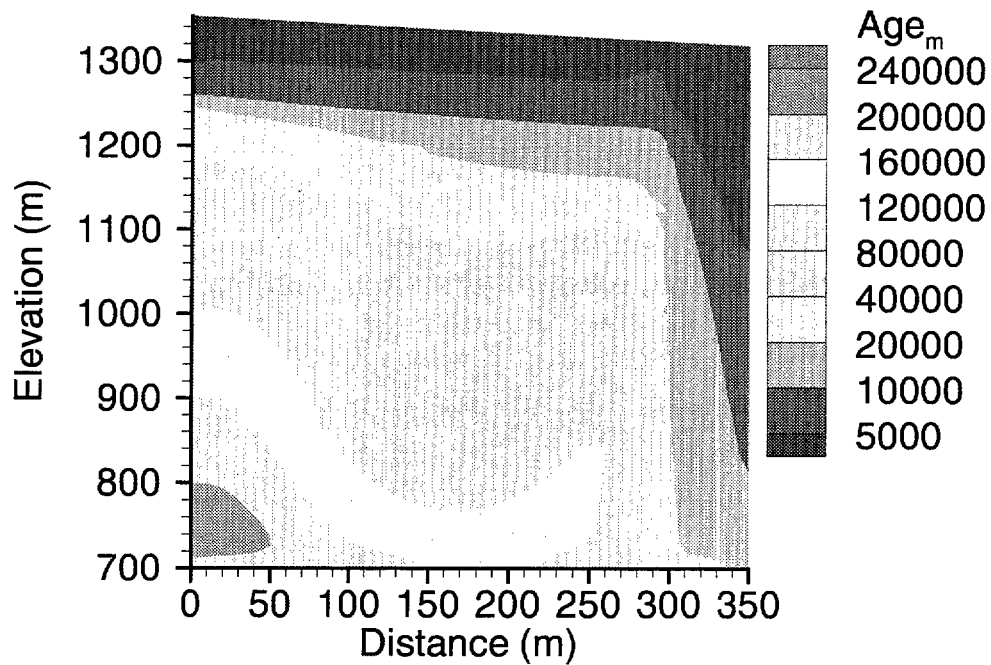


**Figure 5-32**  
Apparent age of matrix waters using F2 fault zone properties

### **5.6.1 Cases 8 & 9: Variable Recharge, 10 mm/week and 10 cm/week Infiltration Pulses with F2 Fault Zone Properties**

In order to determine whether fast fracture flow would occur when the F2 fault zone properties were used, simulations were carried out in which 10 mm/week and 10 cm/week infiltration pulses were applied every 10 years. These simulations were essentially the same as Cases 2 and 3 except that:

1. The steady-state distribution of  $^{36}\text{Cl}$  (shown in Figure 5-31 for the matrix) was used as the initial condition as opposed to a uniform initial concentration of 500.
2.  $^{36}\text{Cl}$  decay was included. Because of the relatively short duration of the simulations compared to the half-life of  $^{36}\text{Cl}$  we did not feel this would have a significant impact.
3. An infiltration rate of 2 mm/year was used to generate the steady-state flow field. If anything, this would result in higher matrix saturations than the 1 mm/year rate used previously, which in turn would favor the onset of fast fracture flow.

Vertical solute movement was much less than was observed previously and so we will only show the results for the 10 cm/week pulse case. Figure 5-33 shows the resultant plume at the end of the first 10 cm/week pulse. Because of the non-uniform initial condition, the difference between the initial concentration and the current concentration, labeled  $dC_m$  and  $dC_f$  on the plots, is shown here. A contour of 1 here would correspond roughly to our previous 501 contour, 50 to 550 etc. It is apparent that the plumes in the matrix and fractures are very similar, unlike what was observed previously (see Figure 5-8).

It appears that the mechanism of fast fracture flow in the fault zone is no longer active, since the plumes are not penetrating very far down into the fault zone, even under cases of high infiltration. This is probably due to the low fault zone matrix saturations, which arise from the new F2 fault zone properties, particularly the capillary pressure curve. The previous fault zone properties caused the matrix to be nearly fully saturated under conditions of long term infiltration. This appears to be a critical factor for initiating fast fracture flow.



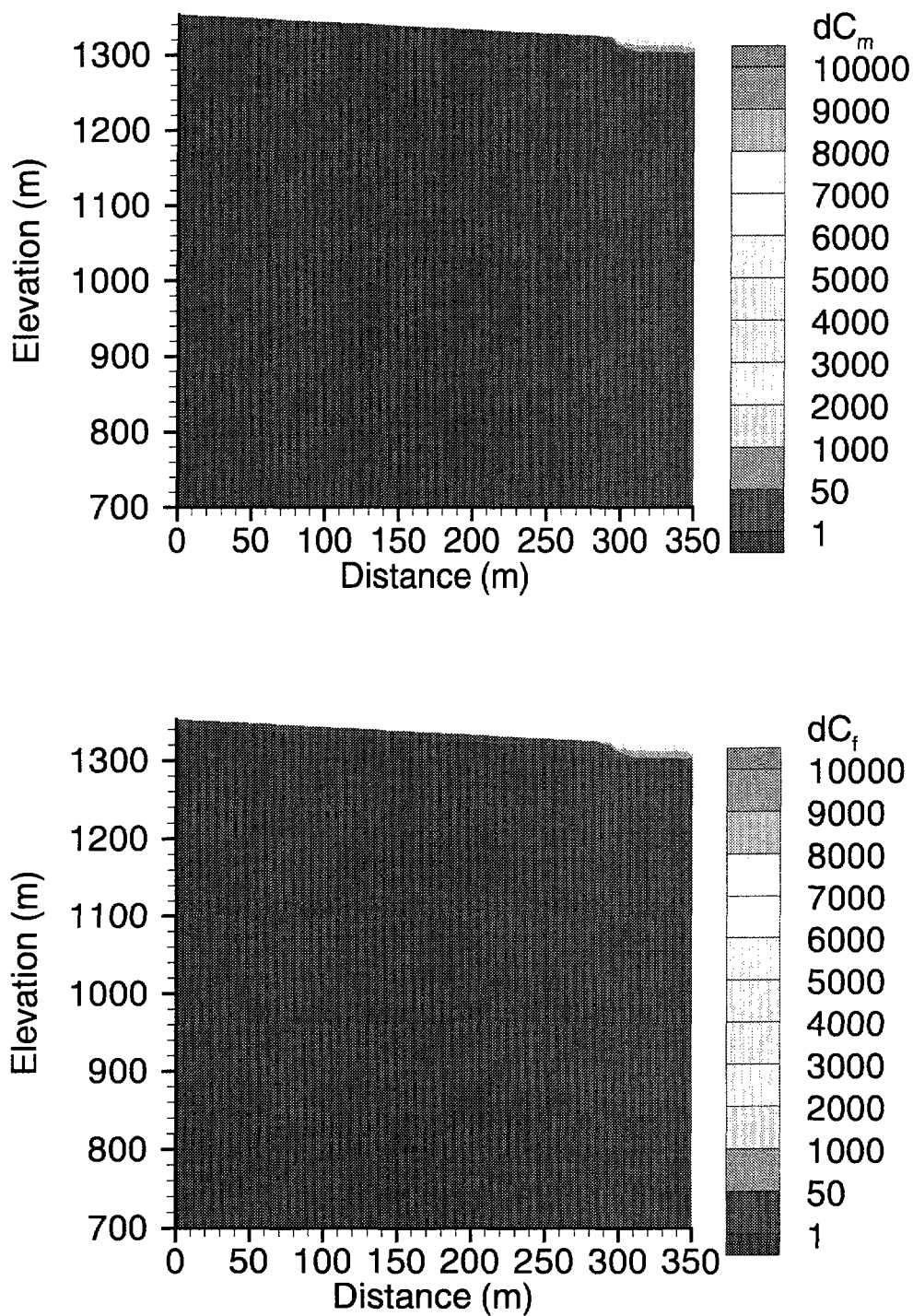


**Figure 5-33**  
Change in concentration after a 10 cm/week pulse, F2 Fault Zone Properties,  
Case 9.

## 5.7 Reduction of the Matrix/Fracture Coupling Term

Although the simulations with the altered Paintbrush fault zone formation properties exhibited fast fracture flow (see Figure 5-11), the solute plume was rapidly attenuated due to flow from the fractures into the matrix. Little movement of solute away from the fault zone was observed. The purpose of this simulation was to assess the effect of a 100-fold reduction in the value of the theoretical matrix-fracture coupling term (equation 3-12). This reduction applies equally to both the flow and advective-dispersive transport coupling terms. This reduction of fracture-matrix coupling from the theoretical values could be due to fracture coating resistance or film flow.

These simulations were essentially the same as Case 4 (which used the altered Paintbrush fault zone properties) except that:

1. the steady-state distribution of  $^{36}\text{Cl}$  was used as the initial condition as opposed to a uniform initial concentration of 500. It was re-generated using the altered Paintbrush fault zone properties but was very similar to that shown in Figure 5-26.
2.  $^{36}\text{Cl}$  decay was included. Because of the relatively short duration of the simulations compared to the half-life of  $^{36}\text{Cl}$  we did not feel this would have a significant impact.
3. An infiltration rate of 2 mm/year was used to generate the steady-state flow field. If anything, this would result in higher matrix saturations than the 1 mm/year rate used previously, which in turn would favor the onset of fast fracture flow.

The steady-state heads, saturations,  $^{36}\text{Cl}$  concentrations and apparent age of waters were not significantly different from previous results and will not be shown here. Figure 5-34 shows the resultant plume at the end of the first 10 cm/week pulse. Compared to the previous results (see Figure 5-11), the concentration in the fractures is much higher, while there is no visible plume in the matrix. This is to be expected since the matrix buffering effect has been greatly reduced because of the reduction in the matrix/fracture coupling term.

Figure 5-35 shows the plume at the end of 1 year. The slug of  $^{36}\text{Cl}$  from the first infiltration pulse has moved all the way down to the water table through the fractures in the fault zone and is leaving the model domain. Significant lateral movement of  $^{36}\text{Cl}$  into the non-fault zone occurred in the Topopah Springs formation and at the base of the model domain, in the Calico Hills formation. This latter effect may be related to proximity to the water table. There are also increased  $^{36}\text{Cl}$  levels in the Tiva Canyon formation, which were probably buffered before by flow into the matrix. There is a large plume of low concentration in the matrix which is more or less restricted to the fault zone.

Figure 5-36 shows the plume at 50 years, after 4 additional infiltration events and 10 years of equilibration. Concentrations in the fractures are actually less than were seen after one year of equilibration after the first pulse. Apparently, most of the solute mass has been flushed out of the system through the bottom boundary or been buffered by the matrix.

It is evident that the matrix/fracture coupling term exerts a strong influence on the fast fracture flow mechanism and reducing it can result in significant lateral movement of <sup>36</sup>Cl away from the fault zone.

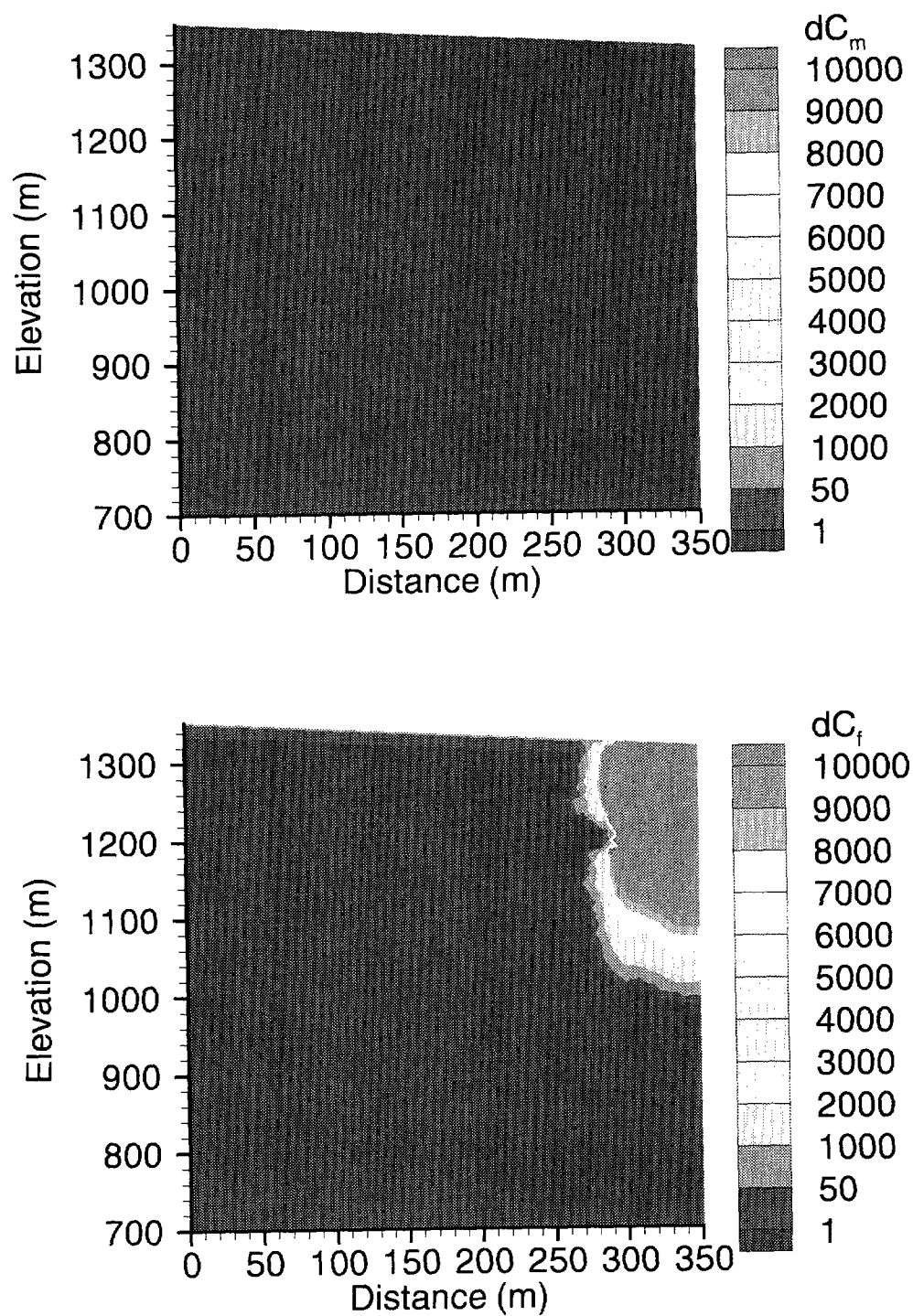


Figure 5-34  
Change in concentration after a 10 cm/week infiltration event, Case 10

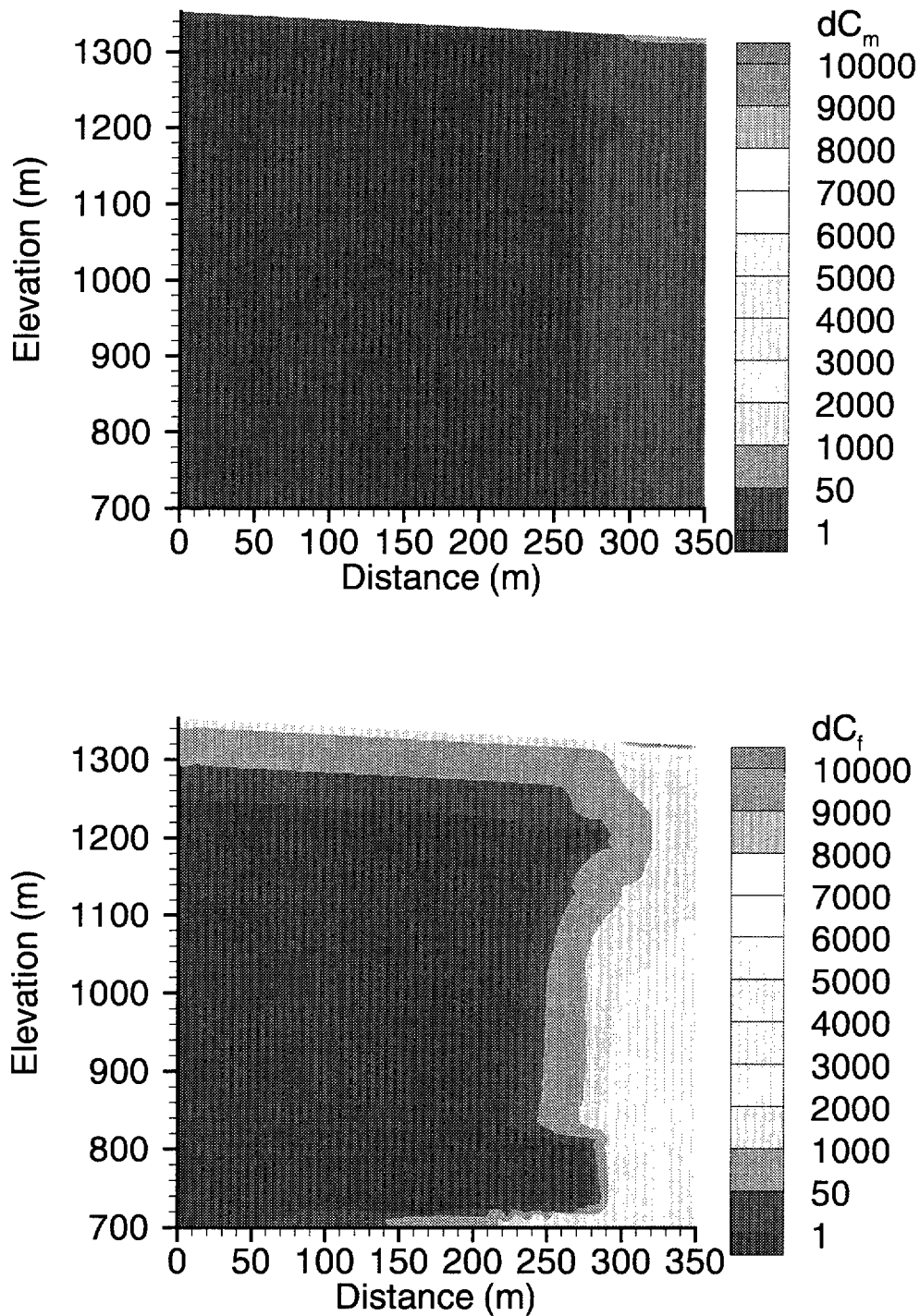


Figure 5-35  
Change in concentration after 1 year, Case 10

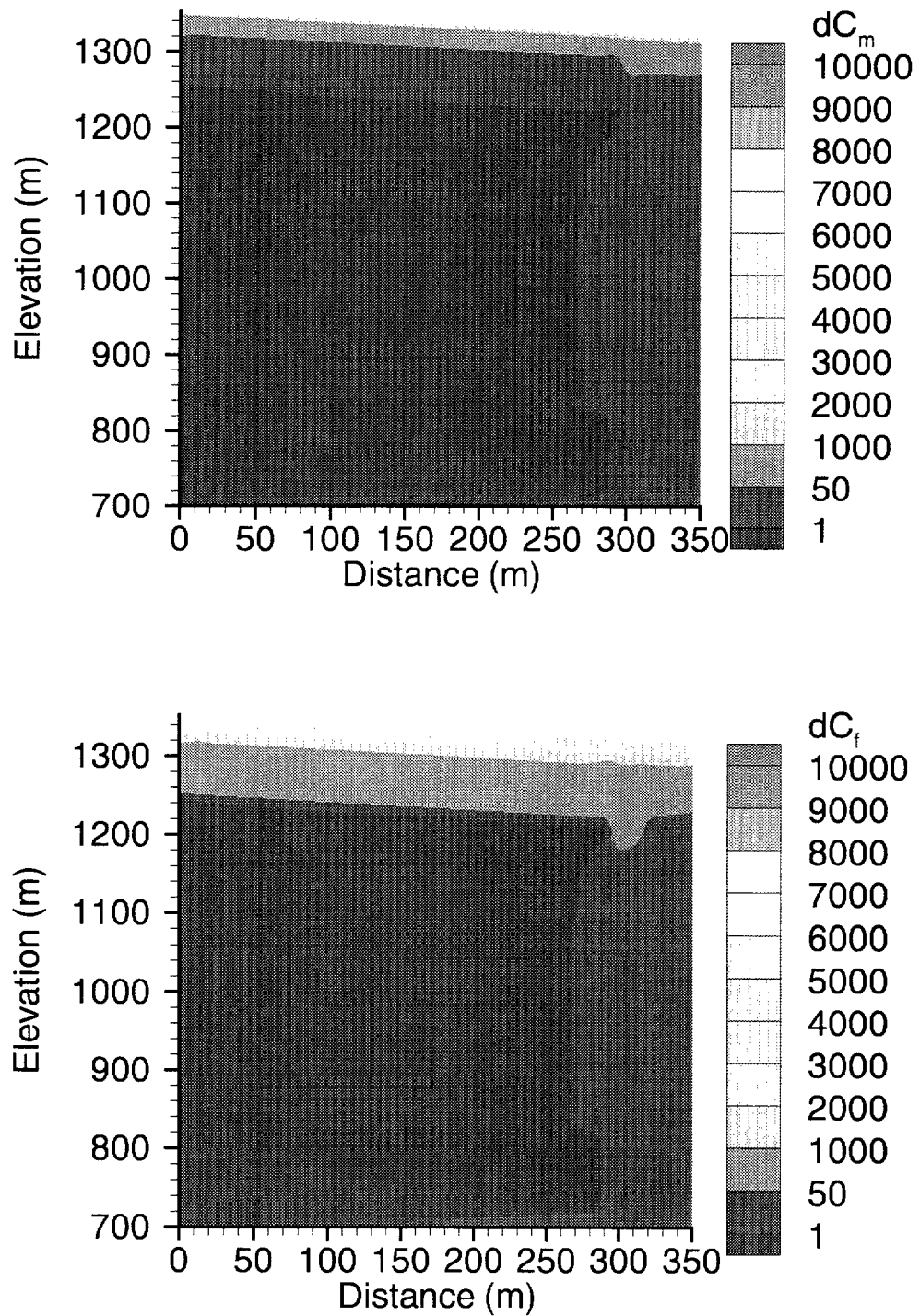


Figure 5-36  
Change in concentration after 50 years, Case 10

# 6

## **ADDITIONAL MODEL RESULTS USING AN AVERAGE RECHARGE RATE OF FIVE MILLIMETERS PER YEAR AS A BASE CASE**

---

In light of the results from the simulations conducted earlier in this project, and after consultation with various researchers involved in the Yucca Mountain project, it was determined that a final set of Phase 1 simulations should be carried out to reinforce the conclusions for higher average infiltration rates.

Consequently, additional scenarios were simulated with the following notable differences from previous runs:

1. The long term rate of recharge was increased to 5 mm/year, up from 1 or 2 mm/year in the earlier work. This appears to be consistent with more recent data.
2. Pulse events were either 10 mm/week or 10 cm/week for 1 week every 10 years as before, however, the pulse was applied over the entire 350 m of the top of the system. Previously, the pulse was applied to the 50 m wide fault zone at the right end of the top of the system. Applying the pulse events to the entire top of the system simulates the effect of a large episodic rainfall event, which then will be focused into the fault zone due to the spreading layer. This simulates, in an approximate way, the effects of runoff into the fault zone.

With these changes to infiltration, four scenarios were modeled. These were:

1. The Base Case, using the original data.
2. A case with the altered Paint Brush fault zone properties.
3. A case with original Paint Brush properties, but reduced fracture/matrix coupling factor.
4. A case with both altered Paint Brush fault zone properties and reduced fracture/matrix coupling factor.

These four cases will be used to demonstrate which effects are important in producing movement of the tracer away from the fault zone to the repository. The same finite element mesh shown in Figure 5-1 was used for the work described in this chapter.

As well, after consultation with EPRI, the flux diversion factors are computed differently than in previous runs. Note that the flux diversion is highly time-dependent in the case of pulsed infiltration. This will be described in some detail in the following sections.

A constant, long-term infiltration rate of 5 mm/year was applied on the top boundary of the domain. In order to distribute the infiltration evenly between the matrix and fractured continua, a thin infiltration spreading layer was added to the top of the system. The pressure head was fixed at 0 (equivalent to 700 m total or hydraulic head) along the bottom. Both sides of the domain were assumed to be no flow boundaries, which represent flow divides or symmetry boundaries. Results of the steady-state simulation are shown in Figure 6-1. It is clear from the contoured heads that the hydraulic potential in the fractures (Figure 6-1b) is somewhat higher than the matrix (Figure 6-1a) near the top of the system, which is probably because of focused recharge (due to the infiltration spreading layer). There are also zones of higher potential in the fractured continua near the base of the Topopah Spring formation (TSw) and to a lesser extent near the base of the Tiva Canyon formation (TCw) in the non-fault zone. These could be caused by a buildup of water in the fractures prior to penetrating the lower layers.

The matrix saturations (Figure 6-1c) are very high (0.9 or greater) throughout most of the cross-section, with the exception of the Paintbrush (PTn) and Calico Hills Formations (CHn), which are both non-welded tuffs. On the other hand, fracture saturations (Figure 6-1d) are near residual throughout most of the cross-section. Note that the PTn layer acts as a barrier to flow, and causes significant diversion of infiltration into the fault zone.

The model was set up to simulate transport using these steady-state flow conditions as input. Initial background concentrations (expressed as the ratio of  $^{36}\text{Cl}/^{35}\text{Cl}$ ) were generated by assigning a third-type boundary condition along the top of the domain with an input concentration of 500 and assuming decay of  $^{36}\text{Cl}$  (301,000 year half-life). The resultant steady-state plume for the matrix is shown in Figure 6-1e. Also shown in Figure 6-1f is the apparent age of the matrix waters which can be calculated from the relative concentration and decay constant of  $^{36}\text{Cl}$  using the equation (5-1).

These ages show that water in the fault zone would generally be much younger and that age would increase with lateral distance from the fault zone. Ages on the order of 3,000 to 7,000 years for the Calico Hills formation are reported in Wu, Chen and Bodvarsson (1996, e.g. page 238-239) which are within the range calculated here.



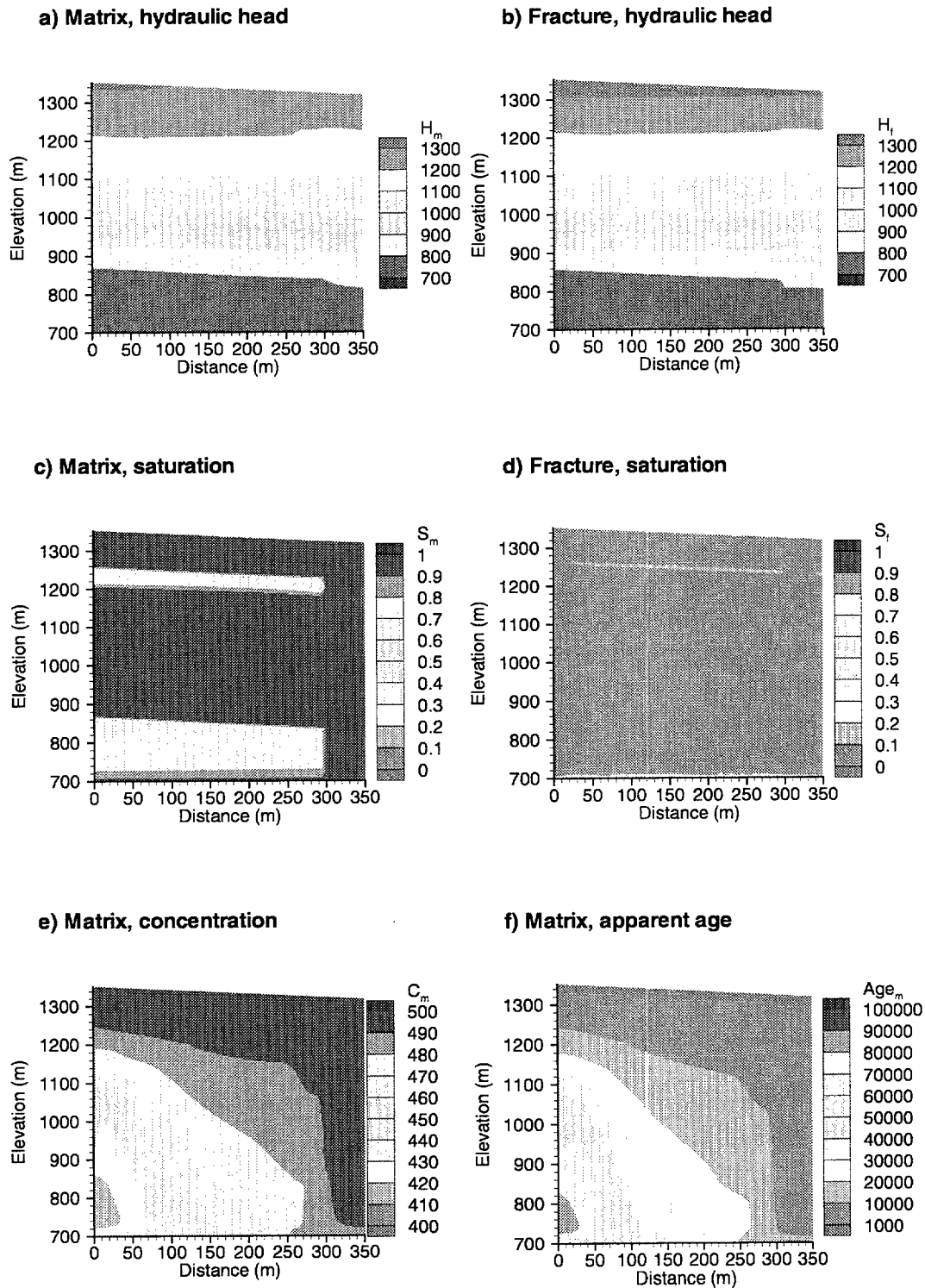


**Figure 6-1**  
**Steady State System**

## **6.1 Base Case**

Using the concentrations shown in Figure 6-1e as our initial background, a third-type boundary condition was applied along the top of the domain with an input concentration of 20,000, which is representative of levels attained during bomb testing. The resultant plume (expressed as the change in concentration from the initial condition) is shown at a time of 50 years for the matrix and fractures in Figures 6-2a and 6-2b respectively, and has not penetrated very far into the system in either case. The concentrations in the matrix and fractures are essentially the same, indicating that the system is in equilibrium.

Clearly, this base case simulation with a constant infiltration rate can't explain the observed rapid movement of  $^{36}\text{Cl}$ . However, it is possible that episodic infiltration events may take place at the Yucca Mountain site. It is conjectured that very large amounts of infiltration may occur during short periods of time. This large infiltration may be due to an episodic rainfall event, followed by focusing caused by preferential runoff.

Figures 6-2c and 6-2d show the effect of applying an infiltration pulse of 10 mm/week for 1 week every 10 years after 50 years. In this case the plume has advanced further into the system but has not penetrated the Paintbrush formation. The effect of even larger infiltration pulses of 10 cm/week are shown in Figures 6-2e and f. In this case the plume has penetrated the Paintbrush formation in the region of the fault zone but not at very high concentrations. There is a small region of elevated concentration in both matrix and fractures which could be due to the pooling of water above the Paintbrush formation in the fault zone.

Figure 6-3 shows the evolution of the  $^{36}\text{Cl}$  plume with time for the base case with 10 cm/week pulses. Immediately following the first pulse event, concentrations in the fractures are quite high (Figure 6-3b). However, after 1 year the matrix and fractures have equilibrated and the concentrations are much lower (Figures 6-3c and d). Because the matrix porosity is high relative to the fracture porosity, it buffers the concentration so the peaks are much lower than we observed in the fractures at the end of the first pulse.

## **6.2 Altered Paintbrush Properties**

Examination of saturations and Darcy fluxes indicated that the properties assigned to the Paintbrush formation in the fault zone (F1-P) were inhibiting the movement of  $^{36}\text{Cl}$  by causing water to flow through the matrix rather than the fractures. The large storage capacity of the matrix was in effect absorbing the solute. In order to study this effect further, it was decided to assign the properties of layer F1-TS to F1-P in Table 2-2 in order to see if this would enhance the downward movement of  $^{36}\text{Cl}$ .

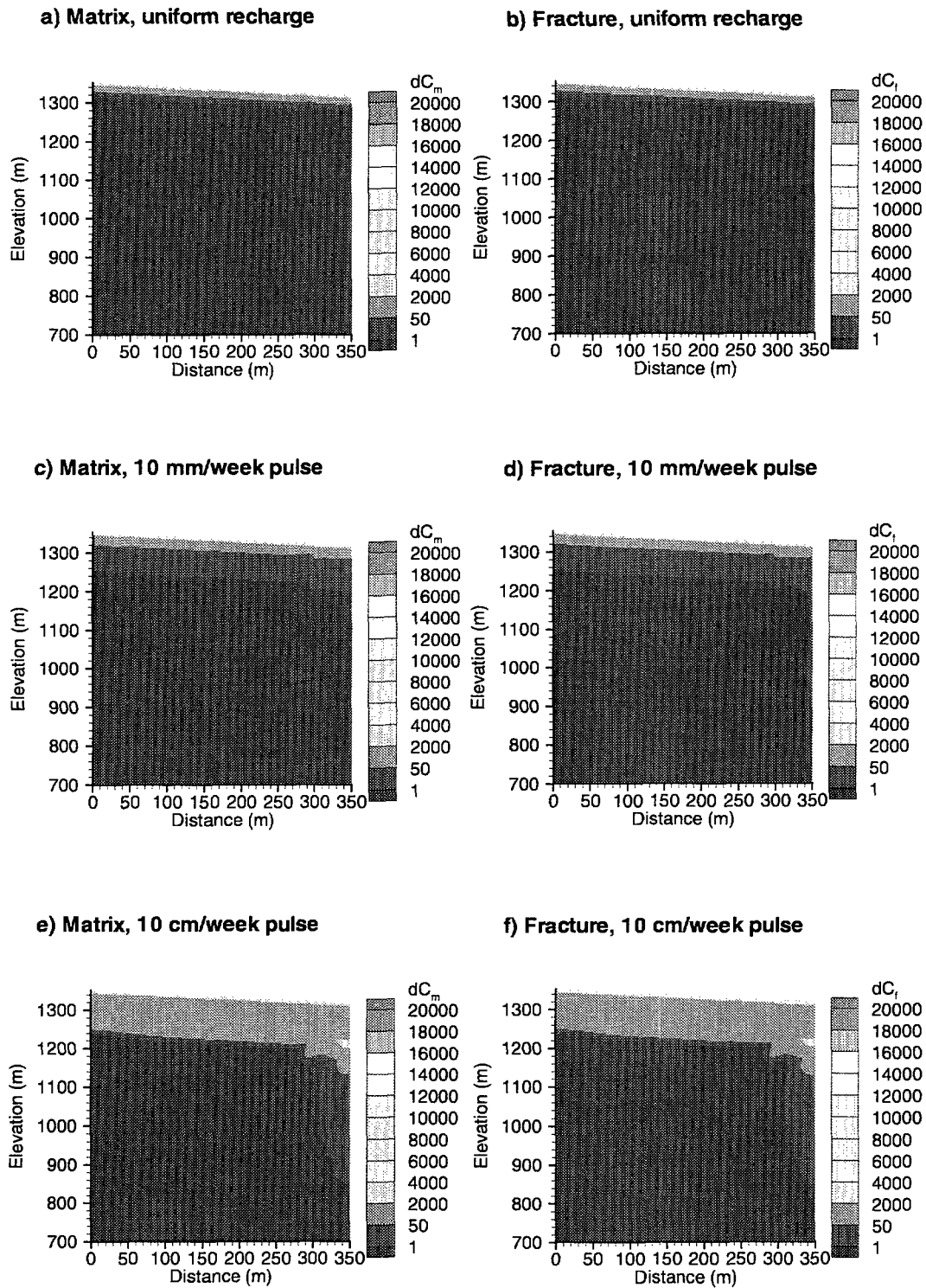
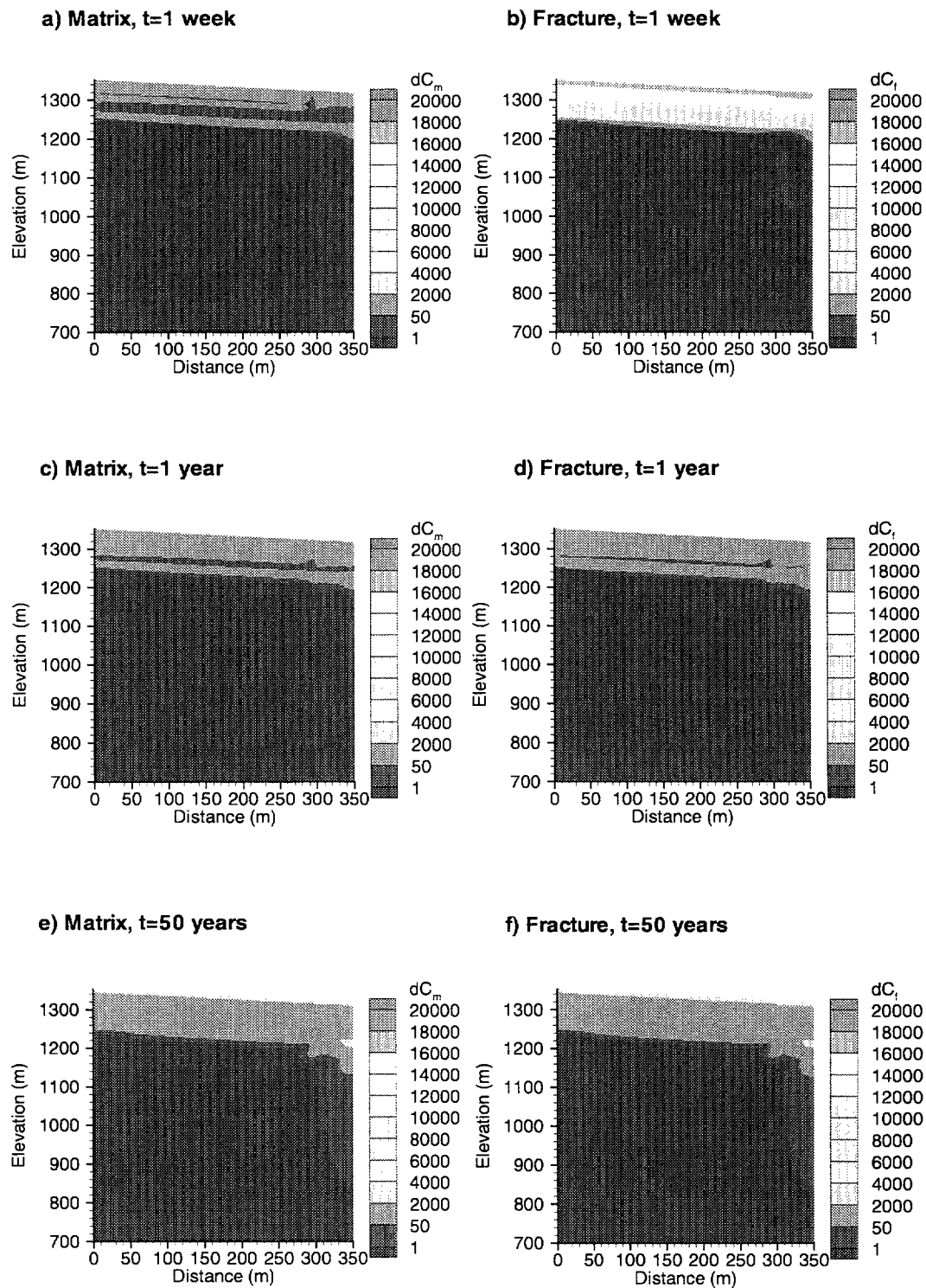


Figure 6-2  
Base Case Concentration, t=50 years



**Figure 6-3**  
Base Case Concentrations with 10 cm/week Pulse Events

The results of this simulation are shown in Figure 6-4 for the uniform recharge and increased pulse event cases. In this case, the plume has advanced further, concentrations are higher and there is no evidence of pooling above fault zone F1-P when compared to the base case. Plumes in the matrix and fractures are very similar indicating that the two continua have equilibrated since the last pulse .

### **6.3 Reduction of the Matrix/Fracture Coupling Term**

Although the simulations with the altered Paintbrush fault zone formation properties exhibited fast fracture flow, the solute plume was rapidly attenuated due to flow from the fractures into the matrix, and little movement of solute away from the fault zone was observed. The purpose of this simulation was to assess the effect of a 100-fold reduction in the value of the theoretical matrix-fracture coupling term but with the original F1-P properties. This reduction applies equally to both the flow and advective-dispersive transport coupling terms. Recall that equation (3-12) was based on a simple geometric model for matrix fracture coupling. A reduction of this coupling due to the effects of fracture coating resistance or thin film flow is a distinct possibility.

The results of this scenario are shown in Figure 6-5 for the uniform recharge and increased pulse event cases. The plume has penetrated the fault zone F1-P for even the uniform recharge case and for the 10 cm/week pulse case, the plume has advanced all the way to the bottom of the system at fairly high concentration and has even begun pooling and spreading laterally along the water table. There is ample evidence of pooling above fault zone F1-P, similar to that seen in Figures 6-2e and f for the base case. Plumes in the matrix and fractures are visibly different which indicates that the two continua have not equilibrated since the last pulse at 40 years, due to the reduction in the matrix/fracture coupling term.

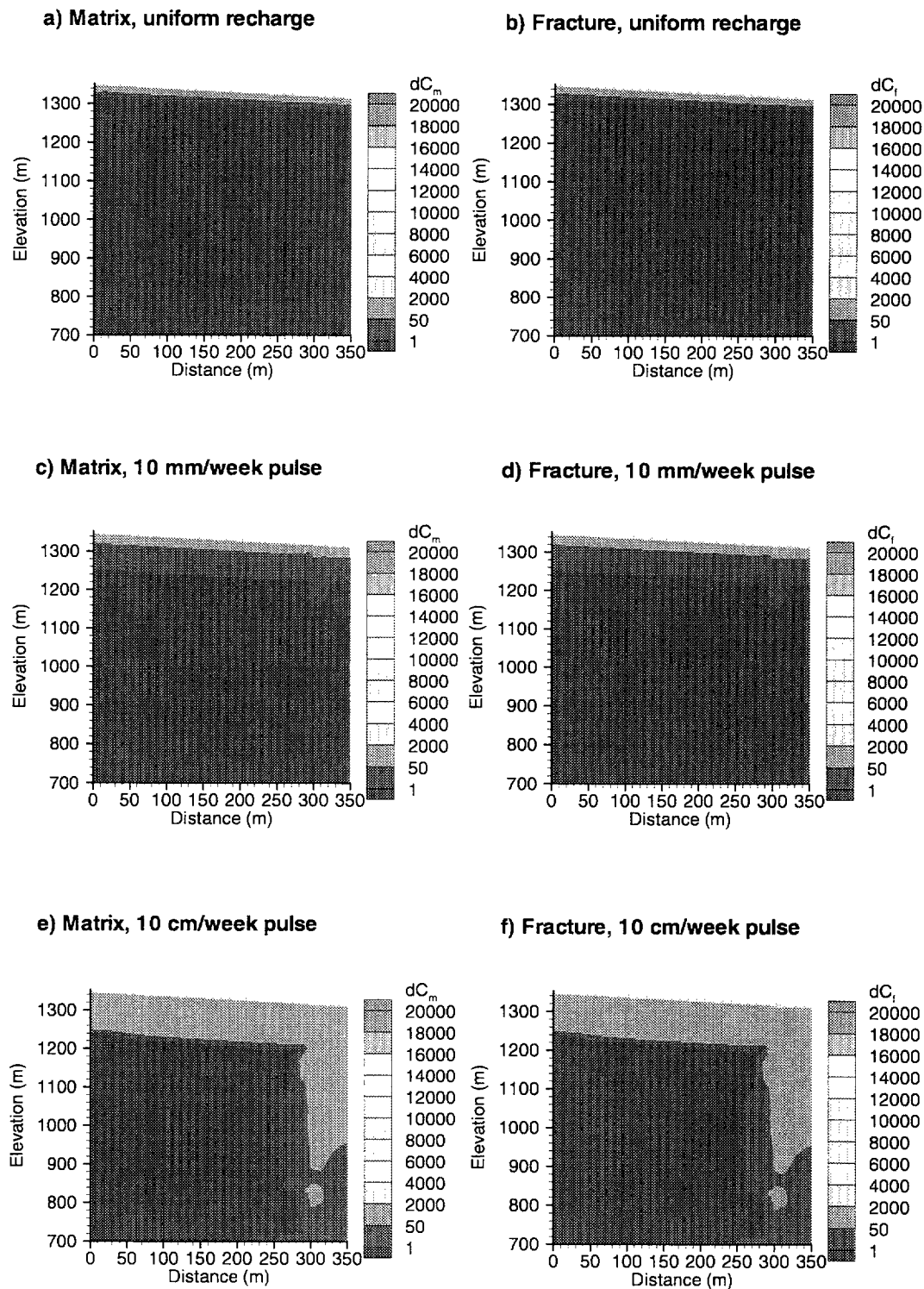


**Figure 6-4**  
Altered Paintbrush Properties Concentrations, t=50 years

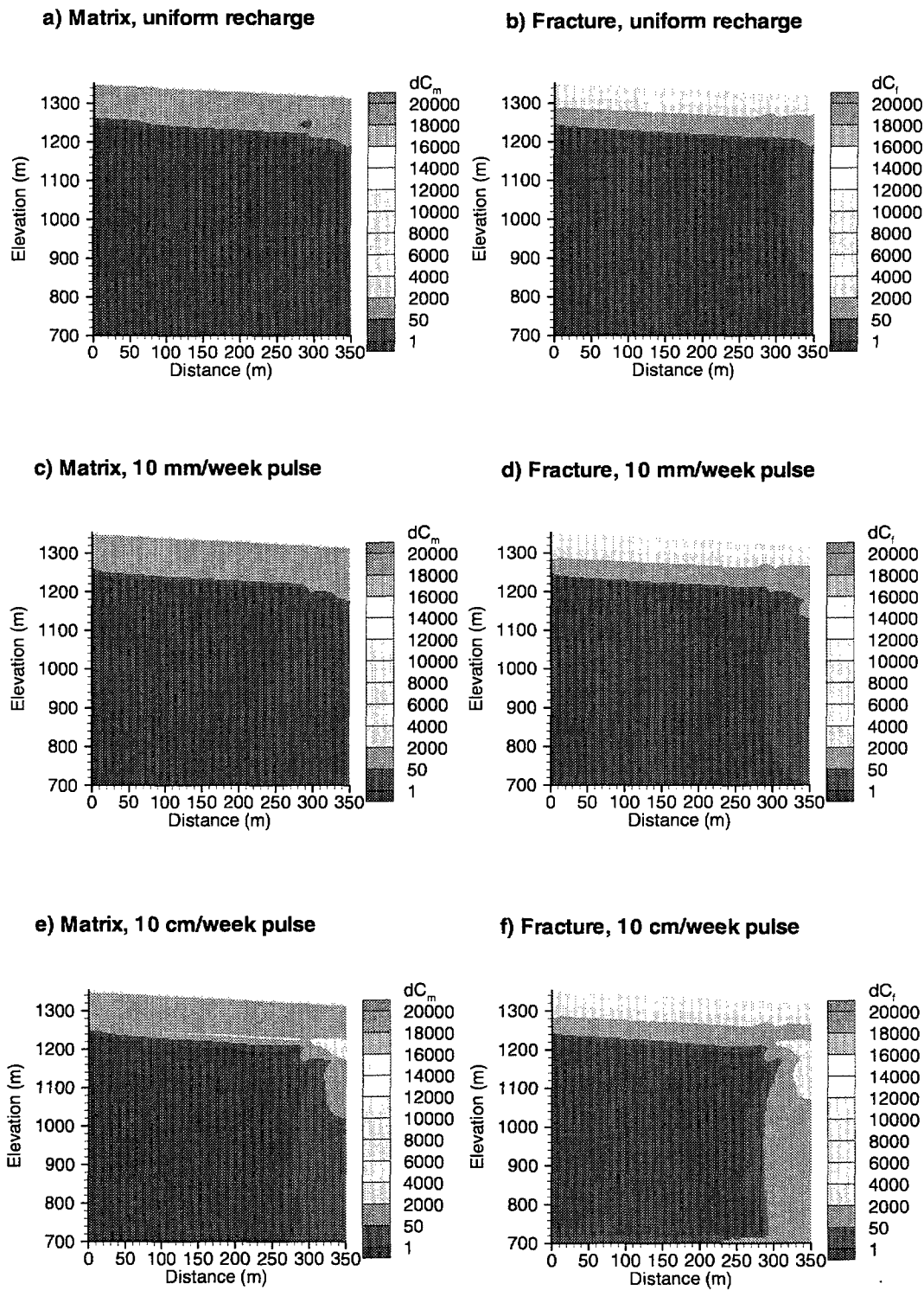


**Figure 6-5**  
Fracture/Matrix Reduction Concentrations,  $t=50$  years

## **6.4 Combined Case**

Figure 6-6 shows the coupled effect of both altering the Paintbrush fault zone properties and reducing the matrix/fracture coupling term. Again, there is no evidence of pooling above zone F1-P. There is also more significant lateral movement of the plume next to the fault zone. Again, plumes in the matrix and fractures have not equilibrated since the last pulse at 40 years.

## **6.5 Flux Diversion**

One of the objectives of the modelling exercise was to determine how much infiltrating water was diverted laterally into the 50 meter wide fault zone by the Paintbrush Formation, which is thought act as a barrier to flow.

Figure 6-7a is a plot of the vertical component of the Darcy flux versus time, which has been integrated over the non-fault zone (i.e. from  $X=0$  to  $X=300$  m) at both the top of the system and at the repository level (assumed to be at elevation 1185 meters for the purpose of this exercise) for the case of a single 10 mm/week pulse followed by 10 years of re-equilibration. Figure 6-7b shows the instantaneous percent diversion calculated according to:

$$\text{Percent diversion} = 100 - \frac{Flux_{repository}}{Flux_{top}} \times 100 \quad (6-1)$$

At early time, under the influence of the 5 mm/year background infiltration rate, the percent diversion is 52.8%. This rises to a value of 99.5% from around 1 to 10 days as the pulse passes through the system. We can also integrate the area under the curves in Figure 6-7a to get the total flux in each case and use those values in (29) to calculate the average percent diversion. This yields a value of 63.0%.

Figure 6-8 shows the results for all 4 cases for a 10 cm/week pulse event. Figures 6-8b and d show that significant flows do occur in the repository region. In these instances a drop in percent diversion below the background value also occurs. This is due to the time lag between the passing of the pulse at the top and at the repository level due to system storage.

Table 6-1 shows the average percent diversion for each of the cases discussed previously. Altering the Paintbrush formation properties results in a reduction of average percent diversion, while reducing the fracture/matrix coupling term tends to increase diversion. In all cases, increasing the size of the infiltration pulse event increases the average diversion, up to a maximum value of 89.5% for the case of reduced fracture/matrix coupling and a 10 cm/week pulse event.



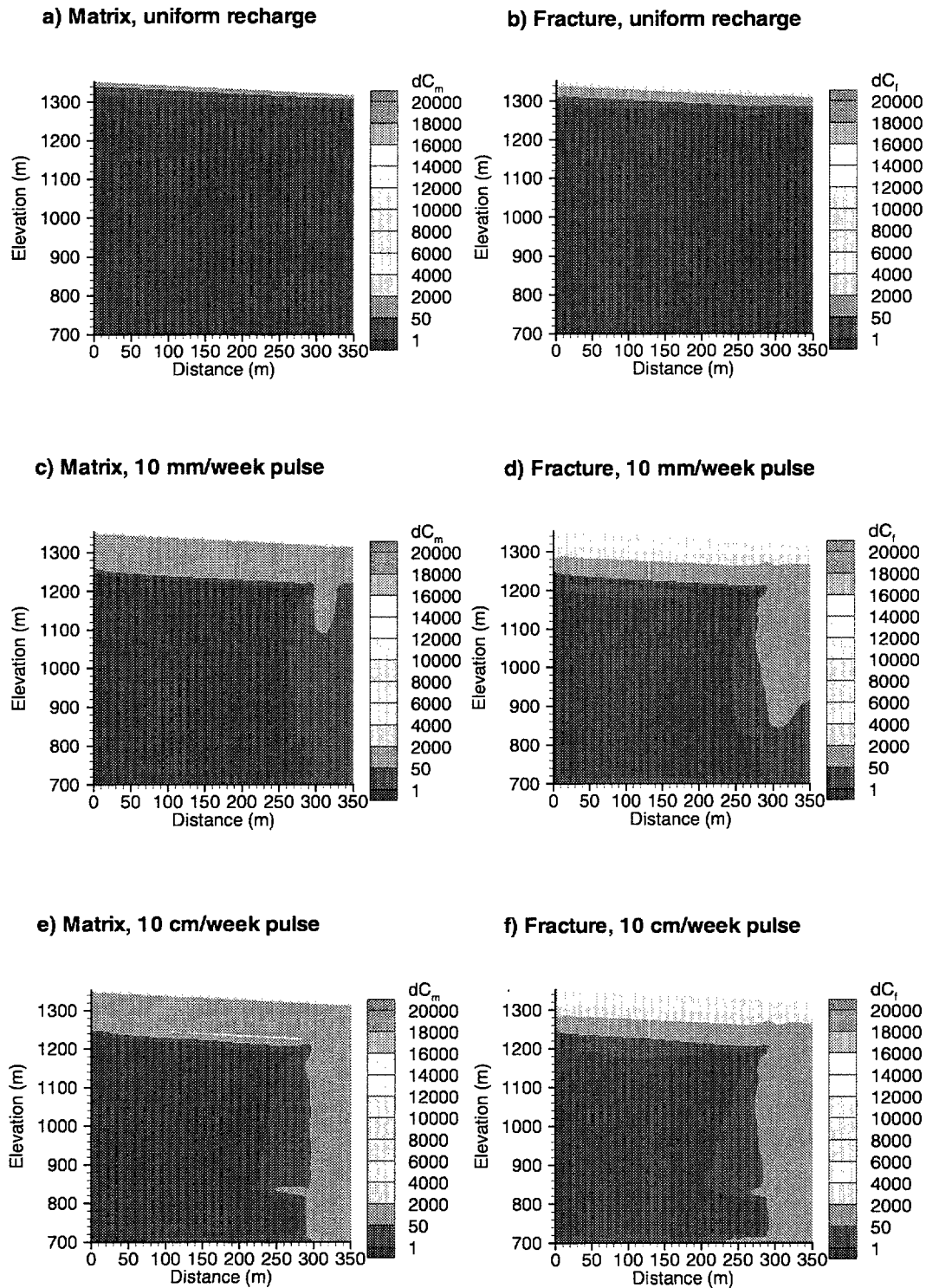


**Figure 6-6**  
Fracture/Matrix Reduction Concentrations,  $t=50$  years

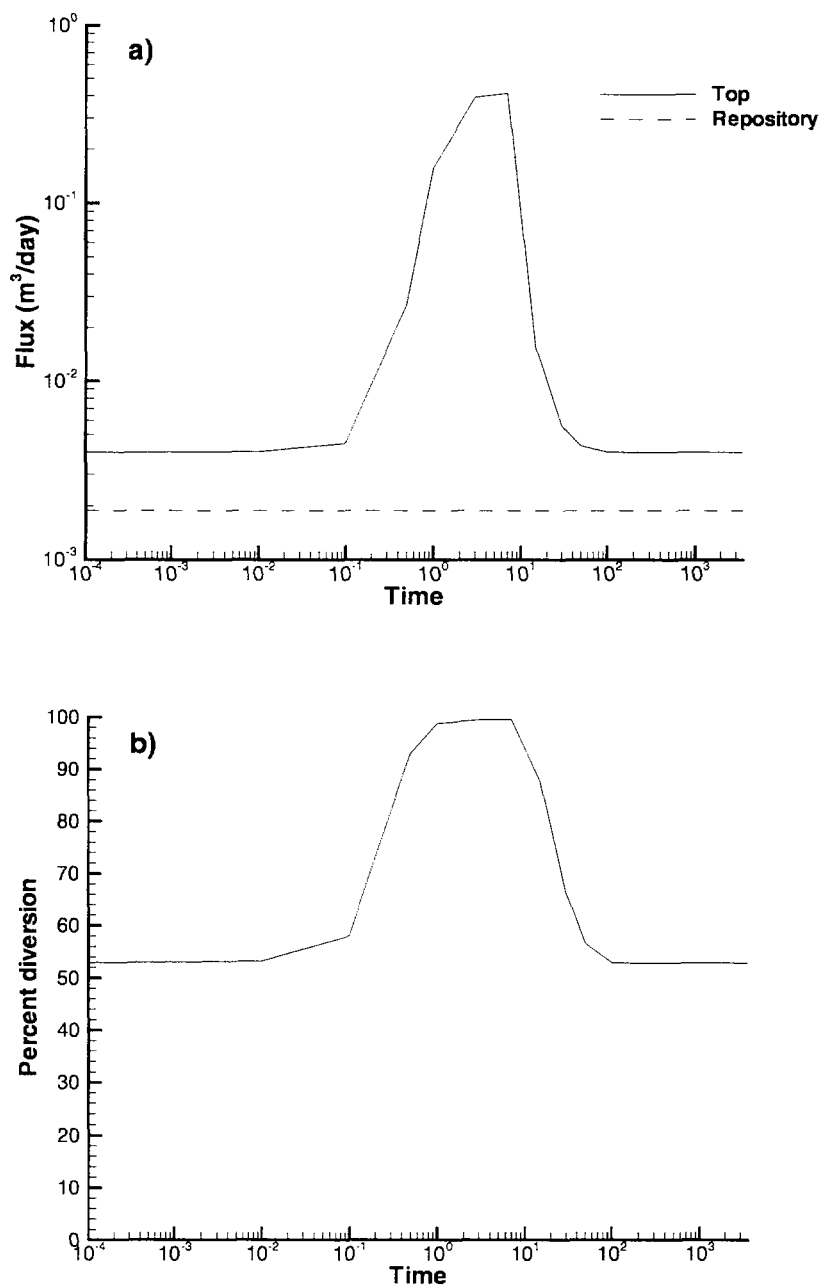
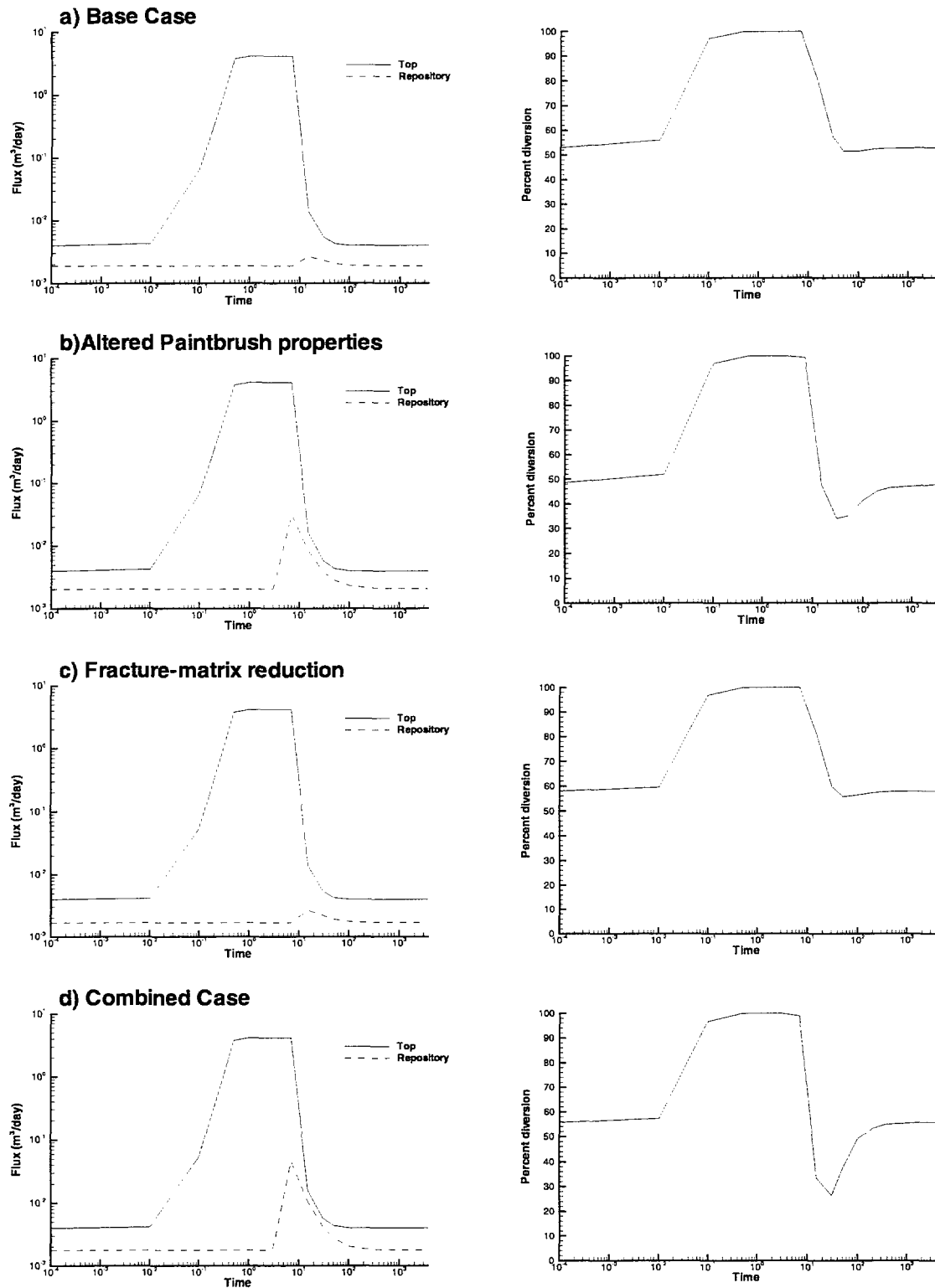


Figure 6-7  
Flux Diversion



**Figure 6-8**  
Flux Diversion for a 10 cm/week Pulse Event

**Table 6-1**  
**Summary of flux diversion calculation**

<b>Case</b>	<b>Average Percent Diversion</b>		
	<b>Background</b>	<b>10 mm/week pulse</b>	<b>10 cm/week pulse</b>
Base	52.8%	63.0%	88.2%
Altered Paintbrush formation properties	48.5%	59.4%	86.4%
Fracture/matrix coupling term reduction	65.4%	67.1%	89.5%
Combined	56.4%	64.9%	88.2%

# 7

## CONCLUSIONS

---

1. The capillary barrier (Paintbrush formation) diverts from 27 to 90% of the infiltrating water to the fault zone (depending on which recharge rates and material properties are used) as long as there are no discrete fractures or breaks in the barrier layer.
2. Fast fracture flow through the fault zone is highly dependent on the fault zone material properties and whether or not there are large episodic infiltration events.
3. In cases where fast fracture flow occurs, very little  $^{36}\text{Cl}$  penetrates laterally away from the fault zone unless the matrix-fracture coupling term is reduced dramatically from the theoretically calculated factor.
4. The matrix is near saturated even under low long-term infiltration. This is dependent on the properties in the fault zone (i.e. F2 fault zone properties inhibit fast fracture flow)
5. The ECM model cannot be used to simulate fast fracture flow.
6. It is necessary to obtain a true steady-state flow solution before attempting to do a transport solution. The non-linear equation must be solved to very small residuals which is exceedingly difficult.
7. Regions of the system which are not in close proximity to active fault zones may take an exceedingly long time to reach equilibrium with respect to changes in infiltration at the surface.

Simulating flow at Yucca Mountain using a DCM model is an extremely challenging task. Despite the fact that full Newton iteration was used to solve the non-linear discrete algebraic equations, and that a very small Newton iteration convergence tolerance was used, simulations of tracer contaminant transport resulted in incorrect maxima and minima. This problem was traced to a combination of very small fracture volumes and extremely non-linear constitutive laws. Simply using a small global Newton convergence tolerance (i.e.  $|\Delta S| \leq 10^{-10}$ ) was no panacea, since this frequently caused the simulation to abort due to excessive Newton iterations. A new Newton

iteration convergence tolerance was developed (different for each node) which ensured that the flow solution was converged before use in a transport simulation.

We have carried out an extensive set of simulations of a typical Yucca Mountain cross-section described in this work. We have presented representative results from these simulations. In all cases, very little fast fracture flow is observed unless large episodic infiltration events occur.

In addition, significant movement of the tracer through the fault zone only occurs if the fault zone F1-P formation properties are altered, or the matrix-fracture coupling term is reduced by two orders of magnitude. However, neither of these two effects alone results in movement of the tracer away from the fault zone. Combining both of these effects (altered F1-P properties and matrix-fracture coupling) causes significant movement of tracer away from the fault zone.

It would therefore appear to be necessary to further delineate mechanisms by which large episodic infiltration events occur, perhaps due to complex surface-water-groundwater interaction.

It is also imperative to further characterize the properties of fault zones at Yucca Mountain, and to obtain a more precise understanding of the mechanism of matrix-fracture coupling.

# 8

## REFERENCES

---

- Bodvarsson, G.S., and T.M. Bandurraga, 1996. Development and Calibration of the Three-Dimensional Site-Scale Unsaturated Zone Model of Yucca Mountain, Nevada: Lawrence Berkeley National Laboratory, LBNL-39315, 563 pp.
- Dean, R. and L. Lo, 1983. Simulation of Naturally Fractured Reservoirs, SPEJ, 23, pp. 695-707.
- Fabryka-Martin, J., A.V. Wolfsberg, P.R. Dixon, S. Levy, J. Musgrave, and H.J. Turin, 1996. Summary Report of Chlorine-36 Studies: Sampling, Analysis, and Simulation of Chlorine-36 in the Experimental Studies Facility: Los Alamos National Laboratory, Milestone Report 3783M, 131 pp.
- Forsyth, P.A., 1991. A control volume finite element approach for NAPL groundwater contamination, SIAM J. Sci. Stat. Comp., 12, pp. 1029-1057.
- Forsyth, P.A., Y.S. Wu and K. Pruess, 1995. Robust numerical techniques for saturated-unsaturated flow with dry initial conditions in heterogeneous media, Adv. Water Resources 18, pp. 25-38.
- Kessler et al. 1996. Kessler, J., R. McGuire, J. Vlasity, A. Long, S. Childs, B. Ross, F. Schwartz, D. Bullen, M. Apted, W. Zhou, E. Sudicky, G. Smith, K. Coppersmith, J. Kemeny, and M. Sheridan, *Yucca Mountain Total System Performance Assessment, Phase 3*, EPRI TR-107191, Electric Power Research Institute, Palo Alto CA, December 1996.
- Lax, P. and X.D. Liu, 1998, Solution of two-dimensional Riemann problems of gas dynamics by positive schemes", SIAM J. Sci Comp., 19, pp. 319-340
- Letniowski, F.W. and P.A. Forsyth, 1991. A control volume finite element method for three dimensional NAPL contamination problems, Int. J. Num. Meth. Fluids 13, pp. 955-970.
- Robinson, B.A., A.V. Wolfsburg, G.A. Zyvoloski, and C.W. Gable, 1995. An unsaturated Zone Flow and Transport Model of Yucca Mountain: Los Alamos National Laboratory, Milestone 3468, 177 pp.

- Unger, A., P.A. Forsyth and E. Sudicky, 1996. Variable weighting methods for multiphase, multicomponent flow, *Adv. Water Res*, 19, pp. 1-27.
- Sudicky, E.A. and J.E. VanderKwaak, 1996. A holistic approach to modeling hydrologic systems: Integrating models of stream, 2D overland flow and 3D variably-saturated subsurface flow and transport, *ModelCare'96*, Golden, CO, Sept. 25-27
- Witwer, C., G. Chen, G.S. Bodvarsson, M. Chornack, A. Flint, I. Flint, E. Kwicklis, and R. Spengler, 1995. Preliminary Development of the LBL/USGS Three-dimensional Site-Scale Model of Yucca Mountain, Nevada: Lawrence Berkeley Laboratory, LBL-37356/UC-814, 69 pp.
- Wu, Y.S., S. Finsterle and K. Pruess, 1996. Computer models and their development for the unsaturated zone model at Yucca Mountain, In: G.S. Bodvarsson and T.M. Bandurraga (Editors), *Development and Calibration of the Three-Dimensional Site-Scale Unsaturated Zone Model of Yucca Mountain*: Lawrence Berkeley National Laboratory Report LBNL-39315, pp. 131-168.
- Wu, Y.S., G. Chen and G.S. Bodvarsson, 1996. Perched water analysis, In: G.S. Bodvarsson and T.M. Bandurraga (Editors), *Development and Calibration of the Three-Dimensional Site-Scale Unsaturated Zone Model of Yucca Mountain*: Lawrence Berkeley National Laboratory Report LBNL-39315, pp. 232-270.
- Zvan, R., P. Forsyth and K. Vetzal, Winter 1998, Robust numerical methods for PDE models of Asian options, 1, *J. Comp. Fin.*, 39-78.



# A

## DERIVATION OF CONVERGENCE CONDITION FOR DISCRETE FLOW SOLUTION

In this Appendix, we derive the convergence condition (equation 3-16) for the discrete flow solution which ensures that the transport solution for  $C_i^{(N+1)}$  will not exhibit incorrect local maxima and minima.

For ease of exposition, we consider a simplified form of the transport equation 3-21. The following analysis can be carried out for the complete equation 3-21, but the algebra becomes more complex. The final result is valid for the complete transport equation. Consider a simplified form of equation 3-21, where we ignore dispersion/diffusion, decay, and adsorption. In this case, equation 3-21 becomes

$$\{[\theta S_w C]_i^{N+1} - [\theta S_w C]_i^N\} \frac{V_i}{\Delta t} = \sum_{j \in \eta_i} C_{(ij+1/2)}^{N+1} (\lambda_w)_{(ij+1/2)}^{N+1} \gamma_{ij} (\psi_j^{N+1} - \psi_i^{N+1}) + (q_w C_{ups})_i^{N+1} \quad (A-1)$$

If we use pure upstream weighting for  $C_{ij+1/2}$ , where

$$\begin{aligned} C_{ij+1/2} &= C_i \text{ if } \psi_j^{N+1} - \psi_i^{N+1} < 0 \\ &= C_j \text{ if } \psi_j^{N+1} - \psi_i^{N+1} > 0 \end{aligned} \quad (A-2)$$

then equation (A.1) can be written as

$$\begin{aligned} &C_i^{N+1} \left( \frac{V_i}{\Delta t} [\theta S_w]_i^{N+1} - \sum_{j \in \eta_i} \min(flow_{ij}, 0) - \min((q_w)_i^{N+1}, 0) \right) \\ &= C_i^N [\theta S_w]_i^N \frac{V_i}{\Delta t} + \sum_{j \in \eta_i} \max(flow_{ij}, 0) C_j^{N+1} + \max((q_w)_i^{N+1}, 0) C_{inflow} \end{aligned} \quad (A-3)$$

where

$$flow_{ij} = (\lambda_w)_{ij+1/2}^{N+1} \gamma_{ij} (\psi_j^{N+1} - \psi_i^{N+1}) \quad (A-4)$$

Of course the discrete flow equations 3-7 are only solved to finite precision. The definition of the residual equation 3-13 using equation A-4 we obtain;

$$\begin{aligned} & [\theta S_w]_i^{N+1} \frac{V_i}{\Delta t} - \sum_{j \in \eta_i} \min(flow_{ij}, 0) - \min((q_w)_i^{N+1}, 0) \\ & = r_i + [\theta S_w]_i^N \frac{V_i}{\Delta t} + \sum_{j \in \eta_i} \max(flow_{ij}, 0) + \max((q_w)_i^{N+1}, 0) \end{aligned} \quad (A-5)$$

From equations A-5 and A-3 we obtain

$$C_i^{N+1} = \frac{[\theta S_w]_i^N \frac{V_i}{\Delta t} C_i^N + \sum \max(flow_{ij}, 0) C_j^{N+1} + \max((q_w)_i^{N+1}, 0) C_{inflow}}{[\theta S_w]_i^N \frac{V_i}{\Delta t} + \sum \max(flow_{ij}, 0) + \max((q_w)_i^{N+1}, 0) + r_i} \quad (A-6)$$

Since all coefficients of  $C_j^{N+1}$ ,  $C_i^N$  and  $C_{inflow}$  in equation A-6 are non-negative, then

$$\alpha_i \min(C_i^N, C_j^{N+1}, C_{inflow}) \leq C_i^{N+1} \leq \alpha_i \max(C_i^N, C_j^{N+1}, C_{inflow}) \quad ; j \in \eta_i \quad (A-7)$$

Where

$$\begin{aligned} \alpha_i &= \frac{[\theta S_w]_i^N \frac{V_i}{\Delta t} + flow_i^{pos}}{[\theta S_w]_i^N \frac{V_i}{\Delta t} + flow_i^{pos} + r_i} \\ flow_i^{pos} &= \sum_{j \in \eta_i} \max(flow_{ij}, 0) + \max((q_w)_i^{N+1}, 0) \end{aligned} \quad (A-8)$$

Of course if  $r_i = 0$  then  $\alpha_i = 1$ , and hence no spurious local maxima and minima can appear in the discrete solution. Consequently, a suitable measure of error for convergence of the flow equations is

$$\begin{aligned} |1 - \alpha| &\leq \varepsilon \\ \varepsilon &> 0 \end{aligned} \quad (A-9)$$

which will guarantee that

$$(1 - \varepsilon) \min(C_i^N, C_j^{N+1}, C_{nflow}) \leq C_i^{N+1} \leq (1 + \varepsilon) \max(C_i^N, C_j^{N+1}, C_{inflow}) \quad j \in \eta_i \quad (\text{A-10})$$

In practice,  $C_{ij+1/2}^{N+1}$  determined using a flux limiter as described in Unger et al (1996). The above analysis can be repeated using the limiter for  $C_{ij+1/2}^{N+1}$ , and the same convergence condition is obtained. In this case, the discretization is said to be of positive type (Lax et al, 1998). Crank-Nicholson timeweighting can also be employed, but this puts a restriction on the timestep size in order to ensure that the discrete equations have the correct behavior (Zvan et al, 1998). Consequently, regardless of whether pure upstream weighting is used or a flux limiter for  $C_{ij+1/2}^{N+1}$ , the flow equations must be solved to the tolerance (equation A-9).

The usual method of determining convergence of the Newton iteration for the flow equations is to simply check the changes from one iteration and the next. If these changes are small, then the solution is considered to have converged. However, even if the changes in saturations are very small (i.e.  $10^{-6}$ ),  $\alpha_i$  may not be near unity. In the simulations of flow in fractured Tuff, we found this to occur in the fractures, when the saturation was very small, the volume of the fracture was very small, and there was a large throughput of water in the fracture. Due to the highly non-linear nature of the capillary pressure and relative permeability relations, very small errors in saturations and pressures caused the flow solution error to be large, as measured by equation A-9.

In practice, a value of  $\varepsilon = 10^{-3}$  in equation A-9 was sufficient to prevent the appearance of physically incorrect oscillations in the discrete transport equation A-1.

# APPENDIX B SUPPLEMENT

## Color Versions of Selected Figures on CD-ROM

Attached to the back cover of this report is a CD-ROM holding 31 full color versions of report pages with 32 figures that are best viewed in color. These pages are being distributed on this CD-ROM as a Portable Document Format (PDF) file (CLRPAGES.PDF).

### Getting Started

1. Locate your computer's CD-ROM drive and insert the CD-ROM disk.
2. Install Adobe Acrobat Reader 3.0 from CD-ROM (instructions in next section).
3. Run Adobe Acrobat Reader 3.0
4. Open the file MEFIRST.PDF on the CD-ROM.

With MEFIRST.PDF open you will see a list of figures that are available in color on this CD-ROM. Each of the figure captions on these 5 pages is hyperlinked to the figure in question.

Acrobat Reader has document navigation buttons in a toolbar. You may use the arrow buttons in this toolbar to go from page to page within the PDF file containing the figures. Or you can use the custom bottom placed in the upper right corner of each page to return to the List of Figures page.

### Adobe Acrobat Reader 3.01

Adobe Acrobat® Reader, a program developed by Adobe Systems Incorporated to view and print PDF files, is provided on this CD-ROM. The latest version is always available from Adobe via the internet:  
(<http://www.adobe.com/prodindex/acrobat/readstep.html>).

The following is a list of supported computer platforms for Adobe Acrobat Reader:

---

Macintosh	Windows	Sun™ Solaris®
SunOS™	IBM® AIX®	HP-UX
Silicon Graphics® IRIX™	Digital UNIX®	Linux
OS/2®	MS-DOS	

### System Requirements

CD-ROM drive, a 13 inch or larger color monitor.

#### Requirements for Windows

- 486 or later PC processor
- Windows 3.1 or later, Windows 95, or Windows NT® 3.51 or later
- 8MB of RAM (16MB for Windows NT)
- 10 MB of available hard-disk space

#### Requirements for Macintosh

- Macintosh with a 68020 processor or Power Macintosh® later processor
- Apple System Software version 7.0 or later
- 8 MB of RAM
- 10 MB of available hard-disk space

### Installation Instructions

#### for Windows 3.1:

From the windows environment choose Run in the File menu of then Program Manager. When the Run dialog box appears press the Browse button. Choose the drive letter corresponding to your CD-ROM drive. Double click the "ACROREAD" directory, the "WIN" directory, and then the directory "16BIT", where you will find the file INSTALL.EXE. Now choose INSTALL EXE and press the OK button. You will press OK when the Run dialog box reappears. Follow the instructions given by the installation program.

#### for Windows 95 and NT:

From windows environment use Windows Explorer to locate the CD-ROM drive. Open the drive by double clicking it and find the folder "Acroread". Double click on the "Acroread" folder, the "Win" folder, and then the folder "32Bit" where you will find the file INSTALL.EXE. Now launch the installation program INSTALL.EXE by double

clicking on it. Follow the instructions given by the installation program.

***for Macintosh:***

From the Finder locate and double click the CD-ROM icon named " TR108536" on your desktop. Double click on the "Acroread" folder, the MAC folder, and then the folder READER where you will find the file INSTALL. Now launch this program by double clicking it. Follow the instructions given by the installation program.

**NING**

NG THIS  
SIGNIFIES  
TANCE OF THE  
EMENT TERMS  
D HEREIN


Nuclear Power Full Group Purchase Target  
Strategic Science and Technology Program

**About EPRI**

EPRI creates science and technology solutions for the global energy and energy services industry. U.S. electric utilities established the Electric Power Research Institute in 1973 as a nonprofit research consortium for the benefit of utility members, their customers, and society. Now known simply as EPRI, the company provides a wide range of innovative products and services to more than 700 energy-related organizations in 40 countries. EPRI's multidisciplinary team of scientists and engineers draws on a worldwide network of technical and business expertise to help solve today's toughest energy and environmental problems.

EPRI. Powering Progress

© 1998 Electric Power Research Institute (EPRI), Inc. All rights reserved. Electric Power Research Institute and EPRI are registered service marks of the Electric Power Research Institute, Inc. EPRI. POWERING PROGRESS is a service mark of the Electric Power Research Institute, Inc.

 Printed on recycled paper in the United States of America

TR-108536